UNIVERSITY OF SOUTHAMPTON

Faculty of Science

Department of Physics and Astronomy

GALAXY-CLUSTER INTERACTIONS: BENT JETS, WAKES, AND RAM PRESSURE STRIPPING

by Irini Sakelliou

A Thesis submitted for the degree of Doctor of Philosophy

May 1998

UNIVERSITY OF SOUTHAMPTON

ABSTRACT

FACULTY OF SCIENCE

PHYSICS AND ASTRONOMY

Doctor of Philosophy

GALAXY-CLUSTER INTERACTIONS: BENT JETS, WAKES, AND RAM PRESSURE STRIPPING

by Irini Sakelliou

The work in this thesis is concerned with the physical processes that take place in clusters of galaxies, and in particular the manifastations of the galaxy-intracluster medium (ICM) interactions.

The effects of such prosesses are witnessed in wide-angle tailed radio galaxies (WATs), which are radio galaxies whose jets are bent in a wide C-shape. Their appearance is attributed to the combined action of ram pressure and buoyancy forces. A new method is developed, by solving the detailed hydrodynamical equations for a specific point on the radio jets, and applied to two radio galaxies (4C 34.16 and 3C 354) to constrain the galaxy velocity independently from the jet velocity. The jet velocity is also calculated: for both sources it is found to be in the range of $(10^3 - 10^4$ km s$^{-1})$.

An effort is made for the first time to explain observationally the sudden flaring and subsequent deceleration of radio jets from relativistic to subrelativistic velocities. Using *ROSAT* PSPC and HRI data the X-ray emission from the galaxy that host 3C 354 is found to consist of one extended and an unresolved components.

A sample of WAT sources is compiled in order to investigate the dynamics of their host clusters. The direction in which their jets are bent is used to uncover their preferred orbits in the clusters. X-ray observation retrieved from the *ROSAT* archive are used to determine their properties (accurate position of the cluster centre, size and morphology). The results are consistent with the idea that WATs are radio galaxies that originated in poor groups, but are now in the process of falling into richer clusters.

As a cluster galaxy travels through the ICM, gas streams past the galaxy, it is gravitationally deflected and concentrated into a wake, down-stream from the galaxy. This phenomenon is detected in the ICM around the WAT source 4C 34.16. Its properties revealed by X-ray observations (density and temperature) are used to measure the projection of the galaxy velocity onto the plane of the sky.

The extend of the X-ray emission from the early-type galaxies in a fairly rich cluster is found to be smaller for galaxies in poorer environments and is comparable to the size of the galaxies in the optical light, pointing towards a stellar origin for this emission. Additionally the this hypothesis is supported by the comparison of the optical and X-ray lunimosities of these galaxies.

Acknowledgments

I would like to thank my supervisor, Prof. Michael Merrifield, for sharing his enthusiasm for science and guiding during the course of this thesis. His enthusiasm and inspiration kept me interested in this research during the most difficult days. I am also grateful to Dr. Ian M^{c}Hardy, who has always been willing to help me with any problems and questions I had.

I would also like to express my gratitude to Dr. Nikolaos Solomos, who was the first to show me the enjoyment and importance of research in Astrophysics.

Special thanks to my family for their financial support and patience over the years of my studies.

Thanks also go to Pablo and Ignacio for introducing me to the "earthy" taste of the spanish wine, and for teaching me how to call and burn witches in the garden.

I would like to thank Theresa, Natasha and Sparky for helping me get through the last, most stressful months by having deep conversations about food, playing "happy family" and their overwhelming welcoming.

Finally, I would like to thank Chris for making my stay in England very enjoyable, by dragging me out the office and making me climb up high mountains (!). His support, encouragement and honest comments have been crucial during the last years.

Contents

Chapter 1

Introduction

1.1 Clusters of galaxies

1.1.1 Optical properties

Clusters of galaxies, as indicated by their name, are large concentrations of galaxies in a small area in the sky. In three dimensional space, the galaxy density is, on average, 100 times higher in a cluster than in the field, and this overdensity reaches a factor of 10^4 in the central regions of rich clusters. Rich clusters can contain hundreds of galaxies in a region of $\sim$ 3 Mpc. In such a system, the galaxies are bound together by the self gravity of the cluster and move randomly with typical velocities of $\sim$ 750 km s^{-1}. The radial density distribution of galaxies in a cluster can be approximated by a bounded Emden isothermal profile (Zwicky 1957; Bahcall 1977), or by its King approximation (King 1962):

$$n_{\rm gal}(r) = n_{\rm gal}(0)\left[1+\left(\frac{r}{R_c}\right)^2\right]^{-3/2} \qquad (1.1)$$

where $n_{\rm gal}(r)$ is the space number density of galaxies, $n_{\rm gal}(0)$ the central number density, and R_c the cluster's core radius.

The properties of rich clusters of galaxies and of poor cluster or groups, which make up a natural and continuous extension to lower richness, mass, size, and luminosity from the rich clusters, are summarized in Table 1.1.

Table 1.1: PROPERTIES OF CLUSTERS OF GALAXIES

PROPERTY	RICH CLUSTERS	GROUPS AND POOR CLUSTERS
Richness[a]	30–300 galaxies	3–30 galaxies
Radius[b]	$(2\text{–}4)h_{50}^{-1}$ Mpc	$(0.2\text{–}2)h_{50}^{-1}$ Mpc
Radial velocity dispersion	(400–1400) km s^{-1}	(100-500) km s^{-1}
Total mass ($\leq 3H_{50}^{-1}$ Mpc)	$(2 \times 10^{14} - 4 \times 10^{15})h_{50}^{-1}\ M_\odot$	$(6 \times 10^{12} - 2 \times 10^{14})h_{50}^{-1}\ M_\odot$
M/L_B^c	$\sim 150h_{50}\ M_\odot/L_\odot$	$\sim 100h_{50}\ M_\odot/L_\odot$
Cluster number density[d]	$(10^{-6} - 10^{-5})h_{50}^3$ Mpc^{-3}	$(10^{-6} - 10^{-4})h_{50}^3$ Mpc^{-3}
Fraction of galaxies in clusters or groups[e]	$\sim 5\%$	$\sim 55\%$
X-ray temperature	(2–14) keV[f]	≤ 2 keV[g]
Iron abundance	(0.35 ± 0.15) solar	(0.25 ± 0.15) solar
Central gas density	$(0.5\text{–}15)\times 10^{-3}\ h_{50}^{0.5}$ cm^{-3} [f]	$(0.1\text{–}2.0)\times 10^{-3}\ h_{50}^{0.5}$ cm^{-3} [g]
β-index	0.5–0.75[f]	0.4–0.7[g]
Core radius (r_c)	$(100\text{–}750)h_{50}^{-1}$ kpc [f]	$(150\text{–}200)h_{50}^{-1}$ kpc [g]
X-ray luminosity	$(1 \times 10^{43}\text{–}4 \times 10^{45})h_{50}^3$ erg s^{-1}	$\leq 4 \times 10^{43}h_{50}^3$ erg s^{-1}
$M_{\rm gal}/M_{\rm tot}$	$(2\text{–}7)h_{50}^{-1}\%$	$(5\text{–}10)h_{50}^{-1}\%$
$M_{\rm gas}/M_{\rm tot}$	$(10\text{–}30)h_{50}^{-1}\%$	$(3\text{–}25)h_{50}^{-1}\%$

NOTES:
[a] the number of galaxies as defined by Abell (1989), see footnote (1) of chapter 2.
[b] the radius of the main concentration of galaxies, where, typically, the galaxy surface density drops to ~1% of the central core density (Bahcall 1996).
[c] typical mass-to-light ratio (Bahcall 1996).
[d] The number density of clusters decreases sharply with cluster richness (Sarazin 1986).
[e] The fraction of bright galaxies (Bahcall 1996).
[f] from Jones & Forman (1984) and Sarazin (1986).
[g] from Kriss, Cioffi & Canizares (1983), Price et al. (1991), and Doe et al. (1995).

1.1.2 X-ray properties

X-ray emission was first discovered around the galaxy M87 in the Virgo cluster in 1966 (Byram, Chubb & Friedman 1966; Bradt et al. 1967). Since this first discovery, X-ray satellites have revealed emission from all observed clusters of galaxies. The X-ray emission is diffuse, and its extent is comparable to the galaxy distribution.

It is now known that the primary mechanism through which clusters produce X-ray emission is thermal bremsstrahlung (free-free emission) from hot, extended gas (for a review see Sarazin 1986), known as the intracluster medium (ICM). The emissivity of this process depends on the electron density (n_e) and temperature (T) of the emitting gas (Rybicki & Lightman 1979):

$$\epsilon_\nu^{ff} = 6.8 \times 10^{-38} n_e^2 T^{-1/2} e^{-h\nu/kT} g_{ff},\ \text{erg s}^{-1}\ \text{cm}^{-3}\ \text{Hz}^{-1} \qquad (1.2)$$

where it is assumed that the gas is ionized hydrogen, and g_{ff} is a dimensionless parameter which depends on the temperature of the emitting gas and the frequency of the radiation (Gaunt factor). Line radiation from highly ionized species has also been discovered (Mitchell et al. 1976; Serlemitsos et al. 1977). For very hot gas, the strongest line is the iron line at $\sim$ 6.7 keV. At cooler temperatures some other heavy element emission lines such as O, Si, S, and Ne appear (see Sarazin 1986). The detection of these emission lines in the X-ray spectra of clusters of galaxies indicates that the ICM does not consist only of primordial gas, which was not consumed during the formation of galaxies, but has also been enriched with heavy elements. Since heavy elements are produced by nuclear reactions in stars, a fraction of the ICM which now occupies the space between galaxies in clusters must have been expelled from the galaxies during the lifetime of the cluster. Currently, the most plausible candidates for the injection of heavy elements into the ICM are supernovae (see Matteucci & Gibson 1996).

The ICM is held within the cluster by its gravitational potential, and the density of the gas declines with distance from the cluster centre approximately according to the β-model (see Appendix A):

$$n_{\rm gas}(r) = n_{\rm gas}(0)\left[1+\left(\frac{r}{r_c}\right)^2\right]^{-3\beta/2} \tag{1.3}$$

where $n_{\rm gas}(r)$ is the number density of the ICM at a distance r from the cluster centre, $n_{\rm gas}(0)$ the central number density, r_c the core radius of the gas distribution, and β a parameter that defines the slope of the distribution. The observed range of parameters for the ICM are also presented in Table 1.1.

In addition to the distribution of gas in the ICM (see Appendix A), X-ray observations allow us to measure the temperature of the ICM. The temperature is determined by fitting model spectra which incorporate eq. (1.2) and emission from the heavy elements (Raymond-Smith thermal model; Raymond & Smith 1977) to the observed photon spectra.

1.1.3 Evolution and structure of clusters

According to current thinking, structures in the Universe have formed from inhomogeneities in the density distribution of the primeival medium in the early Universe. These density fluctuations have grown by the action of gravity. When the growth of some overdense regions reaches a critical amplitude, they decouple from the cosmic

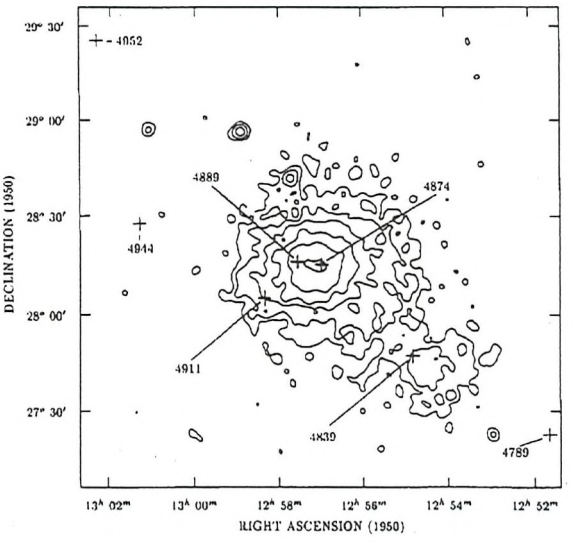

Figure 1.1: Contour map of the Coma cluster in the 0.5 to 2.4 keV energy band from Briel et al. (1992). The positions of some bright galaxies in the cluster are also marked and labeled by their NGC numbers.

Hubble flow, collapse, and dynamically stable objects are formed. Furthermore, in a hierarchical scenario, the formation of structure is expected to proceed from small to large scales (see Peebles 1990; Kaiser 1990), and clusters of galaxies grow by the gravitational accretion of surrounding material.

Although a few years ago it was believed that clusters of galaxies are dynamically relaxed systems, there is increasing evidence that they are still evolving, even the nearby ones, by the accretion of surrounding material. The signature of such processes is generally revealed by optical or X-ray observations. In the Virgo cluster, for instance, only the central part is dynamically old, while the large surrounding region is not virialized and is still infalling towards the cluster centre (Böhringer 1995). Another example of a nearby cluster which has been recently found to be still active is the Coma cluster of galaxies. Coma had long been considered the prototype of well-relaxed, regular clusters. Nevertheless, there is evidence of substructure in the optical and X-ray data (for a review see Biviano 1997); the more pronounced structure is a group of galaxies located to the southwest of the cluster centre around the bright galaxy NGC 4839 (Fig. 1.1). This group was discovered in X-rays by the *ROSAT* satellite (Briel, Henry & Böhringer 1992). All these recent findings demonstrate how clusters of galaxies are formed, and that they are still growing by accretion of material which lies at their peripheries.

1.2 Clusters of galaxies as natural laboratories

Clusters of galaxies, being such large systems with multiple components, offer the opportunity for studying many different and interesting astrophysical problems:

- *Cosmological parameters.* The knowledge of clusters' properties, particularly their masses, mass distributions, and the number densities of clusters as a function of mass, place constraints on the density Ω_0 and on the baryon content Ω_b of the Universe. Currently there are various methods for determining the mass of a cluster: (i) from data of optical observations, using the spatial and redshift distribution of the cluster's galaxies, assuming that the cluster is in virial equilibrium (Kent & Gunn 1982; Kent & Sargent 1983), (ii) from X-ray observations, using the density and temperature profile of the ICM (Böhringer 1994), and (iii) from gravitational lensing, using the lensed images of background objects (Schneider, Ehlers & Falco 1992). Further constraints on the density of the Universe can also be placed by the observed rate at which clusters grow by the accretion of surrounding material (Richstone, Loeb & Turner 1992).

- *Large scale structure.* The present structure and distribution of clusters of galaxies is used to infer the power spectrum of the density fluctuations in the early Universe, and to test the theories of structure formation (West, Oemler & Dekel 1988). Additionally, more clues about the formation and distribution of large scale structure are found in the structure and dynamics of nearby clusters. Since the dynamical time in clusters is comparable to the age of the Universe, there should be signs of recent structure formation in relatively nearby clusters, as discovered in the Coma and Virgo clusters.

- *Nature, quantity, and distribution of dark matter.* In a dynamical study of the Coma cluster, Zwicky (1933) and Smith (1936) first showed that the mass required to hold the galaxies of the cluster together (virial mass) exceeds the luminous mass by a large factor (Table 1.1). This result led them to invoke for the first time the problem of missing mass (dark matter). It is not clear yet how the dark matter is distributed, and what it may consist of, and many studies of cluster morphology and dynamics are devoted to the investigation of this issue.

- *Formation and evolution of galaxies,* for example, the formation of galaxies by cooling flows. The gas density in the core of many clusters is sufficiently high that the radiative cooling time is less than the age of of the cluster. The weight of the overlying gas causes the gas density to rise further, and a cooling

flow is established (Fabian 1994). X-ray observations of this phenomenon show that the mass flow rates are in the range of hundreds of solar masses per year. It has been suggested that the cooled gas forms stars, gradually giving birth to galaxies (Fabian et al. 1982; Sarazin & O'Connell 1983). Another way of approaching the evolution of galaxies is by studying the enrichment of the ICM with heavy elements. The need to explain the observed abundances has prompted the development of detailed theoretical models of galactic evolution in order to establish how and when the enrichment has taken place (De Young 1978; David, Forman & Jones 1991; Ciotti et al. 1991; Mihara & Takahara 1994; White 1991).

- *Environmental effects on galaxies.* It is understood that the cluster environment can affect the structure and dynamics of galaxies. Such alterations can be the result of interaction either between neighbouring galaxies, or a galaxy and the gravitational potential of the cluster, or the cluster's galaxies and the ICM (Fitchett 1990). A piece of evidence that shows such interactions occur comes from the galactic content in rich clusters of galaxies. The fraction of elliptical, S0, and spiral galaxies differs from that in the field, and depends on the cluster classification type[1], or the number density of galaxies in the cluster (Bahcall 1977; Dressler 1980). Elliptical (E) and S0 galaxies are more abundant in rich compact clusters, while the fraction of spirals (Sp) decreases towards the cores of such clusters. A typical rich cluster comprises 35% ellipticals, 45% S0, and only 20% spirals [(E+S0)/Sp=4], while in the field there are 10% ellipticals, 20% S0, and 70% spirals [(E+S0)/Sp=0.5]. Although it is plausible that different initial conditions might have caused the observed morphological segregation (e.g., Sandage, Freeman, and Stokes 1970; Gott & Thuan 1976), this difference could better be explained by Toomre's (1977) suggestion that all galaxies begin as spirals and then merge to form elliptical galaxies. The cluster environment also appears to be able to modify the size of galaxies: cD galaxies can grow to large size (see chapter 2, §2.1), while ellipticals can be depleted of their interstellar media (see chapter 3).

- *Cluster-AGN Association.* Imaging and spectroscopic data (e.g., Ellingson, Green & Yee 1991; Yee & Ellingson 1993) indicate that quasars are found in environments significantly richer than those of average galaxies. This result suggests a correlation between the probability that a galaxy may become active

[1]BM and RS type (see chapter 2 and also Sarazin 1996)

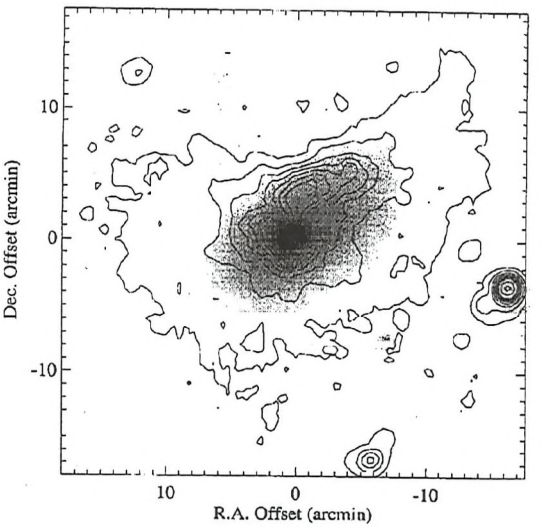

Figure 1.2: Optical image of M86 overlaid by a contour map of *ROSAT* PSPC data (Rangarajan et al. 1995).

and the richness of its environment, and that the nuclear activity is triggered by interactions between galaxies. For example, numerical simulations have shown that interaction between galaxies drive shock waves into the interstellar media of the galaxies which compress the gas towards the centre of the galaxies, possibly initiating or feeding a black hole (Barnes & Hernquist 1991). Additionally, the black hole can be fed by accretion of the surrounding ICM, and from cooling flows (Bremer, Fabian & Crawford 1997).

1.3 Manifestations of the ICM/galaxy interaction

This thesis explores the interactions of the clusters' galaxies with the ICM. In this section, the relevant physical processes and their results are summarized.

1.3.1 Ram pressure stripping

When a galaxy is moving in a cluster its interstellar medium (ISM) feels the dynamical ('ram') pressure resulting from its passage through the ICM. If the gravitational potential of the galaxy is not strong enough to retain the ISM, gas can be stripped from the galaxy (Gunn & Gott 1972; Lea & De Young 1976).

The most extraordinary example of a galaxy which is suffering the result of ram

pressure stripping is the elliptical galaxy M86 in the Virgo cluster (Fig. 1.2). Although this galaxy in the optical light looks like a normal elliptical galaxy, X-ray observations have revealed a plume of X-ray emission associated with it. Since the ISM of elliptical galaxies is in a hot phase that emits X-rays (see for more details in chapter 3), this elongated X-ray feature has been explained as the stripped interstellar medium (e.g., Rangarajan et al. 1995).

1.3.2 Galactic wakes

Consider a galaxy moving through the ICM. The ICM is gravitationally attracted by the moving galaxy, deflected, and concentrated behind it into a wake. This mechanism was first explored by Bondi & Hoyle (1944) in the context of stellar accretion (Bondi-Hoyle accretion). Observationally, the concentration of gas will lead to an enhancement in the diffuse X-ray emission from the ICM in the region immediately behind the moving galaxy, indicating its direction of travel. Numerical simulations (Balsara, Livio & O'Dea 1994) indicate that this physical process can result in a density enhancement by a factor of $\sim$5 behind the moving galaxy. Such features have now been discovered in a number of systems: associated with the galaxy NGC1404 in the Fornax cluster (Jones et al. 1997); in the NGC5044 group of galaxies (David et al. 1994); and also in the poor group which hosts the radio galaxy 4C 34.16 (Sakelliou, Merrifield & M^{c}Hardy 1996; Fig. 5.1).

1.3.3 Distorted radio jets

A few percent of the known galaxies in the Universe contain hyperactive central regions (active galaxies; Blandford 1990). Compared with the size of the galaxy, these regions are extremely compact as indicated by rapid variability of their luminosities flux (Mushotzky, Done & Pounds 1993). The power output of an active galactic nucleus can exceed the luminosity of a thousand normal galaxies, reaching a value as high as 10^{46} erg s^{-1}. The manifestations of the nuclear activity are extremely diverse, leading to the division of active galaxies into several classes, such as quasars, radio galaxies, and Seyfert galaxies. However, in all these cases the 'prime mover' responsible for producing all the energetic phenomena we observe is believed to be a supermassive black hole which resides at the cores of these galaxies.

In radio galaxies the central engine gives rise to the production of two very well collimated jets (Fig. 1.3). They emerge from the opposite sides of the galaxy, which is normally an elliptical, and extend out to several hundred kiloparsecs (see Begelman,

Blandford & Rees 1984; Hughes 1991). Since the first discovery of the 'curious straight ray' associated with M87 by Curtis (1918), it was a long time before it was realized that the double radio sources which straddle the optical galaxy are the radio images of continuous outflows from the active nucleus. In the 1970s, beam models were first postulated to explain these powerful, extended extragalactic radio sources (Rees 1971; Blandford & Rees 1974; Scheuer 1974). Today, jets are envisaged as continuous flows of plasma which transport mass, momentum and energy from the core of a radio source to the outer extended radio structure. This notion is supported by the direct detection of motion of features in jets by radio observations (e.g. Biretta 1992). The radio emission is synchrotron radiation, produced by electrons spiralling in a magnetic field.

Fanaroff & Riley (1974) pointed out an important morphological difference which divides radio galaxies into two distinctive classes: 'edge-brightened' or FRII radio galaxies (Fig. 1.3), which are brighter at the outer edges of the radio lobes, and 'edge darkened' or FRI radio sources (Fig. 1.3), where the brightest part of the jets are closer to the host galaxy, and then fade away with distance from the radio core. Additionally, Fanaroff & Riley (1974) discovered that this morphological division is also a division in the total radio luminosity: FRIs are low luminosity sources with $P_{20\ \mathrm{cm}} \leq 10^{24-25}$ W Hz^{-1}, while FRIIs have radio luminosities above this limit.

Apart from the above mentioned general classification, a wide variety of morphological types of radio galaxies have been identified. Figure 1.4 shows an example of the radio galaxies known as wide-angle tailed radio sources (WATs). This class of objects was first classified by Owen & Rudnick (1976). They are C-shaped structures associated with bright galaxies in clusters. More extremely bent jets are found in the so called narrow-angle tailed radio sources (NATs; or head-tail radio galaxies). As shown in Fig 1.5, the jets in these radio galaxies are bent in a very narrow angle. NATs, like WATs, reside in poor or rich clusters of galaxies. X-ray observations have confirmed the presence of gas around them (e.g., Burns & Balonek 1982), and it is believed that the observed morphology of these radio galaxies is an environmental effect mainly resulting from the interactions of the radio jets with the hot ICM.

1.4 Applications of the ICM/galaxy interactions

As explained in the previous sections, the interactions between a cluster's galaxies and the ICM result in stripped galaxies, condensations of gas around the galaxies, and distorted radio jets. As soon as the details of these physical processes are understood

and quantified, they can be used as tools for investigations concerning for example, the dynamics of clusters and the nature of radio jets. A few examples of such applications are as follows:

- *Ram pressure stripping.* The size of the ISM was used by Burns et al. (1986) to constrain the velocity of a galaxy relative to the ICM since the greater ram pressure is, the smaller the size of the ISM is expected to be. Similarly, the size of the ISM of spiral galaxies in the Virgo cluster, combined with line-of-sight velocities and the density distribution of the ICM, was used by Böhringer et al. (1997) to accurately locate these galaxies with respect to the central galaxy in the cluster, M87.

- *Galactic wakes.* X-ray wakes are expected to occur behind any moving galaxy in clusters. Information of wake direction combined with line-of-sight velocities can be used to reveal the orbits of galaxies, and constrain the shape of the cluster's gravitational potential (Merrifield 1998).

- *Radio jets.* The velocity of jet propagation and the minimum energy of the magnetic field has been used to estimate the density of the gas around radio galaxies (Wellman, Daly & Lin Wan 1997). This application is of great importance, since the resolution of current X-ray instruments generally makes it very difficult to determine the extent and properties of the X-ray emission (e.g., Crawford & Fabian 1993; 1995; Worrall et al. 1994) from clusters at high redshifts ($z \geq 0.5$).

1.5 Content of the Thesis

This thesis presents an extensive investigation of the interactions between cluster galaxies and the ICM. In Chapter 2, the direction in which the jets in WATs are bent is used to decipher their orbits in rich clusters, and ascertain the dynamical history of these clusters. Chapter 3 investigates the gas content of the early-type galaxies in a relatively rich cluster of galaxies, and the effectiveness of stripping mechanisms. In Chapter 4, a detailed hydrodynamical model for the bending of jets is used in combination with X-ray observations to constrain the galaxy and jet velocity of the bent jets of a radio galaxy. Finally, in Chapter 5 the discovery of a wake of X-ray emission behind a moving galaxy is reported. Its properties, derived from the X-ray observations, are used to find the velocity of the galaxy on the plane of the sky.

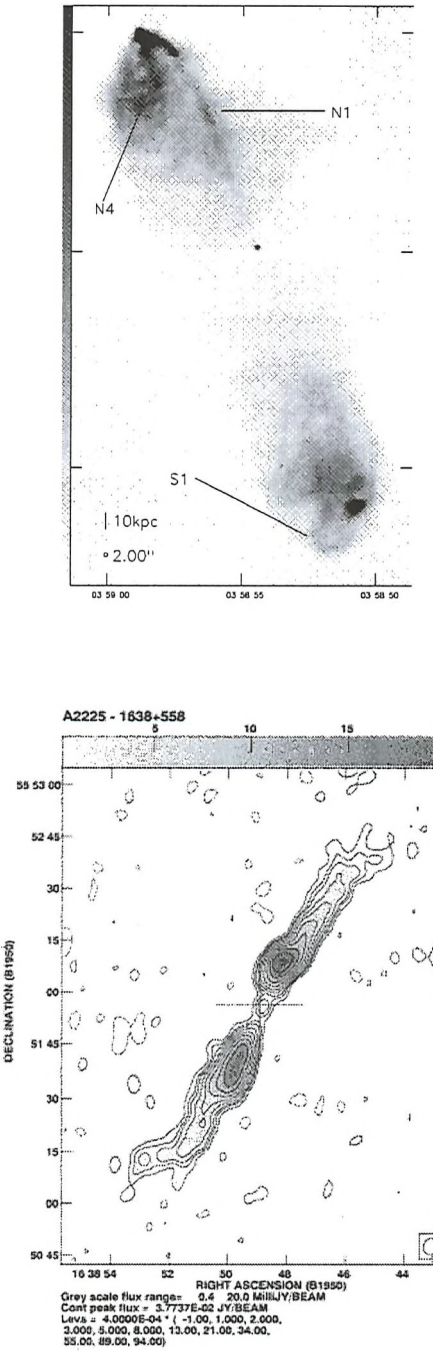

Figure 1.3: Top panel: the FRII radio galaxy 3C 98 (from Leahy et al. 1997). Bottom panel: the FRI radio galaxy 1638+558 in the Abell 2225 cluster of galaxies (from Owen & Ledlow 1997). The cross marks the position of the optical galaxy.

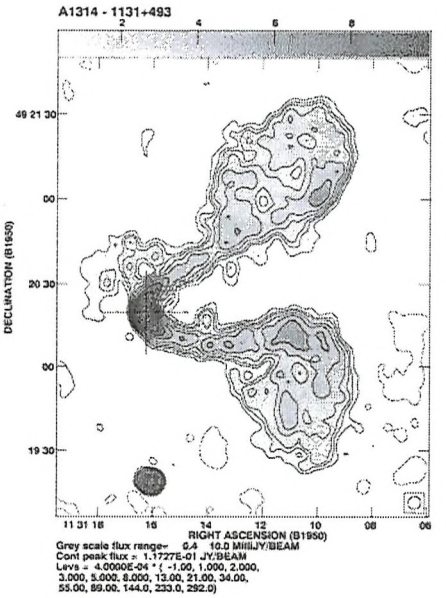

Figure 1.4: The wide-angle tailed radio galaxy 1131+493 in the cluster of galaxies Abell 1314 (from Owen & Ledlow 1997). The cross marks the position of the optical galaxy.

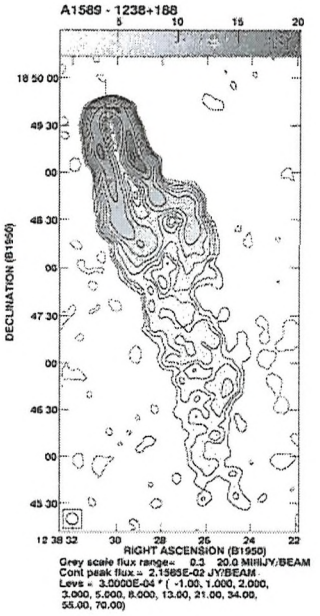

Figure 1.5: The narrow-angle tailed radio galaxy 1238+188 in the cluster of galaxies Abell 1589 (from Owen & Ledlow 1997). The cross marks the position of the optical galaxy.

Chapter 2

WATs in Abell clusters

2.1 Introduction

Wide-angle tail radio galaxies (WATs) form a class of radio galaxies whose special appearance is attributed to the interaction of the radio emitting jets with the surrounding medium. These radio sources appear to be symmetrically bent in a wide 'C' shape. Their structure, as seen in radio maps, gives the immediate impression that the jets are being 'swept back' by the dynamic pressure resulting from the motion of the associated galaxy through the inter-galactic medium. This 'ram pressure' model was first developed by Begelman, Rees & Blandford (1979), and studied in more detail by Vallée, Bridle & Wilson (1981) and Baan & McKee (1985).

Unfortunately, there is a piece of evidence that seems to contradict this model. WATs are usually associated with the brightest cluster ellipticals (D or cD galaxies). These galaxies are supergiant, superluminous elliptical galaxies, and are thought to lie at rest at the centres of clusters of galaxies. For example, cD galaxies are defined as galaxies with a nucleus of a very luminous elliptical galaxy embedded in an extended (sometimes >1 Mpc) halo of low surface brightness (Matthews et al. 1964). In addition to the morphological differences, 'first-ranked' cluster galaxies are believed not to follow the same formation scenario as normal ellipticals. Theories of such galaxies' formation and evolution suggest that they were formed and have been modified by dynamical processes which take place in clusters of galaxies. This belief is further supported by the relative lack of such galaxies in the field, isolated from any other galaxy. Gallagher & Ostriker (1972) explained these giant galaxies as the result of the gradual piling up of debris produced by tidal interactions between the normal cluster galaxies. Close encounters of galaxies lead to the stripping of stars and interstellar medium from the galaxies. The galactic material is then left behind as the galaxies

continue their journey in the cluster, and is concentrated towards the cluster centre. Another scenario presents these big cluster galaxies as cannibals, which grow by the accumulation of other cluster galaxies ('galactic cannibalism', Ostriker & Tremain 1975; Ostriker & Hausman 1977). Recent numerical studies of cluster evolution have illustrated how the above-mentioned mechanisms take place in clusters, and have successfully reproduced the formation of a big galaxy at the cluster centre in a relatively short time (Bode et al. 1994; Garijo, Athanassoula & García-Gómez 1997). Whatever the details and the exact time of the formation of these galaxies, all theories agree that they must lie at the centres of the clusters, and that they cannot move away to large distances. The expectation that cD galaxies are located at the minimum of the cluster gravitational well is also supported observationally: the line-of-sight velocities of cD galaxies agree with the mean velocities of the other cluster galaxies (Quintana & Lawrie 1982), which confirms that they are at the kinematical centres of the clusters, at rest relative to other galaxies; X-ray observations also find that they coincide with the peak of the ICM distribution (Jones & Forman 1984), again implying that they lie stationary at the centres of clusters.

Therefore, if such galaxies are indeed the hosts of WATs they cannot move at the speeds required by the ram pressure model, so that the radio jets are bent at the observed angle. In order to avoid this problem, other forces, which do not require a moving galaxy, have been implicated to explain the shape of the jets in WATs:

- *Gravitational forces,* for example buoyancy. If the jets are less dense than their surroundings, buoyancy forces drag them towards regions in the ICM where the densities inside and around the jets are equal. Such a model requires that the galaxy is not at the bottom of a spherically symmetric gravitational potential, and that there is a steep gradient in the density distribution of the ICM, so that this force becomes effective.

- *Electromagnetic forces.* Another candidate for the bending mechanism for WATs is an electromagnetic force arising from the interaction between a jet that carries a net electrical current and the magnetic field in the ICM (Eilek et al. 1984). Given our poor understanding of currents in jets and magnetic fields in clusters, this model has not been extensively explored. One major problem with it, is that it requires a highly and favorably ordered magnetic field in order to produce the symmetric shape of WATs.

- *Jet-cloud collisions.* Jets could be deflected by collisions with dense clouds in the ICM. Although this model can be at work in some radio galaxies whose

jets are deflected and disrupt abruptly, again it has difficulty reproducing the large-scale symmetric structure of the WATs (Burns et al. 1986).

In an attempt to rescue the ram pressure model, it has been recently suggested that WATs reside in environments which are suffering the consequences of recent merger events (Pinkney, Burns & Hill 1994; Gómez et al. 1997a, b; Loken et al. 1995). In such a case the necessary ram pressure to bend the jets may be provided naturally by the violent collision of the two clusters.

The idea that a WAT indicates the place where a recent merger event has occurred has gained a lot of attention recently, after the realization that clusters of galaxies are dynamically young and merge frequently. Theoretical and observational studies have forced us to discard the idealized picture of a spherical relaxed cluster which is isolated and does not interact with its surroundings (e.g., Evrard 1990; Jing et al. 1995; Frenk et al. 1996). In a hierarchical universe, large-scale structure forms through the accretion of small structures continuously, even at the present day, and therefore clusters are far from being relaxed systems. X-ray observations of the hot ICM reveal significant 'substructure' in clusters, a departure from the spherically symmetric image. This substructure is identified by: a) multiple X-ray peaks, instead of the expected one peak that defines the minimum of a cluster's gravitational potential; b) clumpiness, instead of a smooth distribution of the ICM; c) departures from spherical isophotes, with many clusters being elongated, d) isophotal twisting, where the position angle of the major axis of the elliptical isophotes changes; e) centroid shifting, where the centre of the isophotes is not always the same; and f) temperature substructure, instead of an isothermal gas distribution.

Clusters displaying strong X-ray evidence for a recent (or ongoing) merger include Abell 2256 (Briel et al. 1991), Abell 754 (Henriksen & Markevitch 1996; Henry & Briel 1995; Zabludoff & Zaritzky 1995), the Coma cluster (White, Briel & Henry 1993), and Abell 2255 (Burns et al. 1995; Feretti et al. 1997; Davis & White 1998). X-ray temperature maps, which show that clusters are not isothermal, have recently become available (Abell 2256 Roettiger, Burns, Pinkney 1995; A2255 Davis & White 1998; A754 Henry & Briel 1995; Perseus Arnaud et al. 1994; A2163 Markevitch et al 1994).

Evidence that clusters merge frequently also comes from the luminosity function of clusters of galaxies. Several studies have found that there is a lack of X-ray bright clusters in the past compared to their space density at the present time (Henry et al. 1992; Gioia et al. 1990; Edge et al. 1990).

Although more difficult to identify, substructure is also present in the clusters'

galaxy distribution. If a cluster is relaxed, the velocity dispersion profile can be approximated by a Gaussian function. Departures from this symmetric shape and the appearance of multiple peaks provide indications of the presence of clumps of galaxies in the clusters which are characterized by a velocity dispersion different from the rest of the cluster. Dressler & Schectman (1988) found this signature of substructure in 30-40% of the rich clusters of galaxies they studied, while Bird (1993) estimated that 30-70% of clusters contain significant substructure in their galaxy distribution. Even clusters that host a cD galaxy at their centres, and were thought to be the more evolved and relaxed, have been recently found to depart from the idealized picture of a relaxed system (Way, Quintana & Infante 1998).

Numerical simulations (Evrard 1990; Roettiger, Burns, Loken 1993; Roettiger, Burns & Loken 1996; Roettiger, Loken & Burns 1997; Schindler & Müller 1993) of two colliding clusters put the finishing touches to the picture of such a merger event. They show that large gas motions persist in the clusters for a long time after the merger event. If a radio galaxy happens to be near the centre of either the cluster or the subcluster, after the first impact its jets will be bent symmetrically, since the collision of two clusters will provide the necessary ram pressure.

So, are WATs at rest at the centres of the clusters? If this is found to be the case, more attention must be given to forces other than ram pressure in order to explain the shape of the bent jets in these sources. On the other hand, if they are not at the minima of their clusters' potentials, it will be an indication that they are in motion relative to the cluster centre. The sort of orbits they follow will then provide clues to the history of these systems, and will shed light on the details of their dynamics.

In order to answer all these questions, a sample of WATs in clusters of galaxies has been compiled from the available radio surveys. Section 2.2 describes the process by which radio galaxies were selected to represent the WAT class, and in sections 2.3 and 2.4 the X-ray observations of the field around them, and their analysis, are presented. Section 2.5 investigates the distribution of WATs in clusters, while in section 2.6 their orbits are quantified.

2.2 Sample selection

Over the last ten years, Abell clusters of galaxies have been extensively mapped at the radio frequency of 1.4 GHz by Zhao, Burns & Owen (1989), Owen, White & Burns (1992), and Owen, White & Ge (1993). Maps of the radio sources found in these clusters, along with the optical identifications of the galaxies that host them,

are given by the previous works and by Ledlow & Owen (1995a) and Owen & Ledlow (1997). This sample of radio galaxies in Abell clusters is statistically complete for sources with a redshift of $z < 0.09$ and flux density at 1.4 GHz of $S_{1400} > 10$ mJy. Additionally, the whole sample has been extended to include clusters out to a redshift of $z = 0.25$. This radio survey forms the basis of the present investigation.

As the primary criterion, WATs have been selected on the basis of their morphology. Extended sources which show clearly the characteristic 'C' shape of WAT sources have been collected to define a sample of WATs in Abell clusters. Some radio galaxies which were previously classified as WATs by various investigators but whose jets do not appear to be significantly bent are not included in the present sample. An example of such a source is the radio galaxy 0043+201 in Abell 98. Although for the study of its dynamics it was treated as a bent WAT source (Krempec-Krygier & Krygier 1995), radio maps do not show the characteristic bent structure (O'Donoghue et al. 1990). Based on indirect arguments, Giovannini et al. (1987) suggested that its jets could be bent along the line of sight. Given its appearance in the radio maps, this radio galaxy has not been used in the present survey.

Subsequently, sources whose jets were found to be smaller than $100h_{50}^{-1}$ kpc were excluded. This selection criterion is imposed in order to discard sources that lie entirely inside the interstellar medium of the host galaxy. The reason for such a preference towards large WATs is that the present study is based on simple models that describe the interaction of the jets with the ICM, without involving the dynamical effects of the galactic ISM. Therefore, since it is expected that the ISM plays a major roll in the dynamics of small WATs, inclusion of them in the present sample would not be appropriate, and would dilute the results of the survey. The WAT sources PKS 2322-123 in Abell 2597, 2207-124 in Abell 2420, 1519+488B in Abell 2064, 1508+059 in Abell 2029, NGC 4874 in Coma, 1142+157 in Abell 1371, and 0720+670 in Abell 578 were all found to be too small to be used for the purpose of this investigation.

The final sample of WATs in Abell clusters is presented in Table 2.1. The first two columns give the names of the radio galaxy, while the third one gives the Abell cluster in which it is located. Additionally, this table gives details of the available X-ray observations of the field around the WAT (see §2.3). Information about the Abell clusters is collected in Table 2.2: its redshift [column (2)]; the length in kiloparsecs to which one arcsec corresponds at the distance of the cluster [column(3)]; the number

Table 2.1: X-RAY OBSERVATIONS OF WATs

(1)	(2)	(3)	(4)	(5)	(6)	(7)
			ROSAT OBS.		*Einstein* OBS.	
Source name	Other name	Abell cluster	Sequence number	Exposure (sec)	Detector	Exposure (sec)
0035+180		A69	–		–	
0110+152		A160	rh800953	16501	IPC	2700
0123-016B	3C 40	A194	rp800316n00	24482	–	
0141+061		A245	–		–	
0146+138		A257	–		–	
0255+058A,B	3C 75	A400	rp800226	23615	IPC	13000
0327+246B		A439	–		IPC	2082
0647+693	4C 69.08	A562	rp800500	5865	–	
0658+330		A567	–		–	
0705+486		A569	wp800575	4181	IPC	800
0803-008	3C 193	A623	rp800506	4447	–	
0836+290		A690	–		IPC	6061
0838+32	4C 32.26	A695	–		–	
0908-103		A761	–		–	
0909+162		A763	–		–	
1011+500		A950	–		–	
1025+040		A1024	–		–	
1108+410A		A1190	–		–	
1131+493	IC 708	A1314	wp800392	2940	IPC	6600
1159+583	4C 58.23	A1446	rp800501	7094	IPC	11400
1200+519		A1452	–		–	
1221+615		A1529	–		–	
1225+636		A1544	–		–	
1227+119		A1552	wp800577	3398	–	
1231+674	4C 67.21	A1559	–		–	
1233+168	4C 16.33	A1569	rp800504	3687	IPC	3000
1243+26(7)		A1609	–		IPC	1600
1300+32(1)		A1667	–		–	
1306+107A	4C 10.35	A1684	–		–	
1320+584		A1731	–		–	
1333+412	4C 41.26	A1763	rp800252	15659	IPC	4500
1415+084		A1890	rh800649	13836	IPC	3200
1433+553		A1940	rp800502	3433	IPC	9100
1445+149		A1971	–		–	
1636+379		A2214	rp800503	5209	–	
1638+538	4C 53.37	A2220	rp201446	24402	IPC	8500
1820+689		A2304	rp800498	5412	HRI	7900
1826+747		A2306	rp800505	4470	IPC	20300
2236-176		A2462	rp800495	4289	–	
2330+091		A2617	–		–	
2335+267	3C 465	A2634	rp800014	10534	IPC	22500
2336+212		A2637	rp000111	2580	–	

Table 2.2: Cluster properties

(1) Abell cluster	(2) z	(3) 1 arcsec (h_{50}^{-1} kpc)	(4) Number of galaxies	(5) R	(6) BM	(7) RS
A69	0.1448	4.21	106	2	II-III:	Ic
A160	0.0444	1.29	34	0	III	C
A194	0.0180	0.52	37	0	II	La
A245	0.0788	2.29	40	0	–	Ic
A257	0.0706	2.05	51	2	II-III	C
A400	0.0238	0.69	58	1	II-III	Ic
A439	0.1063	3.09	35	0	–	La
A562	0.1100	3.20	70	1	II-III	La
A567	0.1270	3.69	60	1	–	Ic
A569	0.0195	0.57	36	0	II:	B
A623	0.0871	2.53	57	1	–	cD
A690	0.0788	2.29	52	1	I	cD
A695	0.0694	2.02	63	1	III	F
A761	0.0921	2.68	50	1	–	C
A763	0.0851	2.48	50	1	II-III	cDp
A950	0.2081	6.05	55	1	II-III	Ic
A1024	0.0733	2.13	69	1	II:	B:
A1190	0.0794	2.31	87	2	II:	B
A1314	0.0338	0.98	44	0	III	C
A1446	0.1035	3.01	85	2	II-III	F
A1452	0.0630	1.83	46	0	–	C
A1529	0.2324	6.76	43	0	–	C
A1544	0.1459	4.24	62	1	II:	F
A1552	0.0843	2.45	75	1	II	B
A1559	0.1071	3.12	50	1	II	Bb
A1569	0.0784	2.28	40	0	–	C
A1609	0.0891	2.59	56	1	II-III:	C
A1667	0.1648	4.79	98	2	III:	F:
A1684	0.0864	2.51	68	1	III:	C
A1731	0.1932	5.62	92	2	II	Bb
A1763	0.2278	6.63	152	3	III	La
A1890	0.0570	1.66	37	0	I-II:	cD
A1940	0.1396	4.06	130	3	III	C:
A1971	0.2084	6.06	42	0	–	F
A2214	0.1610	4.68	38	0	–	Ic
A2220	0.1106	3.22	42	0	–	I:c
A2304	0.0880	2.56	34	0	II	La
A2306	0.1271	3.70	47	0	III:	B
A2462	0.0698	2.03	40	0	I-II:	B
A2617	0.1623	4.72	95	2	II:	L
A2634	0.0321	0.93	52	1	II:	cD
A2637	0.0707	2.05	60	1	II	La

Table 2.3: Radio properties

(1)	(2)	(3)	(4)	(5)	(6)
	OPT. POSITION				
CLUSTER	α (1950)	δ (1950)	l (h_{50}^{-1} kpc)	$F_{1.4}^{total}$ (mJy)	$L_{1.4}^{total}$ ($\times 10^{25}$ W Hz^{-1})
A69	00 35 17.19	+18 04 23.9	230	209	0.96
A160	01 10 20.45	+15 13 35.2	300	719	0.28
A194	01 23 27.55	−01 36 18.9	140	3270	0.21
A245	01 41 19.20	+06 09 34.0	340	124	0.16
A257	01 46 30.66	+13 48 08.2	120	132	0.13
A400(a)	02 55 02.99	+05 49 37.0	130	2795	0.31
A400(b)	02 55 03.08	+05 49 20.9	130	2795	
A439	03 27 32.25	+24 37 36.0	140	320	0.78
A562	06 47 54.58	+69 23 31.5	250	800	2.06
A567	06 58 52.48	+33 01 47.2	270	339	1.18
A569	07 05 21.39	+48 41 47.2	140	940	0.07
A623	08 03 05.14	−00 49 43.1	160	1298	2.05
A690	08 36 13.50	+29 01 12.9	530	1022	1.31
A695	08 38 06.74	+32 35 42.2	200	608	0.60
A761	09 08 32.61	−10 21 33.7	400	177	0.31
A763	09 09 48.50	+16 12 23.0	144	183	0.27
A950	10 11 26.68	+50 00 27.6	405	394	3.98
A1024	10 25 47.94	+04 00 52.1	115	272	0.30
A1190	11 08 54.20	+41 03 25.7	132	116	0.15
A1314	11 31 16.25	+49 20 19.8	100	835	0.19
A1446	11 59 30.41	+58 18 51.3	150	765	1.76
A1452	12 00 34.13	+51 57 12.4	130	720	0.58
A1529	12 21 07.38	+61 31 29.6	324	321	4.14
A1544	12 25 33.20	+63 39 37.8	156	210	0.98
A1552	12 27 20.34	+11 57 13.1	170	1655	2.44
A1559	12 31 03.88	+67 24 17.2	170	879	2.14
A1569	12 33 55.19	+16 48 47.6	130	1338	1.70
A1609	12 43 54.69	+26 43 39.3	410	357	0.59
A1667	13 00 54.54	+32 06 08.1	420	325	1.98
A1684	13 06 34.40	+10 45 32.8	210	405	0.63
A1731	13 20 58.62	+58 25 41.3	191	325	2.79
A1763	13 33 09.52	+41 15 24.1	200	797	9.80
A1890	14 15 02.92	+08 26 19.8	170	331	0.21
A1940	14 33 54.92	+55 20 53.2	140	447	1.91
A1971	14 45 40.62	+14 59 19.5	436	419	4.25
A2214	16 36 15.71	+37 58 53.7	280	617	3.58
A2220	16 38 24.50	+53 52 30.8	390	626	1.63
A2304	18 20 01.32	+68 55 24.0	150	801	1.29
A2306	18 26 23.40	+74 42 05.8	140	244	0.85
A2462	22 36 30.07	−17 36 04.8	200	1642	1.64
A2617	23 30 58.81	+09 08 58.7	260	218	1.29
A2634	23 35 58.93	+26 45 16.2	220	7650	1.59
A2637	23 36 11.04	+21 13 26.3	260	145	0.15

of galaxies [1] in the cluster [column (4)]; the richness [2] class of the cluster [column (5)]; the Bautz-Morgan (BM)[3] type of the cluster [column (6)]; and the Rood-Sastry (RS)[4] type of the cluster [column (7)]. The radio properties of the WATs are presented in Table 2.3: the position of the radio core [columns (2) and (3)]; an approximate length of the radio jets [column (4)]; the flux at 1.4 GHz taken from Owen et al. (1992) and Owen et al. (1993); the radio luminosity at 1.4 GHz calculated for a cosmology with $H_0 = 75$ km s^{-1} Mpc^{-1} and $q_0 = 0.5$ [column (6)].

The selection of a radio source and the classification of it as a WAT in the way described above is dependent on the quality and resolution of the available radio data. If the resolution of the radio observation is not high enough to reveal the detailed structure of the WAT, it might be mistaken for a different class of radio galaxy (such as a narrow-angle tailed radio galaxy) and not included in the sample. For this reason, the literature has been examined to see if higher quality radio maps exist for any of the WAT candidates. Only a few sources were found to have been observed at higher resolution, most of which are presented by O'Donoghue et al (1990). However, since we have restricted the sample to contain sources that are larger than $100h_{50}^{-1}$ kpc and that lie at a redshift of $z < 0.25$, there should be very few WATs that have not been observed with the requisite angular resolution, because at a redshift of 0.25, a WAT that meets our criteria will have an extent of ~ 30 arcseconds, significantly greater than the spatial resolution of almost all the radio data.

Confirmation that Table 2.1 contains a representative sample of WATs comes from

[1]The number of galaxies that belong to the cluster which are more luminous than $m_3 + 2$ mag, where m_3 is the apparent magnitude of the third most luminous cluster member and are contained within an Abell radius. The Abell radius of a cluster is defined as $R_A = 1.7/z$ arcmin, where z is the redshift of the cluster. The number of galaxies is corrected for background contaminations, and is taken from Abell et al. (1989).

[2]The richness of the cluster based on the number of galaxies presented in column (4) of Table 2.2. It was defined by Abell (1965, 1975) as: R=0 30-49 galaxies, R=1 50-79 galaxies, R=2 80-129 galaxies, R=3 130-199 galaxies, R=4 200-299 galaxies, and R=5 > 300 galaxies.

[3]Bautz & Morgan (1970) give a classification system based on the degree to which the cluster is dominated by its brightest galaxy. BM type I clusters are dominated by a single central cD galaxy. In type II clusters, the brightest galaxies are intermediate between cD and normal giant elliptical galaxies, while in type III clusters there are no dominating cluster galaxies. Types I-II and II-III are intermediate. ':' indicates a questionable classification. The information presented in this column is taken from Abell et al. (1989).

[4]This classification system is based on the nature and distribution of the ten brightest cluster galaxies. The six RS types are defined as follow: *cD* the cluster is dominated by a central cD galaxy; *B, binary* the cluster is dominated by a pair of luminous galaxies; *L, line* at least three of the brightest galaxies appear to be in a straight line; *C, core* four or more of the ten brightest form a cluster core with comparable cluster separation; *F, flat* the brightest galaxies form a flattened distribution on the sky; *I, irregular* the distribution of the bright galaxies is irregular. The RS types of the WAT clusters are taken from Struble & Rood (1987).

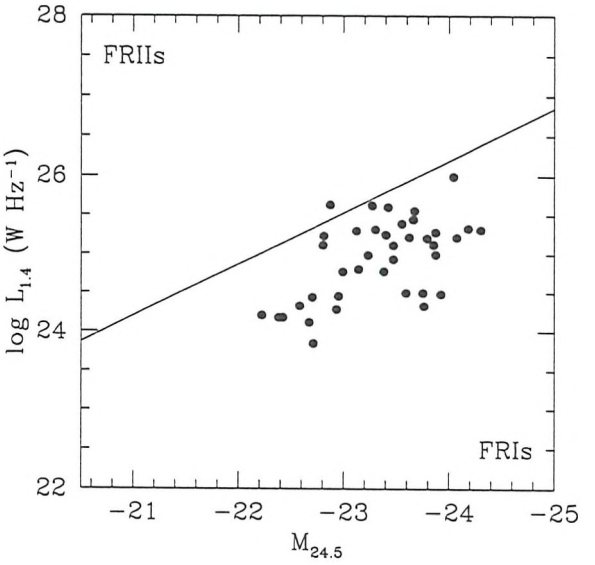

Figure 2.1: The radio luminosity-optical magnitude diagram for only the WAT sources. The solid line divides the plane into two regions: the upper region is occupied by FRII sources, while the lower one by FRI radio galaxies. This plot is directly comparable to the one presented by Ledlow & Owen (1996).

comparing the optical magnitude of the galaxies that host them with their total radio power. Figure 2.1 shows the radio luminosity at 1.4 GHz, given in column (6) of Table 2.3, versus the absolute magnitude of the galaxies that host the WATs. The absolute magnitudes were taken from Ledlow & Owen (1995b), and Owen & White (1991). The plot is the same scale as and therefore directly comparable to the one presented by Ledlow & Owen (1996), which was constructed using all the radio galaxies in their sample and others collected from the literature. The solid line represents the division between FRI and FRII (Fanaroff & Riley 1974) radio galaxies. WATs have been classified as FRI radio galaxies, and as seen from this plot all selected sources lie below the division line, apart from the source in Abell 1763, which is just above it. Additionally, they are associated with bright galaxies (O'Donoghue, Eilek & Owen 1993), whose optical magnitudes lie between -22 and -24.5 mag.

This analysis confirms that all the objects selected show similar characteristics and they can be assigned to the same subgroup of radio galaxies known as WATs.

2.3 X-ray observations

The *ROSAT* database has been searched, in order to find which of the clusters containing WAT sources have been observed in the X-ray energy band. The search was constrained to a circle of 30 arcmin radius around the radio source. The *ROSAT* observations found and used for any following analysis are presented in Table 2.1 [column (4)]. The sequence numbers designate the detector used for each particular observation ('wp' or 'rp' for PSPC, and 'wh' or 'rh' for HRI). All these datasets, apart from the HRI observation of Abell 160, are public. Some of the clusters with PSPC observations have also been observed by the HRI detector, but these datasets are not reported, or used here (e.g., Abell 194, Abell 400, Abell 2634). The total exposure times of the reported observations are also given in column (5) of Table 2.1. Notes on the individual sources with X-ray observations are given in Appendix D.

The clusters were also observed in the *ROSAT* All Sky Survey (RASS) performed with the PSPC. However, as will become clear from the discussion below, the short exposures in the survey observations mean that these data are not suitable for the present investigation. X-ray images of the field around some radio galaxies are presented in Fig. 2.4 and Fig. 2.5. For the remainding WAT sources, X-ray plots are given by Gómez et al. (1997b).

It is clear from Table 2.1 that less than half of the clusters in this sample of Abell clusters that contain WATs have been observed with the *ROSAT* satellite. In order to increase the coverage of X-ray observations over the sample, the *Einstein* database was also searched. Only three of the clusters that have not been observed by *ROSAT*, have *Einstein* observations (A439, A690, A1609). Unfortunately, in all these cases the exposure times are too short to reveal any sign of the emission from the ICM of the associated cluster. Therefore, only the *ROSAT* observations are used in the following sections.

The sparsity of X-ray observations reduces the sample of WATs in Abell clusters. It also raises the possibility that the clusters for which X-ray data exist may form a biased subsample of the WAT systems. In order to check if the clusters with available X-ray observations constitute a representative subsample of the initial sample, the distribution of WATs over the range of redshifts from 0.00 to 0.25 for both samples is compared in Fig. 2.2. Figure 2.2 (a) presents the distribution of all the sources selected in §2.2 over the redshift range from $z = 0$ to 0.25, while Fig. 2.2 (b) shows the redshift distribution of only the sources which have X-ray observations. A first comparison of these two distributions shows that the sample of WATs that have been observed in X-rays contains representatives from the whole range of redshifts. In order

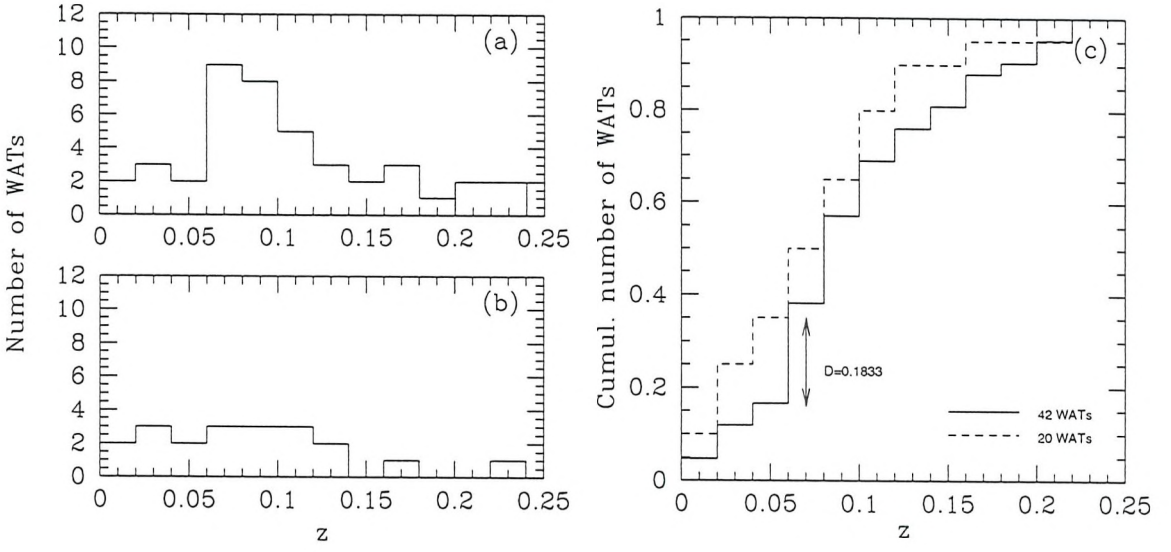

Figure 2.2: The distribution of WATs over the range of redshift from 0.00 to 0.25; (a) for the total sample of 43 galaxies selected in §2.2, and (b) for only the 22 that have X-ray observations. The cumulative distribution of both previous samples is shown in (c), where D is the maximum difference between the two distributions, and is used to calculate the KS probability (see text).

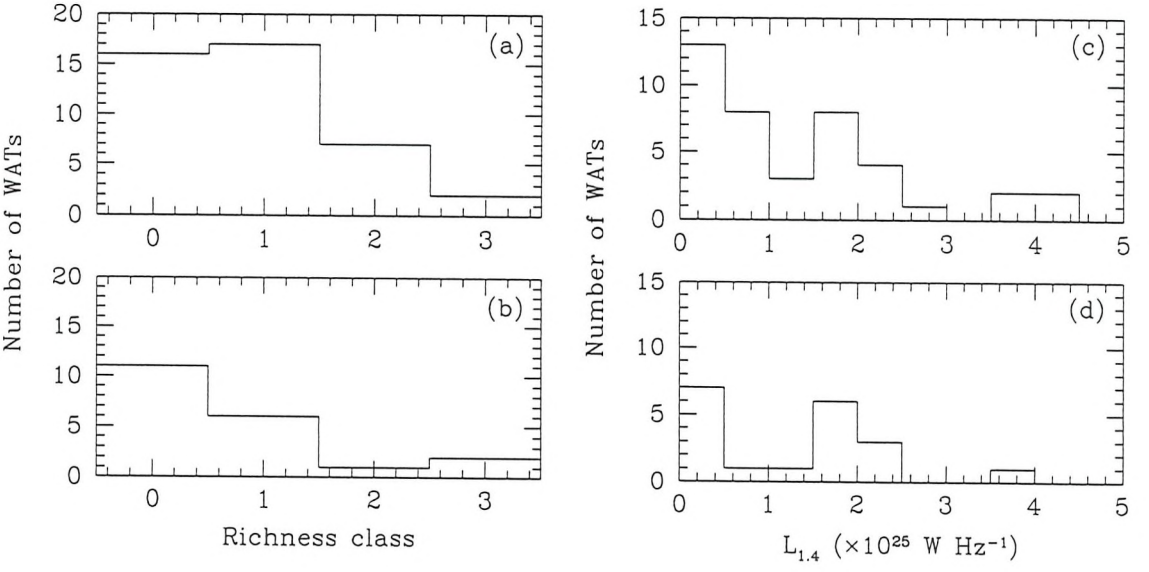

Figure 2.3: The distribution of richness class for WATs: (a) for the whole sample, (b) for WATs where X-ray data exist; the distribution of radio power (c) for the whole sample and (d) for the subsample for which X-ray data exist.

to quantify the difference between these two distributions, a Kolmogorov-Smirnov test (KS; Press et al. 1989) has been applied. The KS statistical test compares the cumulative distributions of two samples, addressing the question of whether they can be drawn from the same distribution. Figure 2.2 (c) shows the cumulative distribution for the two samples of WATs shown in Fig. 2.2 (a) and (b). Such a plot gives for a given redshift the number of WATs that have a redshift less than the given value. The KS test compares the maximum value of the difference between these two distributions [D in Fig. 2.2 (c)], by providing its significance level. For the redshift distribution the KS test gives that D is significant at the 87.4% level, and thus there is no evidence that these two distributions are different. A similar procedure has been followed to compare the clusters' richness distribution [Fig. 2.3 (a) and (b)] and radio powers [Fig. 2.3 (c) and (d)]. Again, the KS test reveals no evidence that the subsample is in any way biased (KS probabilities 79.6% and 99.5% respectively).

2.4 Data analysis

2.4.1 X-ray centres

One important question that we must address if we are to understand the nature of WAT sources is where their host galaxies are located relative to the cluster centres. Are they really at the minimum of the gravitational potential of the clusters, as expected? The investigation of this question requires an accurate and objective determination of the cluster centre. Optical observations, which provide the position and number of galaxies in a cluster, have difficulty in giving an accurate position. The number of galaxies in a cluster is small, and it is possible that the sample of galaxies is contaminated by foreground and background galaxies. Such a difficulty in some cases has led to the use of the position of the biggest and brightest galaxy in the cluster as the cluster centre (e.g. Kent & Gunn 1982). Thus, optical observations could have incorrectly placed the bright galaxies that host the WATs at the cluster centre.

The hot ICM, on the other hand, being a continuous medium, settles down in the cluster, outlining the gravitational potential and revealing the details of its shape. Thus, the distribution of the ICM can be used as a better indicator of the centre of a cluster than the distribution of the galaxies. Given the short exposures in some of the X-ray observations, we also need to be sure that the method used for calculating the cluster centre provides a robust estimate, even when the quality of the data is rather low. In this section, the adopted procedure, and the resulting determinations of the

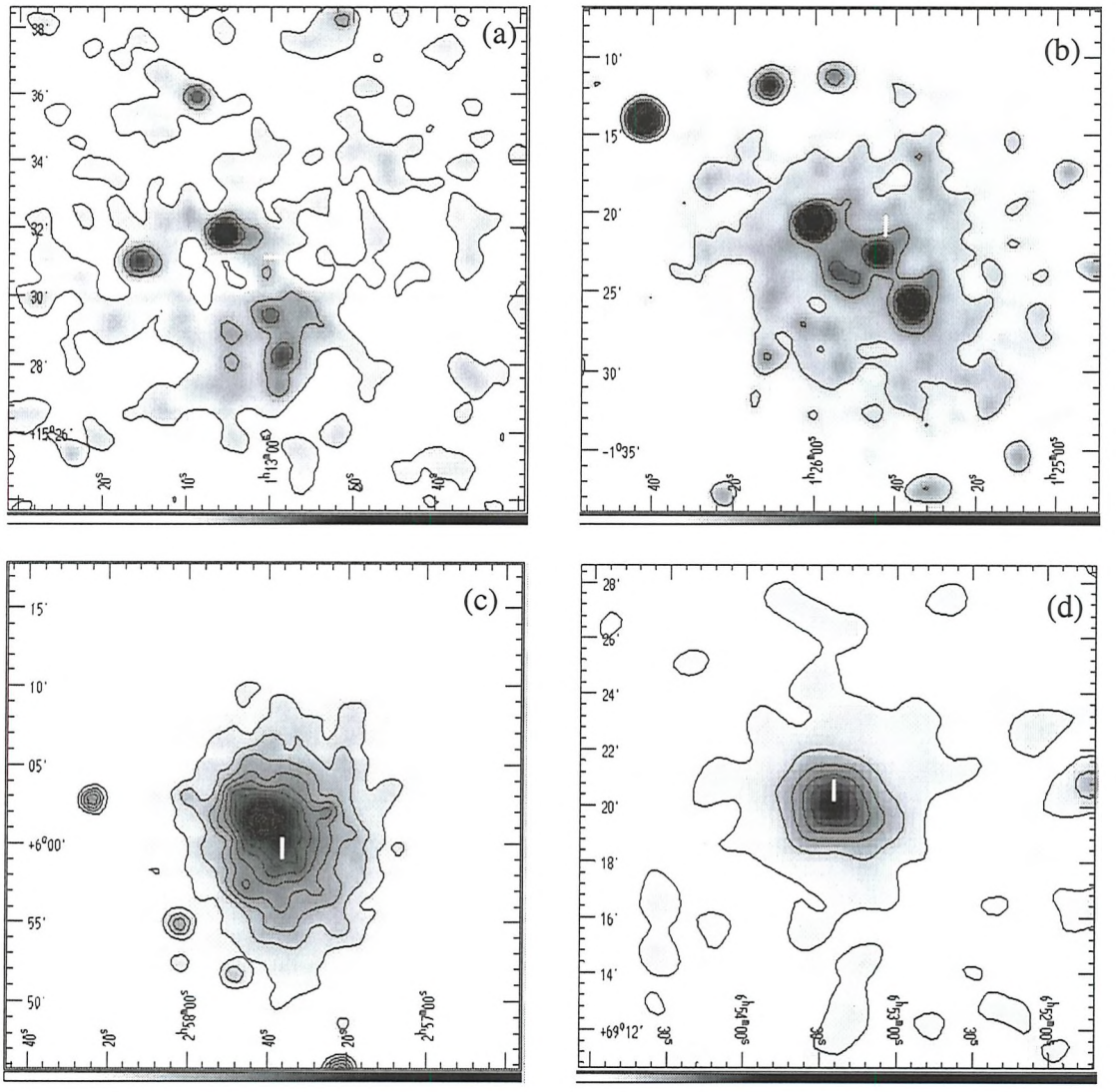

Figure 2.4: (a) Abell 160. Contour levels at 2, 2.5, 3σ (σ = 7.4 $\times$ 10^{-7} cnts s^{-1} arcsec^{-2}), (b) Abell 194. Contour levels at 2, 3, 4, 5, 6, 7σ (σ = 2.07 $\times$ 10^{-7} cnts s^{-1} arcsec^{-2} (c) Abell 400. Contour levels at 3-16σ (1σ = 1.88 $\times$ 10^{-7} cnts s^{-1} arcsec^{-2}), (d) Abell 562. Contour levels at 1, 2, 3, 4, 5, 6σ (1σ = 4.76 $\times$ 10^{-7} cnts s^{-1} arcsec^{-2}). The position of the centre of the cluster derived in § 2.4.1 is marked with crosses. A sketch showing the position and structure of the radio source is also plotted.

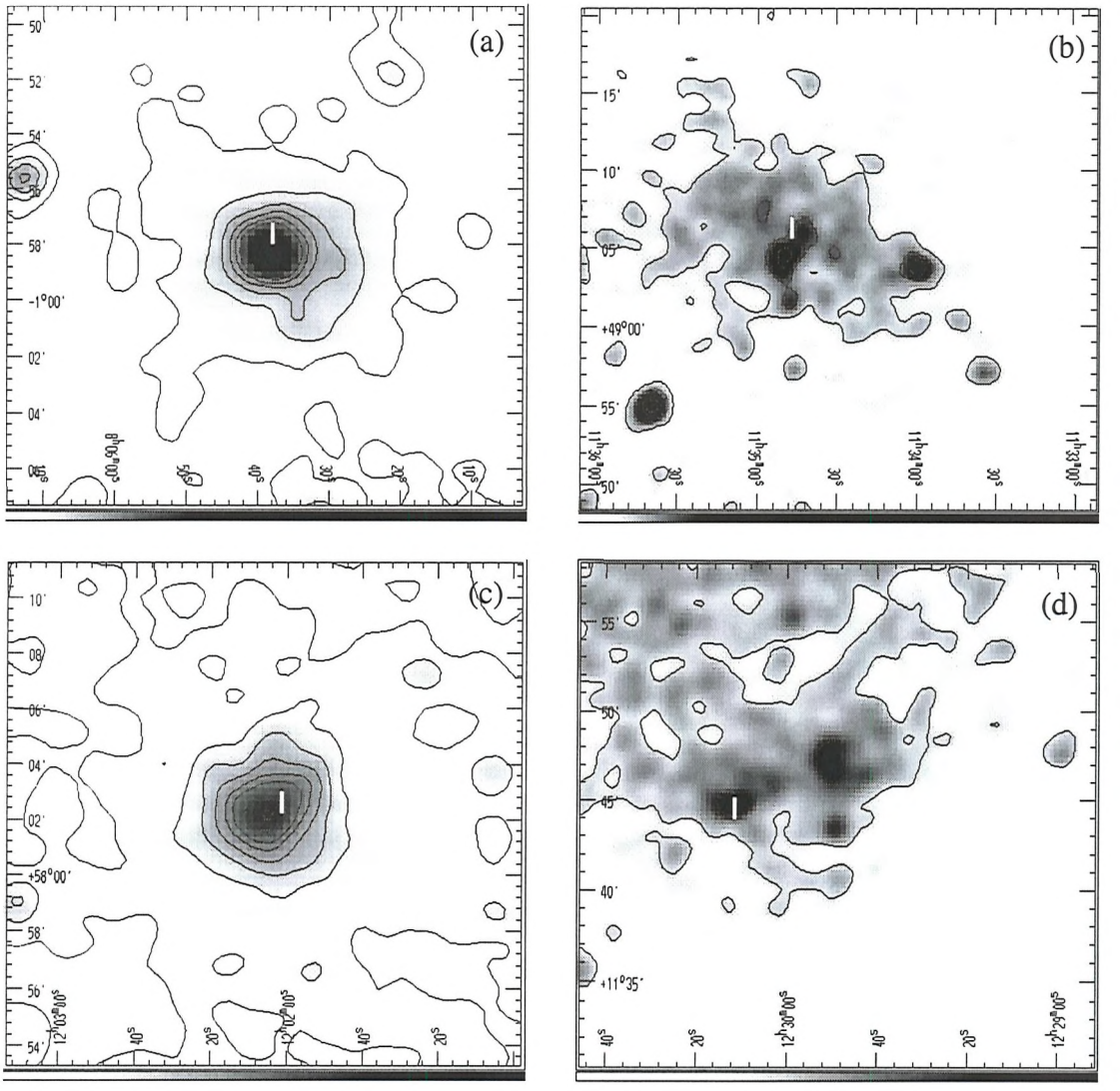

Figure 2.5: (a) Abell 623. Contour levels at 1 - 6σ ($1\sigma = 5.67\times10^{-7}$ cnts s^{-1} arcsec^{-2}), (b) Abell 1314. Contour levels at 2, 3, 4σ ($1\sigma = 7.13 \times 10^{-7}$ cnts s^{-1} arcsec^{-2}), (c) Abell 1446. Contour levels at 1-8σ ($1\sigma = 5.87 \times 10^{-7}$ cnts s^{-1} arcsec^{-2}), (d) Abell 1552. Contour levels at 1, 2σ ($1\sigma = 1.36 \times 10^{-6}$ cnts s^{-1} arcsec^{-2}). A sketch showing the position and structure of the radio source is also plotted.

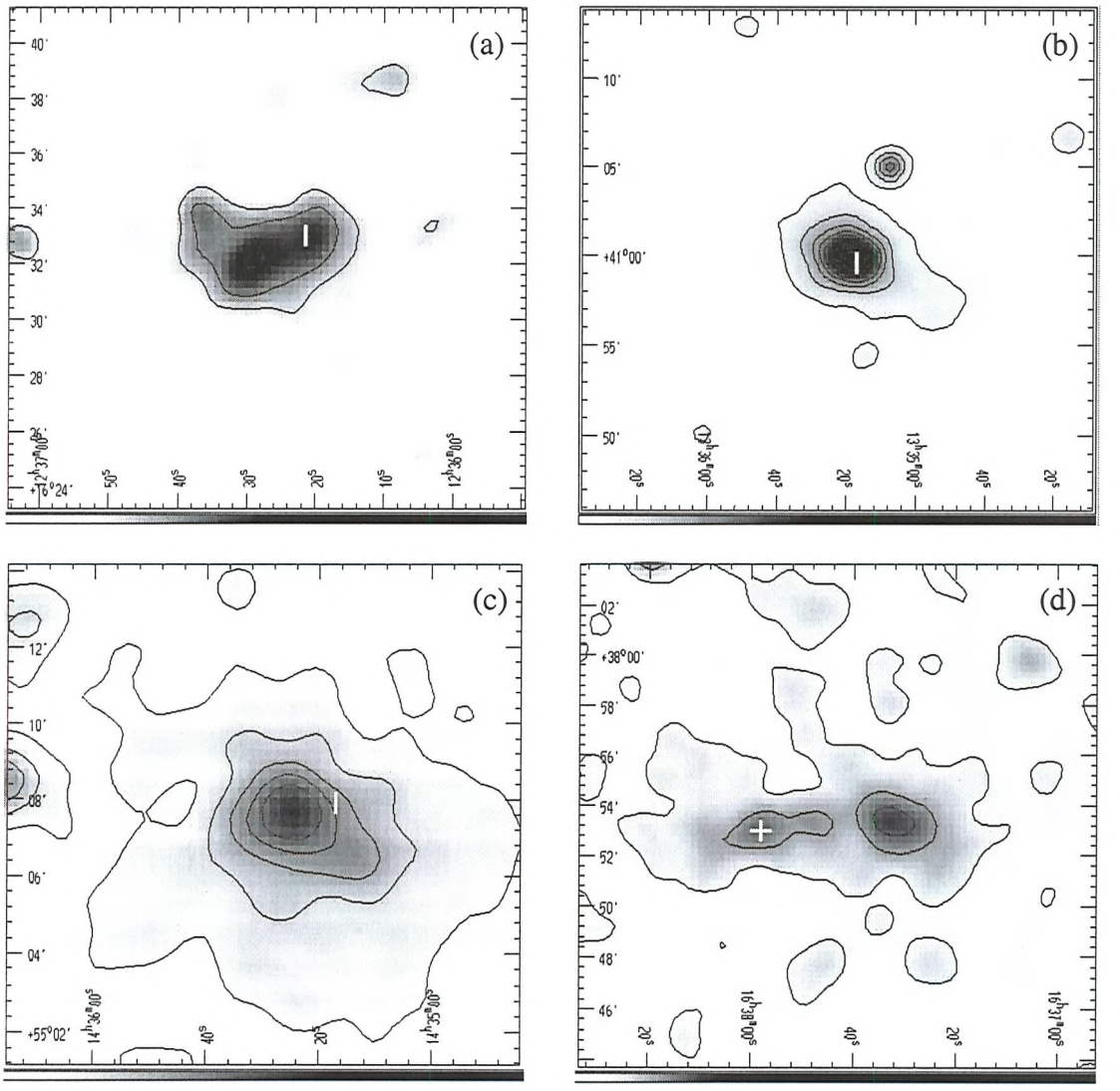

Figure 2.6: (a) Abell 1569. Contour levels at 2, 3, 4, 5, 6σ (1σ = 6.89 $\times$ 10^{-7} cnts s^{-1} $arcsec^{-2}$). (b) Abell 1763. Contour levels at 3, 6, 9, 12, 15σ (1σ = 4.17×10^{-7} cnts s^{-1} $arcsec^{-2}$). $\times 10^{-2}$ counts $arcsec^{-2}$. (c) Abell 1940. Contour levels at 1 - 6σ ($1\sigma = 6.04 \times 10^{-7}$ cnts s^{-1} $arcsec^{-2}$). (d) Abell 2214. Contour levels at 1, 2, 3σ ($1\sigma = 4.88 \times 10^{-7}$ cnts s^{-1} $arcsec^{-2}$). A sketch showing the position and structure of the radio source is also plotted.

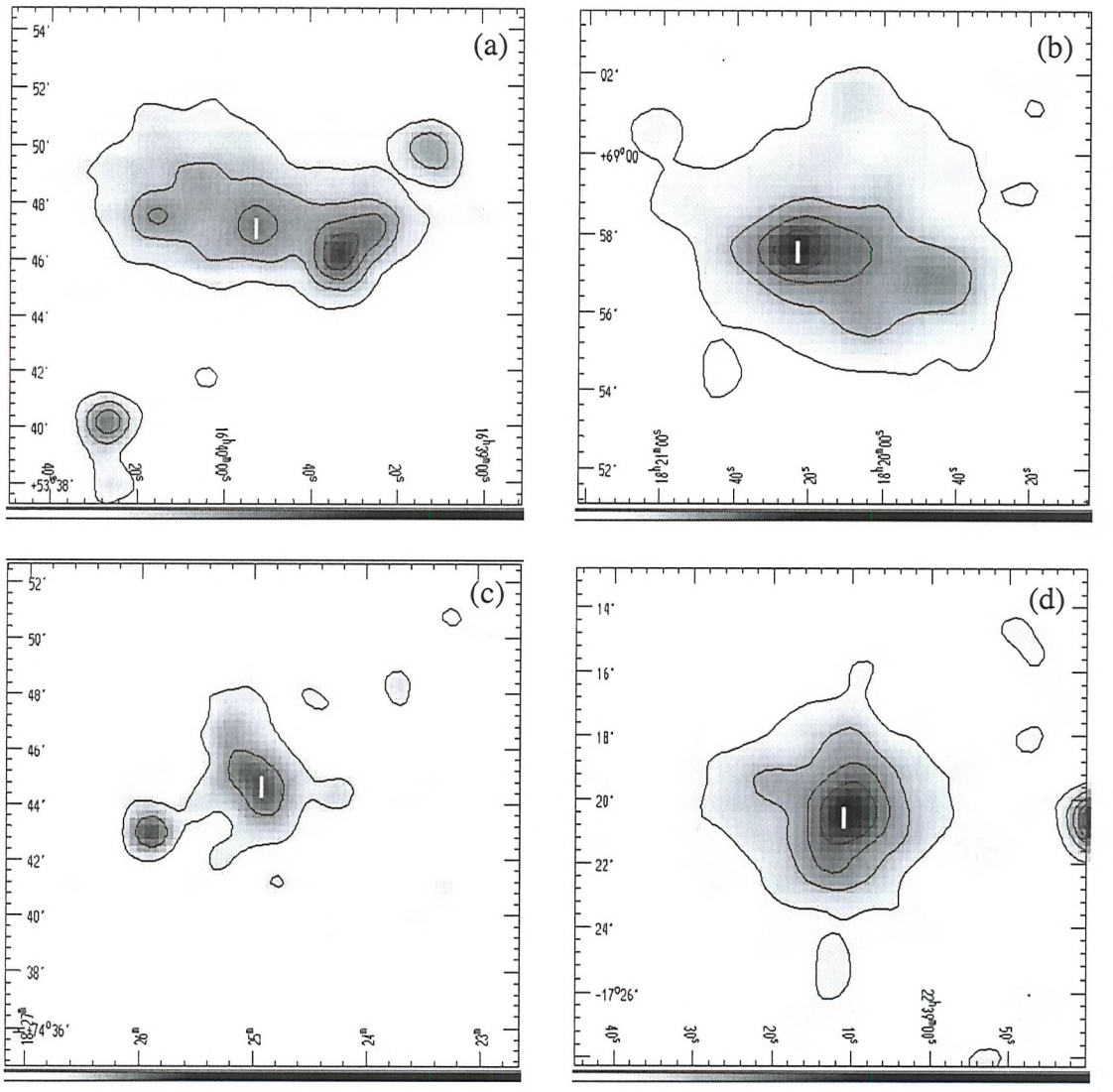

Figure 2.7: (a) Abell 2220. Contour levels at 2, 3, 4, 5σ (1σ = 2.08 × 10^{-7} cnts s^{-1} arcsec^{-2}). (b) Abell 2304. Contour levels at 1, 2, 3, 4σ (1σ = 5.38 × 10^{-7} cnts s^{-1} arcsec^{-2}). (c) Abell 2306. Contour levels at 1, 2σ (1σ = 1.12 × 10^{-6} cnts s^{-1} arcsec^{-2}). (d) Abell 2462. Contour levels at 1 - 5σ (1σ = 5.89 × 10^{-7} cnts s^{-1} arcsec^{-2}). A sketch showing the position and structure of the radio source is also plotted.

Table 2.4: X-ray results

(1)	(2)	(3)	(4)	(5)	(6)	(7)	(8)
	CLUSTER CENTRE		Positional				
CLUSTER	RA	DEC	error	d	r_c	θ	$\sigma_{\|\theta\|}$
	(1950)	(1950)	(arcsec/h_{50}^{-1}kpc)	(arcmin/h_{50}^{-1}kpc)	(h_{50}^{-1}kpc)	(degrees)	(degrees)
A160	01 10 20.2	+15 15 04.6	25/32	1.49/115.3	–	−111.1	15.5
A194	01 23 10.5	−01 36 34.6	30/16	4.27/133.2	296±39	2.3	6.8
A400	02 54 57.7	+05 47 40.1	30/21	2.25/93.1	236±5	−0.2	12.7
A562	06 47 57.9	+69 24 08.1	5/16	0.68/130.6	185±17[g]	39.1	7.0
A569	–	–	–	–	–		
A623	08 03 05.1	−00 48 50.0	30/76	0.88/133.6	174±61[g]	96.7	29.6
A1314	11 32 04.5	+49 23 03.4	20/20	8.33/489.8	322±40	35	2.3
A1446	11 59 27.3	+58 19 25.2	5/15	0.70/126.4	332±16[g]	−13.5	6.8
A1552	12 27 39.5	+12 01 12.0	–	6.16/905.5	–	−14.5	–
A1569	12 33 50.5	+16 49 31.7	40/20	1.34/183.3	289±174[g]	−3.3	6.2
A1763	13 33 06.5	+41 15 09.3	–	0.62/246.6	428±10	176.1	–
A1890	14 15 05.4	+08 26 39.8	50/83	0.70/69.7	301±130	110.8	50.0
A1940	14 33 43.4	+55 21 00.9	15/61	1.64/399.5	257±123[g]	143.5	8.7
A2214	16 36 13.3	+37 58 54.3	–	0.48/134.8	337±41[g]	36.1	–
	16 35 47.2	+37 59 13.9	–	5.63/1580.9		33.9	–
A2220	16 38 44.6	+53 52 54.7	–	2.99/577.7	328±43	−4.2	–
A2304	18 20 43.4	+68 56 03.5	–	3.84/589.8	311±34[g]	20.2	–
A2306	18 26 26.8	+74 42 48.1	20/74	0.74/164.3	133±16[g]	−8.0	24.2
A2462	22 36 29.7	−17 36 11.9	10/20	0.15/18.3	260±17[g]	143.6	47.5
A2634	23 35 53.6	+26 43 56.8	15/14	1.78/99.3	310±16	155.7	8.0
A2637	–	–	–	–	–		

[g] calculated using Gómez et al. (1997b) values for the core radii (see text).

cluster centre location are discussed.

In most cases, bright point sources are projected on the X-ray images of the clusters (Figures 2.4 and 2.5), in addition to the emission from the hot ICM. These sources were removed by setting the counts in a region of the appropriate size around each point source to the average counts detected just outside that region. Subsequently, the emission from the central region of the cluster was projected onto the two perpendicular x- and y-axes of the image. Then, the counts in each projected axis were fitted by a Gaussian function. During each fitting procedure the amplitude, width, and centre of the Gaussian were left as free parameters. The best fit model provided, along with the best value of the other free parameters, the centre of the Gaussians in each axis. These values correspond to the centre of each cluster. The calculated centres are presented in Table 2.4 [columns (2), (3)]. This procedure also gave the errors of the determined cluster centre, which are also listed in Table 2.4 [column (4)]. The results and their position on the X-ray images were also examined by eye, to make sure that the adopted centre had not been influenced by any residuals from the subtraction of the point sources.

In a few cases, as is described in more detail in the notes for each individual source in Appendix D, such a procedure proved not to be feasible, mainly because the cluster is clearly bimodal, so the whole concept of 'a cluster centre' is flawed. In such cases, the brightest peak of the X-ray emission was taken to indicate the centre of the cluster.

The centres of some of the clusters that host WATs have been previously determined by Briel & Henry (1993), Pierre et al. (1994), and Ebeling et al. (1996) using the RASS. Comparison of their results to the positions of Table 2.4 supports the concern mentioned in §2.3 that the short exposures in the RASS could lead to inaccurate determinations of the cluster centres. In several cases the centres that are given by the previously mentioned investigations coincide with the optical galaxy that hosts the radio source (e.g. A1559). Since radio galaxies are sometimes strong X-ray emitters, it is very likely that in some cases the analysis based on RASS picked up the emission coming from the galaxy instead of the centre of the ICM distribution.

One further concern is that if WATs are produced in cluster mergers, one would expect violent hydrodynamic processes to occur when the ICMs of two clusters merge. It is possible that such processes will shift the peak in the X-ray emission away from the merger remnant's mass centroid, so that it does not provide a good measure of the cluster centre. Hydrodynamic simulations of merging clusters of galaxies (Roettiger, Stone & Mushotzky 1997, and references there-in) confirm that such shifts do occur. However, even for the most extreme case of a collision between two equal-mass clusters, the shift is much less than the cluster core radius. As we shall see below, such shifts are small compared to most other distances in this analysis, so the X-ray centroid still provides a satisfactory measure of a cluster's centre of mass.

2.4.2 Size of the cluster

The WAT radio sources presented here are located in a variety of environments, from relatively poor clusters of richness R=0 up to rich (R=3) systems (Table 2.2). The extent of the clusters might be expected to vary accordingly. Therefore, results from different clusters that are to be compared should be scaled to the size of the cluster. In this study, where the impact of the ICM on the jets is also of interest, a sensible scale-length is provided by the core radius of the distribution of the ICM (see Appendix A).

Core radii of some of the clusters that host the WATs have been previously measured by Gómez et al. (1997b), using the *ROSAT* PSPC observations. They fitted the surface brightness distribution of each cluster by the traditional β-model (Appendix A), leaving the central surface brightness, the core radius, and the β parameter to be determined by the fit. Their calculated values for the core radii (r_c), converted

from their cosmology to the one used here, are given in Table 2.4 denoted by g. The presented values are also corrected for the different β-values used for each individual cluster to fit the surface brightess profile. All the given values for the core radii correspond to β=0.65. The formula given by Worrall & Birkinshaw (1994) wa used for this conversion.

For the remainder of the clusters, whose X-ray observations have not been previously analysed, a similar analysis was performed. Counts were integrated in concentric annuli, centered on the cluster centre found in § 2.4.1. The width of each annulus was different for each cluster, depending on the number of photons detected. All the point sources lying on the image of the clusters were masked out. The radial profile was then fitted by the β-model. The background was not subtracted, but left as a free parameter to be determined by the fit. The limited integration time for most of these observations prevented us from satisfactorily fitting for both β and r_c, so the β index was held fixed to $\beta = 0.65$, which is an average value for this parameter found from the study of other similar clusters (Jones & Forman 1984). Figure 5.3 shows the surface brightness distribution of these clusters. The solid line represents the best fit model. The χ^2 of each fit is also shown, and the calculated core radii are given in Table 2.4.

In some cases the β-model does not seem to match the exact distribution of the ICM. However, only the gross characteristics of the clusters are of interest, and in particular, a measure of the size of the distribution of the ICM, in order to place the WAT at the correct relative radius in the cluster. There is no intention to use the results of the present spatial analysis for more in-depth investigation of other properties of the ICM, which would require much longer observations than the ones available, and more sophisticated model fitting.

2.5 Spatial distribution of WATs in the clusters

It has been long known that radio galaxies in clusters of galaxies have a tendency to reside near the centre of the cluster. One of the first surveys of radio sources in Abell clusters and investigation of their properties in connection with their environment (M^{c}Hardy 1979) revealed their strong concentration towards the cluster centre. This result has been further confirmed by the recent radio survey of Abell clusters by Ledlow & Owen (1995a). The latter study also pointed out that this tendency might be the result of dynamical friction. When a galaxy is moving in a cluster of galaxies, it experiences a drag force by the material that is deflected by its gravity

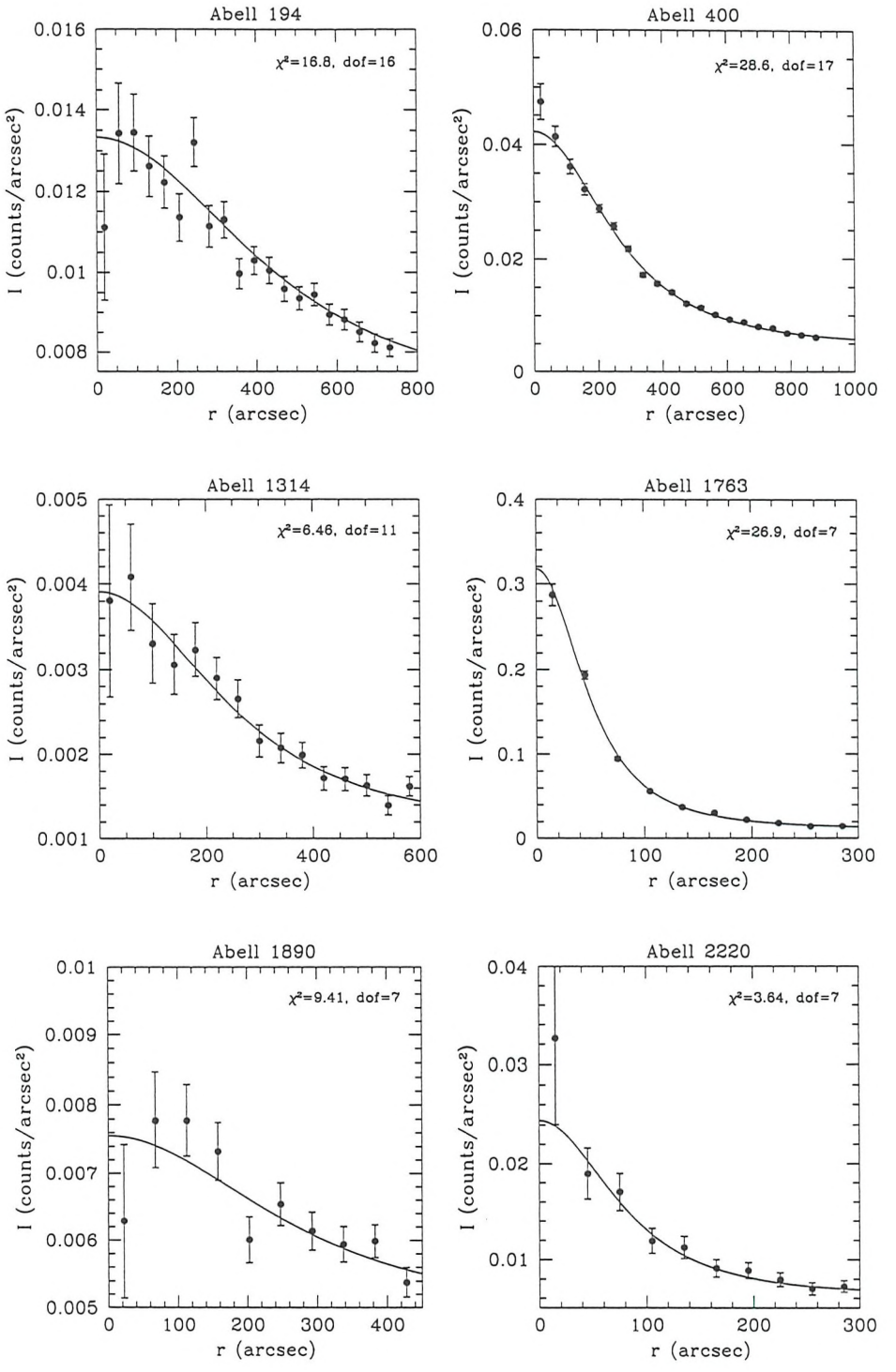

Figure 2.8: Radial surface brightness profile of six of the clusters that contain WAT sources. Most of them are obtained from *ROSAT* PSPC observations. Only Abell 1890 was observed by the HRI detector. The solid line represents the best fit model. The χ^2 of each fit is also given, along with the degrees of freedom.

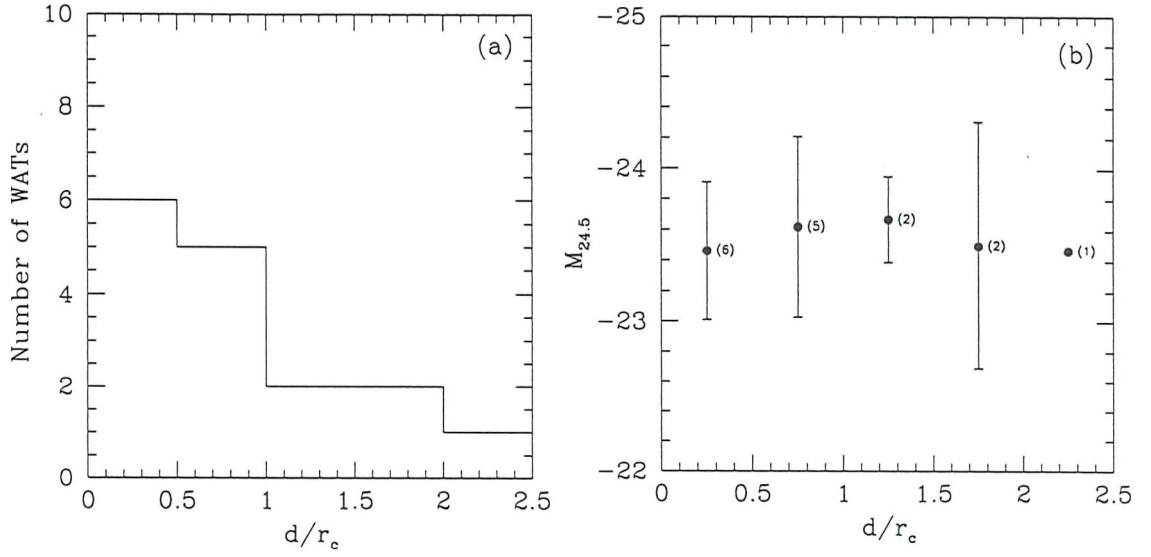

Figure 2.9: (a) The distribution of distances of the WAT sources from the cluster centres, measured in units of the clusters' core radii. (b) The average absolute magnitude of the galaxies that host the WAT sources plotted versus the distance from the cluster centre. The number of sources used to calculate the mean value of the magnitude in each distance bin is also given.

and concentrated behind it. Like an ordinary frictional drag, dynamical friction is proportional to the mass of the galaxy. As the galaxy loses kinetic energy, it spirals towards the minimum of the gravitational potential of the cluster. The more massive the galaxy, the larger the dynamical friction, the faster the galaxy settles towards the cluster centre. Ledlow & Owen (1995a) found a significant decline in the absolute optical magnitude of the radio galaxies in their sample with the distance from the cluster centre, which indicated that dynamical friction may indeed be at work.

One would expect that the WATs, which constitute a subset of these radio galaxies, being on average optically brighter and bigger than the galaxies in Ledlow & Owen's sample (Fig. 2.1), would be more strongly concentrated around the cluster centre.

Having measured the X-ray location of a cluster's centre, the offset between the location of the WAT and the cluster centre can be quantified. The measured distances are presented in Table 2.4 [column (5)]. Their distribution, scaled with the core radius of each cluster, is presented in Fig. 2.9 (a). Contrary to our expectations, WATs are spread over a wide range of distances from the cluster centre. In fact, this figure does not include the most extreme case of Abell 2214, where the WAT lies at ~ 6 core radii. It should also be borne in mind that this result is even more dramatic once projection

effects are taken into account, since they tend to place WATs closer to the cluster centre than they are in 3 dimensions. However, in order to assess the significance of this result, detailed comparison of the profile given in Fig. 2.9 (a) with a distribution similarly derived for non-WAT galaxies is required.

Further confirmation that the WATs do not represent anything close to an equilibrium population comes from Figure 2.9 (b). If the bright galaxies that host WATs have been in a rich cluster environment for a considerable period, then dynamical friction should have dragged them toward the cluster centre. As explained earlier in this section, dynamical friction operates most effectively on the most massive galaxies. If, as seems reasonable, the most massive galaxies are the brightest, then one would expect the more centrally concentrated WAT host galaxies to be the brightest. The absence of any such trend in Figure 2.9 (b) suggests that these systems have not been around long enough for dynamical friction to be an important force, and hence that the whole WAT phenomenon might be a transient one.

2.6 Motion of WATs in clusters

The results of the previous section indicate that the galaxies which host WATs lie far from the minima of the gravitational potentials of their clusters. They must therefore be in motion relative to it. In this section we attempt to decipher their orbits. A useful tool is available for this task: the direction in which the jets are bent. If the jets of these radio galaxies are indeed bent by the ram pressure resulting from the motion of the galaxy through the ICM, this motion is traced by the direction in which the jets are bent. This information has been previously used and its limitations studied by O'Dea, Sarazin & Owen (1987). They explored the dynamics of clusters using the more dramatically bent radio galaxies known as NATs.

The parameter of interest for such an investigation is the angle between the vector connecting the cluster centre and the position of the radio galaxy, and the vector that bisects the angle between the two radio lobes. This angle θ (Fig. 2.10) is measured counterclockwise from the radius vector that connects the cluster centre with the optical galaxy. Such a definition assigns the angles 0 and 180 degrees to sources which move radially inwards and outwards from the cluster centre respectively. The calculated values for θ are presented in Table 2.4 [column (7)].

The error in θ mainly depends on the accuracy of the position of the cluster centre. The position of the optical galaxy has been measured with an accuracy of 1 arcsec (Ledlow & Owen 1995b). For the sources for which a measurement of the error for

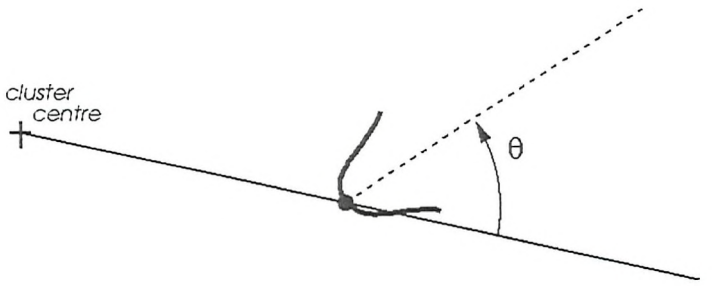

Figure 2.10: Sketch of the WAT and cluster geometry illustrating the definition of the angle θ.

the position of the cluster centre exists, the error in θ was calculated and presented in column (8) of Table 2.4. Generally, the largest inaccuracies of θ correspond to sources which lie very close to the cluster centre, since a small change in the position of such a source corresponds to a large change in angle.

Figure 2.11 shows the distribution of θ for the WAT sources in this sample. Since the geometry is symmetric about $\theta = 0$, the absolute value of θ ($|\theta|$) is plotted, with the angle θ defined in the range $-180 < \theta < 180$ degrees. This plot gives the impression that there is a strong concentration of angles around 0 degrees. In the next section the possible orbits that galaxies in clusters follow are discussed, and the predicted distributions of the angles θ for each model orbit is compared to the observed distribution of Fig. 2.11.

2.6.1 Galaxy orbits

Orbits of galaxies in clusters reflect the history of cluster formation as well as the importance of various dynamical processes in the evolution of clusters. For example, violent relaxation results in isotropic orbits, without the galaxies having a preferred direction of motion. Predominance of radial orbits, on the other hand, indicates that the cluster has undergone spherical collapse (Gunn & Gott 1972), or it has suffered mergers accreting material from its surroundings on radial orbits.

If the orbits were entirely random and isotropic one would expect to observe any angle θ, defined in the previous section, with equal probability. When the distribution of the angles of WATs is compared with such a uniform distribution using the KS test [Fig. 2.12 (a)] the possibility that the WATs of the present sample are moving in

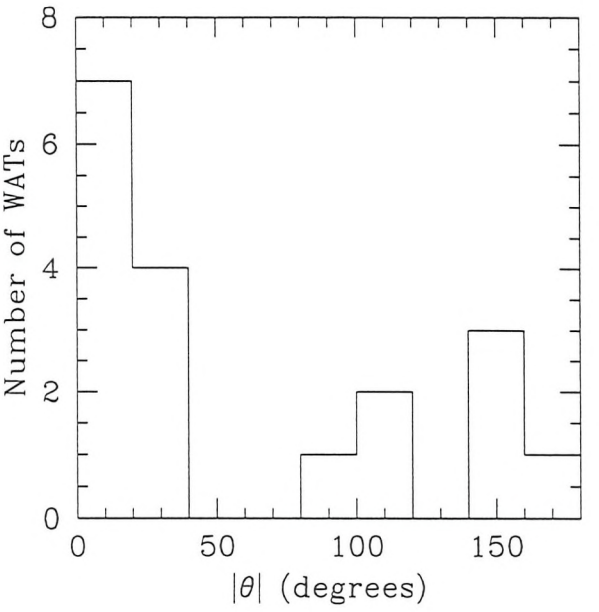

Figure 2.11: The distribution of the observed angles for all the 18 WATs.

random orbits is rejected at the 99.90% confidence level. Thus, the spike at $|\theta| \sim 0$ is statistically significant, and allows us to confidently rule out the possibility that WATs follow purely random orbits.

Galaxies might also move in circular orbits around the cluster centre. The distribution of θ that one would expect for circular orbits is somewhat more complicated due to projection effects, which make circular orbits appear radial. O'Dea et al. (1987) have quantified this distribution. They found that the expected number of galaxies has a minimum at $|\theta| = 0$ degrees, and rises to a sharp maximum at $|\theta| = 90$ degrees, before dropping back to a minimum at $|\theta| = 180$ degrees. Figure 2.12 (b) compares the cumulative distribution of the observed angles for WATs with the model distribution of O'Dea et al. (1997). The KS test rejects the possibility that the orbits of WATs are circular at a higher significance level than previously (99.99%) for the isotropic orbits.

Having ruled out the possibilities that WATs are moving randomly or in circular orbits, it is apparent that they must follow preferentially radial orbits. If the orbits were purely radial, the distribution of θ should consist of delta-function spikes at θ=0 and 180 degrees. Since there are observational uncertainties in the values of θ, it is expected that the distribution is broadened. The presence of a few WATs with

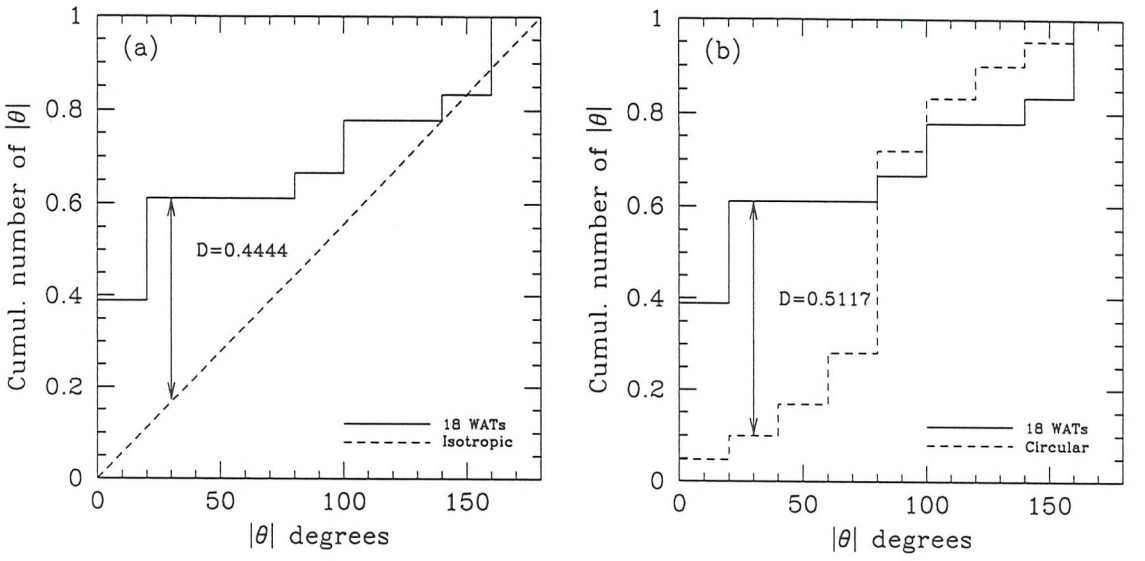

Figure 2.12: The cumulative distribution of the observed angles for the 18 WATs along with the model distribution for isotropic (a), and circular (b) orbits.

intermediate values of θ implies that the orbits cannot be completely radial.

This result provides a first indication that the galaxies which host WATs are currently falling towards the centres of their clusters. In such a scenario the presence of a few WATs with intermediate values of θ, as seen in Fig. 2.13 can be understood. It is apparent from Figure 2.13 that the WATs at intermediate angles lie within one core radius, significantly smaller than the radii of the majority of WATs. As a WAT falls in from large radii, it will have initially $|\theta| \sim 0$ degrees. As it sweeps through the core of the cluster, it will briefly travel tangentially to the cluster centre with $|\theta| \sim 90$ degrees, being deflected by interactions with other galaxies. Afterwards it will start heading approximately radially outward, with $|\theta| \sim 180$ degrees.

2.6.2 In-coming versus out-going galaxies

According to the definition of the angle θ, sources which are moving towards the cluster centre (in-coming) have $|\theta|$ around 0 degrees, while the ones with $|\theta|$ around 180 degrees are moving away from it (out-going). One might expect no preference in the direction of these galaxies; as many galaxies should lie on the inward parts of their orbits as the outward parts. However, as can be seen from Table 2.4 and Fig. 2.14, there are more WATs that are directed towards the cluster centre: for the WATs that are nearly in radial orbits, there are $n_{\rm in} = 11$ in-coming galaxies, and only

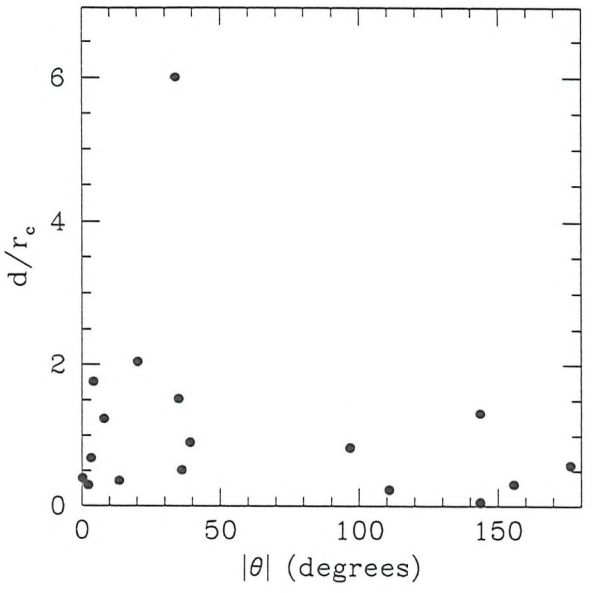

Figure 2.13: The distance of each WAT source from the cluster centre versus the angle of its jets. The WATs in Abell 160 and Abell 1552 are not included because the present X-ray data do not permit the measurement of the core radius of the ICM distribution.

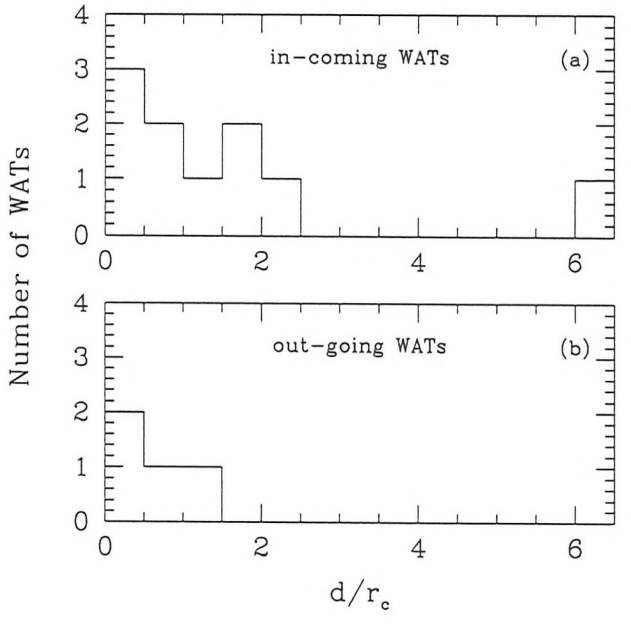

Figure 2.14: The distribution of distances from the cluster centre (a) for in-coming sources, and (b) for out-going ones.

$n_{\rm out} = 4$ out-going WATs. If the probabilities of a WAT going towards the cluster and outwards were equal ($p = p_{\rm in} = p_{\rm out} = 0.5$), the binomial distribution gives that there would be only 6% probability to observe more than 11 sources out of the 15 moving inward. Therefore, the difference between the observed number of in-coming and outgoing WATs is significant at a level of more than 90%.

This imbalance can be understood in terms of the model in which the WAT is produced by the infall of a small group containing a radio galaxy. As such a galaxy initially falls into the cluster, it will form a WAT. However, when it runs into the cluster core, it encounters a high density ICM which may disrupt its relatively delicate radio lobes. Further, the high density of galaxies in the cluster core makes it likely that the WAT will undergo a close encounter with another galaxy. These processes are likely to distort the well-defined C-shape of the jets, so that it will no longer be classified as a WAT. Thus, fewer WATs will emerge on the far side of the cluster than fell inward in the first place. Crudely speaking, we can quantify this effect by assuming that a WAT has a probability p of being disrupted each time it passes through the cluster core. The number of sources which will be identified as such after the first crossing will be $n_{\rm in}(1-p)$, and after n crossings this number will be $n_{\rm in}(1-p)^n$. Therefore the observed fraction $n_{\rm in}/n_{\rm out}$ is:

$$p = 1 - \frac{n_{\rm out}}{n_{\rm in}}, \tag{2.1}$$

and hence that $p \sim 0.6$. Thus, it would appear that the disruptive processes in the cluster core are quite efficient, and few WATs survive to make multiple orbits.

In Fig. 2.13 the angle $|\theta|$ for each individual source is plotted against the distance of the source from the cluster centre. This figure gives the impression that the out-going WATs are found closer to the cluster centre than the in-coming ones. Figures 2.14 (a) and (b) show the distribution of in-coming and out-going WATs respectively. The in-coming WATs with measured values of r_c lie at a mean radius of $(1.5 \pm 0.5) r_c$, while the 4 out-going have a corresponding mean radius of $(0.6 \pm 0.3) r_c$. Applying Student's t-test to these data, it was found that the two means are significantly different at the 95% confidence level. However, it should be realized that this result is not very robust: if the single in-coming WAT with $d = 6r_c$ (in Abell 2214) is excluded, then the difference ceases to be statistically significant.

Braking of a galaxy while it is crossing the central region of a cluster, where the number densities of both the ICM and the galaxies is high, might be expected. Dynamical friction and ram pressure decelerate the galaxies, which after crossing the

cluster centre do not have enough kinetic energy to travel away from it. This effect has been successfully demonstrated by recent numerical simulations. Frenk et al. (1996) follow numerically the formation and growth of a Coma-like cluster of galaxies by the accumulation of smaller units which lie around the forming cluster. They also present the orbits of the infalling galaxies. As they demonstrate, the bigger the galaxy the quicker it settles down at the minimum of the cluster's gravitational potential, and therefore in-coming galaxies are expected to be on average at larger distances than the out-going ones.

2.7 Summary and Discussion

A sample of WAT radio sources in Abell clusters has been defined in order to investigate their origins by quantifying their spatial distribution and orbital motion in clusters of galaxies. X-ray observations, retrieved from the archive of the *ROSAT* satellite, have been used to define more accurately and objectively the centre and size of the clusters that host the WATs.

The basic findings from this data set are as follows:

1. WATs are not generally located at the centres of their host clusters as defined by their X-ray emission. They are found over a range of distances from the cluster centre, out to several core radii.

2. If their bent shape can be attributed to ram pressure, then WATs are found to lie preferentially on radial orbits.

3. There are more WATs travelling toward the centres of their host clusters than there are systems moving away from the centres.

4. There are indications that WATs travelling toward the centres of clusters lie at larger radii on average than those travelling outward.

In-depth analysis of X-ray observations of some of the clusters that host WATs by Gómez et al. (1997b), Schindler & Prieto (1997), and Sakelliou et al. (1996) reveals the complexity of the X-ray emission from the ICM. The X-ray images of these clusters show the presence of substructure, including an elongation of the distribution of the ICM, which coincides with the direction in which the jets are bent. Optical observations also uncover the complexity of the velocity field of these clusters (Pinkney 1995; Gómez et al. 1997b).

These findings are totally consistent with a model in which WATs are produced when a radio galaxy falls into a rich cluster. The WATs' location away from the centres of clusters reflects the large radius from which they are being captured, and the inferred nature of their orbits fits with a simple radial infall. The excess of incoming over out-going WATs indicates that an infalling WAT is frequently disrupted as it passes through the cluster core. The smaller radii at which out-going WATs are found suggests that WATs are also significantly decelerated by dynamical friction as they pass through the cluster core.

This scenario fits extremely well with the current understanding of galaxy cluster formation. Cosmological simulations show that a rich cluster forms from the repeated merging of poor groups (e.g. Frenk et al. 1996). Any large galaxy that is captured in one of these mergers falls radially inward to the cluster centre, where it is rapidly decelerated to rest (Frenk et al. 1996). Any late-arriving large galaxies in poor groups will be undergoing this merger process today. Although difficult to detect, there is increasing evidence that big galaxies are not situated at the centres of their associated clusters, even in the cases of regular clusters (e.g., Lazzati & Chincarini 1998). WATs are simply those systems that happened to have been radio galaxies before they fell into the cluster.

Chapter 3

The Galaxies in Abell 2634

3.1 Introduction

The advent of the *Einstein* observatory changed the belief that early-type galaxies contain little interstellar gas by revealing hot X-ray emitting halos associated with many of them (e.g. Forman et al. 1979). Subsequent X-ray observations led to the conclusion that these galaxies can retain large amounts (up to $\sim 10^{11} M_{\odot}$) of hot ($T \sim 10^7$ K) gas (Forman, Jones & Tucker 1985; Trinchieri & Fabbiano 1985; Canizares, Fabbiano & Trinchieri 1987).

However, this picture might be different for galaxies that reside near the centres of rich clusters of galaxies, since their properties must be affected by their dense environment. For example, interstellar medium (ISM) might be stripped from the galaxy by the ram pressure resulting from the passage of the galaxy through the intracluster medium (Gunn & Gott 1972). Stripping of the ISM can also result from tidal interactions with other nearby galaxies (Richstone 1975; Merritt 1983, 1984). The most dramatic and well-studied example of a galaxy which appears to be in the process of being stripped of its ISM is the elliptical galaxy M86 in the Virgo cluster, which shows a 'plume' of X-ray emission emanating from it (Forman et al. 1979; White et al. 1991; Rangarajan et al. 1995).

In addition to the mechanisms which remove the ISM of a galaxy, gas can also be replenished. The gravitational pull of a galaxy attracts the surrounding ICM. This gas ends up being concentrated in or behind the galaxy, depending on the velocity of the galaxy relative to the ICM (see, for example, Sakelliou, Merrifield & McHardy 1996). Stellar winds can also replenish the hot gas in a galaxy's ISM.

All the processes mentioned above take place simultaneously. The relative importance of each process depends on: the galaxies' velocities; the local density of the

ICM; the number density of galaxies; their orbits in the cluster; and the gravitational potential of each galaxy. It is therefore *a priori* difficult to say which mechanism dominates in the cores of rich clusters of galaxies, and hence whether cluster galaxies are surrounded by the extensive X-ray emitting halos that we see associated with galaxies in the field.

Unfortunately, X-ray observations of rich clusters have generally not been of high enough quality to answer this question, since any emission from the galaxies is hard to detect against the high X-ray background produced by the cluster's ICM (Canizares & Blizzard 1991; Vikhlinin, Forman & Jones 1994; Bechtold et al. 1983; Grebenev et al. 1995; Soltan & Fabricant 1990; Mahdavi et al. 1996). In the cases where galaxy X-ray emission has been reported, the studies have been restricted to a few bright cluster galaxies, and it has not proved possible to investigate the general galaxy population in a statistically complete manner.

In order to search for X-ray emission from galaxies in a moderately rich environment, a deep *ROSAT* HRI observation of the core of the rich cluster Abell 2634 was obtained. Abell 2634 is a nearby (z=0.0312) centrally-concentrated cluster of richness class 1. The optical image of the central part of the cluster is dominated by the presence of the big cD galaxy NGC 7720, which hosts the WAT radio source 3C 465. More information on the appearance and dynamics of Abell 2634 and the WAT 3C 465 can be found in chapter 4. The remainder of this chapter is laid out as follows. Section 3.1 describes the analysis by which the X-ray emission from the galaxies in Abell 2634 was detected. In §3.2 the properties of this X-ray emission are explored, and it is shown that the galaxies in this cluster lack the extensive gaseous halos of similar galaxies in poorer environments. In §3.4 the reasons for this difference are investigated.

3.2 X-ray observations and analysis

The core of Abell 2634 was observed with the *ROSAT* HRI in two pointings, in January and June 1995, for a total of 62.5 ksec. The analysis of these data was performed with the IRAF/PROS software.

Inspection of the emission from the cD galaxy and other bright X-ray sources in the images from the two separate observations indicates that the two sets of observations do not register exactly and that a correction to the nominal *ROSAT* pointing position is required. Therefore, the second set of observations was shifted by $\sim$ 2.0 arcsec to the east and $\sim$ 0.8 arcsec to the south; such a displacement is consistent with typical *ROSAT* pointing uncertainties (Briel et al. 1996). Both images were then registered

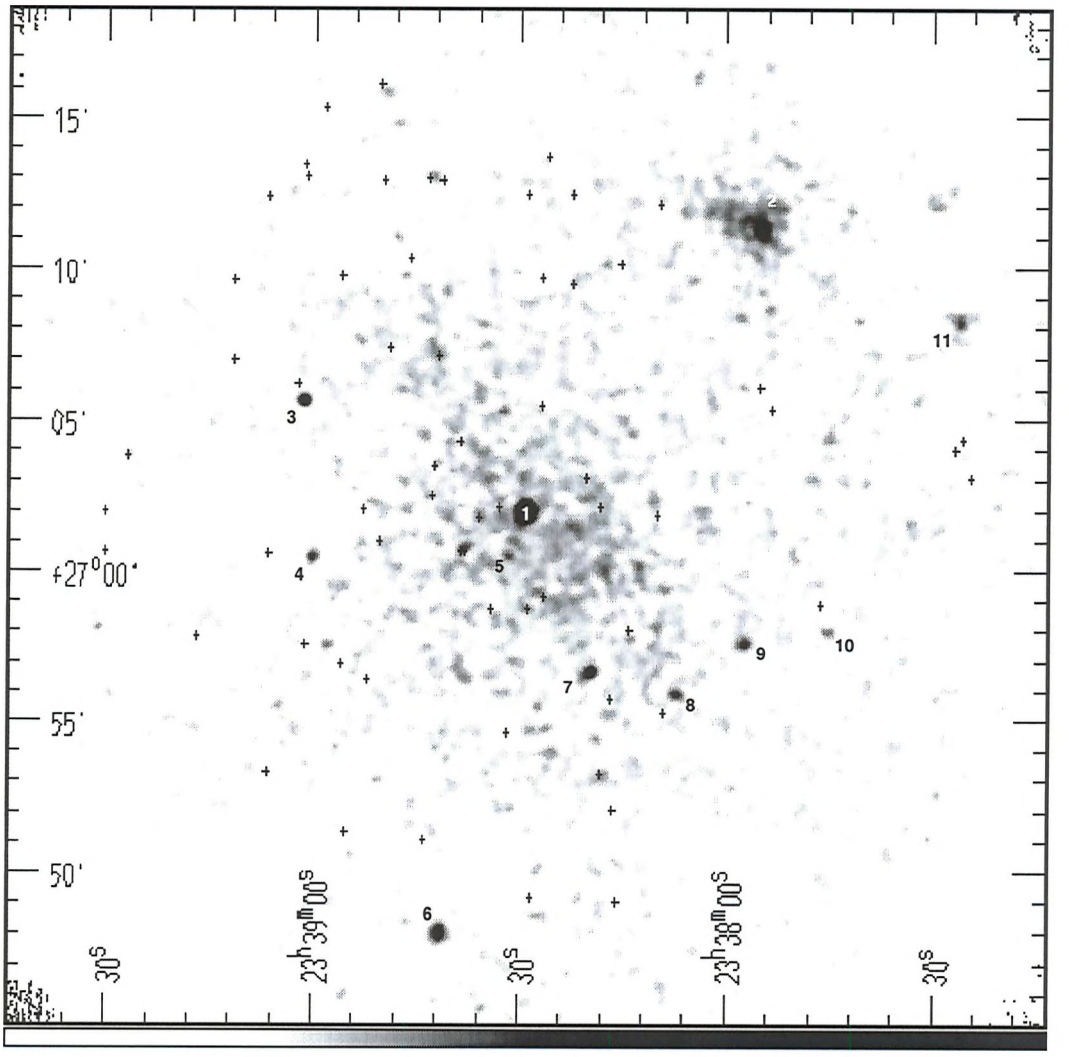

Figure 3.1: Grey-scale *ROSAT* HRI image of the core of the cluster Abell 2634. The image has been smoothed using a Gaussian kernel with a dispersion of 8 arcsec. The positions of the cluster galaxies with measured redshift are marked with crosses.

Table 3.1: Bright Sources

Source	r.a.(J2000) h m s	dec.(J2000) ° ′ ″	ID/notes
1	23 38 29.1	27 01 53.5	cD galaxy
2	23 37 56.1	27 11 31.3	cluster
3	23 39 01.6	27 05 35.9	star
4	23 39 00.5	27 00 27.9	star
5	23 38 31.7	27 00 30.5	nothing
6	23 38 41.5	26 48 04.1	star
7	23 38 19.8	26 56 41.5	?
8	23 38 07.4	26 55 52.8	star
9	23 37 57.5	26 57 30.1	galaxy ?
10	23 37 45.3	26 57 53.1	two objects
11	23 37 26.2	27 08 14.6	?

with the optical reference frame to better than an arcsecond. A grey-scale image of the total exposure is shown in Fig. 3.1. The image has been smoothed with a Gaussian kernel of 8 arcseconds dispersion. At the distance of Abell 2634, 1 arcsec corresponds to $0.9h_{50}$ kpc.

This deep image of Abell 2634 reveals the large-scale X-ray emission from the hot ICM of the cluster and a few bright sources, which are numbered on Fig. 3.1. Source 1 is the cD galaxy NGC 7720, mentioned in the introduction. Source 2 is a background cluster at a redshift of $cz \simeq 37,000$ km s^{-1} (Pinkney et al. 1993; Scodeggio et al. 1995). For the rest of the X-ray bright sources, the Automatic Plate Measuring machine, run by the Royal Greenwich Observatory in Cambridge, was used to obtain optical identifications. Table 3.1 gives the positions of these sources as determined from the X-ray image, and the class of their optical counterparts. The position of source 7 coincides with a faint object in the Palomar sky survey, but there is also a nearby star, and source 11 does not seem to have a discernible optical counterpart. All these sources were masked out in the subsequent analysis.

The positions of galaxies that are members of Abell 2634 are also indicated on Fig. 3.1. Pinkney et al. (1993) collected the redshifts of ~150 galaxies that are probable members of Abell 2634 (on the basis that their redshifts lie in the range $6,000 < cz < 14,000\,\mathrm{km\,s^{-1}}$), and Scodeggio et al. (1995) have increased the number of galaxies whose redshifts confirm that they are cluster members up to ~ 200. The sample of redshifts is complete to a magnitude limit of 16.5. From this magnitude-

Table 3.2: Cluster galaxies

(1) No	(2) NAMES	(3) r.a. (2000) h m s	(4) dec. (2000) ° ′ ″	(5) Morph. type	(6) J mag	(7) B_c mag	(8) L_B $L_\odot$ $\times 10^{10}$	(9) r_e^c arcsec
1	0226/330647	23 38 16.08	26 49 01.90	S0	16.26	-19.66	1.1	8.21
2	0228/-	23 38 28.61	26 49 06.50	E	15.23	-20.69	2.8	
3	0233/330687	23 38 44.18	26 51 02.60	E(S0^{sc})	15.88	-20.04	1.5	8.18
4	0234/-	23 38 55.58	26 51 19.50					
5	-/330645	23 38 16.67	26 52 03.60	S/I	17.13			
6	0238/330649	23 38 18.48	26 53 12.70	E	15.49	-20.43	2.2	4.76
7	0239/330713	23 39 07.05	26 53 16.00	S0				
8	0243/-	23 38 09.47	26 55 13.30					
9	0244/330646	23 38 17.19	26 55 41.30	S	17.00			
10	0246/330697	23 38 52.48	26 56 21.80	S0	16.92	-19.00	0.6	
11	0248/330701	23 38 56.39	26 56 54.60	S0				
12	0250/-	23 39 01.49	26 57 31.10	S0	17.48			
13	-/330725	23 39 17.37	26 57 47.80	S/I	17.30			
14	0253/-	23 38 14.29	26 58 02.30	S0/E				
15	0255/330615	23 37 46.65	26 58 50.60	S0	16.20	-19.76	1.2	5.93
16	0256/330667	23 38 34.47	26 58 46.00	S0	16.42	-19.50	0.9	1.57
17	0257/330660	23 38 29.21	26 58 43.10	E	15.20	-20.72	2.9	8.13
18	0259/330658	23 38 26.85	26 59 06.10	S0/D	15.20	-20.72	2.9	7.18
19	0261/-	23 39 06.85	27 00 36.00	S0				
20	0263/-	23 38 38.81	27 00 40.40	E	15.47	-20.45	2.2	
21	0264/-	23 38 50.66	27 00 56.70	S	16.64			
22	0267/-	23 38 10.22	27 01 49.40	S0				
23	0271/330668	23 38 36.28	27 01 46.50	S0	15.85	-20.09	1.6	13.67
24	0272/-	23 38 53.00	27 02 00.10					
25	0273/330648	23 38 18.62	27 02 06.80	E	17.01	-18.95	0.6	2.02
26	0275/330665	23 38 33.26	27 02 05.20	E				
27	0276/330732	23 39 30.67	27 01 55.20	S0/a	16.84	-19.08	0.6	
28	0277/-	23 38 43.10	27 02 30.80	S				
29	-/330597	23 37 24.89	27 03 02.40	S				
30	0280/330651	23 38 20.68	27 03 02.80	S0	16.70	-19.26	0.8	5.17
31	0283/-	23 38 42.65	27 03 26.30					
32	0284/330600	23 37 27.03	27 03 59.20	S0				
33	0285/-	23 39 27.41	27 03 47.50					
34	0287/-	23 37 26.01	27 04 17.30	S	15.50			
35	0288/331242	23 38 39.05	27 04 14.90		17.03			
36	0294/330621	23 37 53.68	27 05 18.40	S0(a^{sc})	16.88	-19.08	0.6	6.25
37	0295/330659	23 38 27.13	27 05 25.30	S0	16.71	-19.23	0.7	33.11
38	0296/-	23 37 55.38	27 06 01.70	SB0/a	16.57			
39	0298/330706	23 39 02.69	27 06 08.90	E	14.53	-21.41	5.5	4.31
40	0301/330686	23 38 42.07	27 07 06.80	S0	16.67	-19.27	0.8	2.53
41	0302/-	23 39 11.91	27 06 55.00	SB(s)b	15.04			
42	0303/330691	23 38 49.26	27 07 22.20	S0	16.80	-19.14	0.7	
43	0308/330653	23 38 22.75	27 09 28.90	E	15.42	-20.52	2.4	5.65
44	0311/330721	23 39 11.90	27 09 35.70	S(b^{sc})	16.51			
45	0312/330700	23 38 56.24	27 09 41.40	S0	16.34	-19.60	1.0	3.34
46	-/331097	23 38 15.70	27 10 07.10					
47	0316/330688	23 38 46.26	27 10 20.10	S0	16.51	-19.43	0.9	
48	0319/331542	23 38 29.14	27 12 24.70					
49	0320/330711	23 39 07.03	27 12 20.70	S0	16.79	-19.15	0.7	
50	0321/330679	23 38 41.72	27 12 54.10	S0	17.40	-18.54	0.4	9.05
51	0322/330694	23 38 50.11	27 12 53.50	S0(a)	15.48	-20.46	2.3	
52	0323/-	23 39 01.42	27 12 58.50	S				
53	0324/330686	23 38 43.66	27 12 54.90	S0	14.96	-20.98	3.7	14.66
54	0326/-	23 39 01.81	27 13 24.30		16.03			
55	0329/-	23 38 58.77	27 15 18.50	S0				
56	0331/330696	23 38 50.66	27 16 03.90	E	14.75	-21.19	4.5	8.64
57	1310/-	23 38 32.17	26 54 34.60	S0				
58	Z13/330678	23 38 38.38	27 00 37.40	E^{sc}				
59	Z18/-	23 39 30.53	27 00 37.70					
60	-/330636	23 38 10.01	27 12 05.08	I	16.72			
61	-/330654	23 38 22.60	27 12 25.97	S0				
62	-/331541	23 38 26.18	27 13 37.99					

NOTES: ^{sc} Scodeggio et al. (1995)

limited sample, only galaxies that appear projected within a circle of 15 arcmin radius around the cD galaxy were selected. This selection yielded 62 galaxies listed in Table 3.2. The identification number of each galaxy is presented in column (2). The first number is the coding number given by Pinkney et al. (1993), while the second one is from Scodeggio et al. (1995). The next two columns [(3) and (4)] give the positions of the galaxies, which are taken from the CCD photometry of Pinkney (1995) and Scodeggio et al. (1995), and are accurate to $\sim$ 1 arcsec. In column (5) their morphological type is listed. Columns (6) and (7) contain their J and absolute blue magnitude respectively (see §3.2.2). The effective radius r_e^c [column (9)] is taken from Scodeggio et al. (1997). As can be seen from this table, the vast majority of these galaxies are of type E and S0 – only 10 are classified as spirals or irregular. All these galaxies are marked as crosses on Fig. 3.1.

Inspection of Fig. 3.1 reveals several cases where the location of a galaxy seems to coincide with an enhancement in the cluster's X-ray emission, and it is tempting to interpret such enhancements as the emission from the galaxy's ISM. However, it is also clear from Fig. 3.1 that the X-ray emission in this cluster contains significant small-scale fluctuations and non-uniformities. Therefore, there is the possibility that the apparent associations between galaxy locations and local excesses in the X-ray emission may be chance superpositions. For this reason a more objective approach to searching for the X-ray emission from cluster galaxies is required. Such an investigation is presented in the following section.

3.2.1 Detection of the cluster galaxies

Before adopting an approach to detecting the emission from cluster galaxies, we must first have some notion as to how bright the emission is expected to appear in this deep HRI image. Previous X-ray observations have shown that the X-ray luminosities of E and S0 galaxies in the 0.2-3.5 keV energy band range from $\sim 10^{39}$ to $\sim 10^{42}$ erg s^{-1} (Kim, Fabbiano & Trinchieri 1992a, b; Forman et al. 1985). These limits at the distance of Abell 2634 correspond to fluxes of 5×10^{-16} to 5×10^{-13} erg s^{-1} cm^{-2}. The PIMMS software was used to convert these limits to count rates for the *ROSAT* HRI detector. The emission from the galaxies was modelled by a Raymond-Smith plasma (Raymond & Smith 1977) with a temperature $kT = 0.862$ keV and a metal abundance of 25% solar; these quantities are consistent with the values previously found from observations of early-type galaxies (Kim et al. 1992a; Matsushita et al. 1994; Awaki et al. 1994). The absorption by the galactic hydrogen was also taken into account by using the column density given by Stark et al. (1992) for the direction

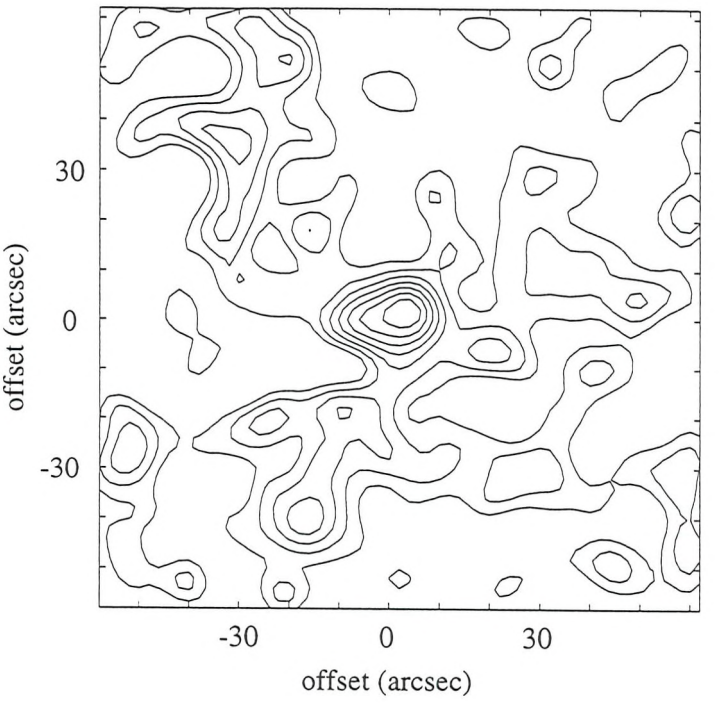

Figure 3.2: Contour plot of the combined image of all the early-type galaxies that belong to Abell 2634. The pixel size of the image is 2 arcsec and it has been smoothed with a Gaussian kernel of 2 pixels. The center of the plot coincides with the optical centres of the galaxies. The contour lines are from 20 to 100 per cent the peak value and are spaced linearly in intervals of 5 per cent.

of Abell 2634 ($N_{\rm H} = 4.94 \times 10^{20}$ cm^{-2}). These calculations predict that the 62.5 ksec HRI observation of this cluster should yield somewhere between $\sim$ 1 and $\sim$ 1200 counts from each galaxy. Motivated by this prediction of a respectable, but not huge, number of counts per galaxy, we set out to detect emission associated with cluster galaxies.

This fairly modest amount of emission from each individual galaxy is projected against the bright background of the ICM emission, which deteriorates the detectability of each galaxy. The statistics can be improved by stacking together the X-ray images in the vicinity of the 40 E and S0 galaxies marked in Fig. 3.1. Figure 3.2 presents a contour plot of the combined image, which covers a region of 1 arcmin radius around the stacked galaxies. The centre of the plot coincides with the optical centres of the individual galaxies. Clearly, there appears to be X-ray emission associated with the cluster galaxies, and it is centred at their optical positions. This coincidence provides some confidence that the X-ray and optical frames are correctly registered. A composite brightness profile for the 40 galaxies was also constructed by adding the

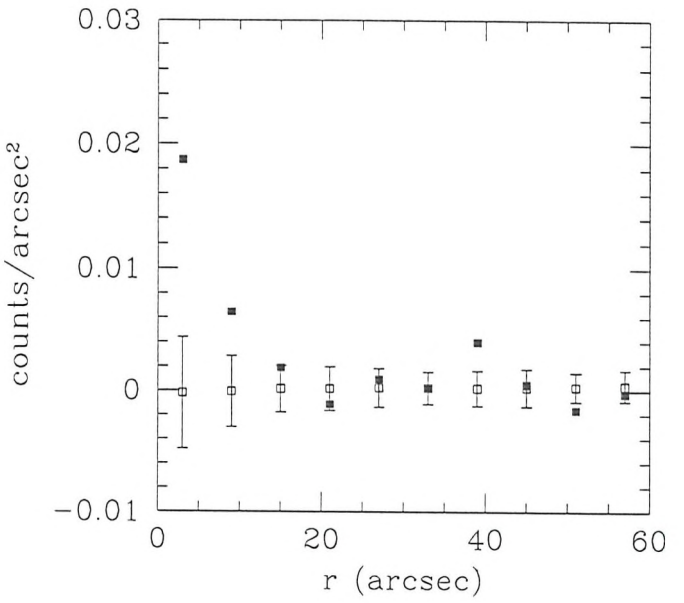

Figure 3.3: The combined surface brightness profile of all the early-type galaxies (filled squares) normalized to one galaxy. Open squares represent the average profile from the simulations.

unsmoothed counts detected in concentric annuli centred on each galaxy. The width of each annulus in this profile was set at 6 arcsec and the local background, as measured in an annulus between 1.0 and 2.0 arcmin around each galaxy, was subtracted. The resulting profile is presented in Fig. 3.3. Once again, the excess of emission in the vicinity of the cluster galaxies is apparent.

In order to assess the significance of this detection, 100 sets of simulated data from randomly selected points on the image were generated. The diffuse emission from the ICM varies systematically with radius, and so the probability that a galaxy is coincidentally aligned with a clump in the ICM emission might vary systematically with radius. Further, the sensitivity of the HRI varies with radius. Thus, the detectability of the emission from a single galaxy will vary with radius as well. The simulated data sets were therefore constructed by extracting counts from the HRI image at the same radii as the true galaxy locations, but at randomized azimuthal angles. The mean profile and the RMS fluctuations amongst the simulated data sets are shown in Fig. 3.3. As might be expected, the average number of counts in these random data sets is zero; the larger RMS error bars at small radii reflect the smaller sizes of

these annuli. A χ^2 comparison between the observed galaxy profile and the simulated profile, shows that there is less than 0.1% probability that the apparent peak in the galaxy emission is produced by chance. Thus, the detection of emission from the galaxies in Abell 2634 is statistically significant.

3.3 Origin of the X-ray emission

As mentioned in the introduction, early-type galaxies have been found to retain large amounts of hot gas, which extends far beyond the optical limits of the galaxies. X-ray binaries also contribute to the total emission, and they become more dominant in X-ray faint galaxies. Some of the emission might also originate from faint active galactic nuclei (AGNs) in the cores of these galaxies. Although none of the galaxies in the present sample has been reported as an active galaxy, there is increasing dynamical evidence that the vast majority of elliptical galaxies contain central massive black holes (van der Marel et al. 1997; Kormendy et al. 1996a, 1996b; for a review see Kormendy & Richstone 1995), and therefore low-level activity might also contribute to the total X-ray emission from these galaxies. In the next sections, the properties of the detected emission from the galaxies in Abell 2634 are investigated and used to constrain its origin.

3.3.1 The extent of the X-ray emission

One diagnostic of the origin of the X-ray emission is the measurement of its spatial extent. AGN emission should be unresolved by the HRI, while emission from X-ray binaries should be spread over a similar spatial scale as the optical emission, and halos of hot gas should be still more extended.

In order to assess the spatial extent of the X-ray emission, the PSF in this HRI observation needs to be characterized. Three of the sources listed in Table 3.1 are fitted by the model PSF of the HRI detector given by Briel et al. (1996) (see also Appendix E). Only sources 3, 4, 8 were used for the determination of the width of the Gaussian. Source 6 is very elongated and cannot be represented by a symmetrical function. The distance of each source from the centre of the HRI image was also taken into account in the modelling of the PSF, since it varies with radius (Appendix E). The results are presented in Fig. 3.4 (dashed lines). As is clear from this plot, these point sources are more extended than the model PSF. This discrepancy can be attributed to residual errors in the reconstruction of *ROSAT*'s attitude, which broaden the PSF in long integrations (Appendix E). Subsequently, the PSF that is appropriate for this

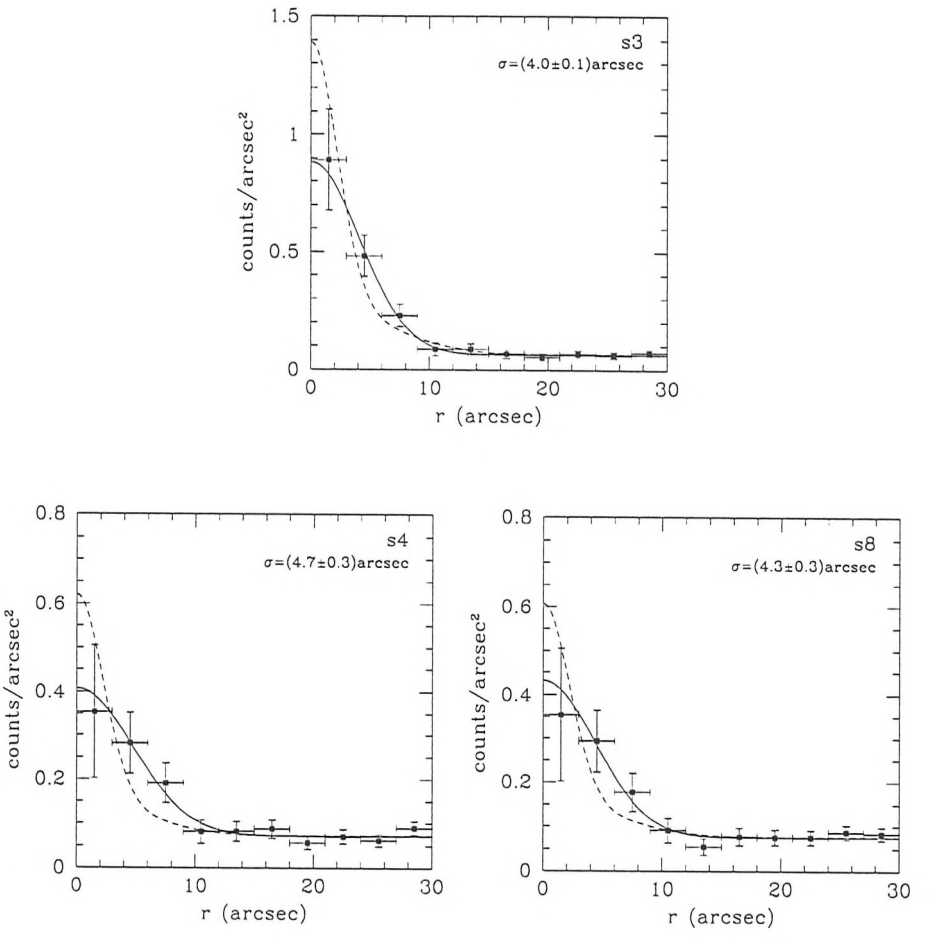

Figure 3.4: Surface brightness distribution of the bright sources in the HRI image. (s3, s4, and s8). The profiles are fitted by the appropriate HRI PSF for the distance of the point source from the centre of the image (dash line) and a Gaussian (solid line). The calculated width (σ) of the best fit Gaussian is also given.

observation was empirically determined by fitting the profiles of the point sources with a Gaussian PSF model (Fig. 3.4, solid line). The mean dispersion of the best-fit model was found to be (4.1 ± 0.1) arcsec. All of the point sources detected in this image have widths consistent with this value, and so there is no evidence that the PSF varies with radius. Therefore, this PSF is adopted for the emission from all the galaxies in the observation.

Figure 3.5 shows the comparison between the adopted PSF (dashed line) and the emission from the cluster galaxies. The emission appears to be more extended than the PSF; fitting the data to the PSF yields a χ^2 value of 14.2 with 9 degrees of freedom, which is marginally consistent with the emission being unresolved. A better

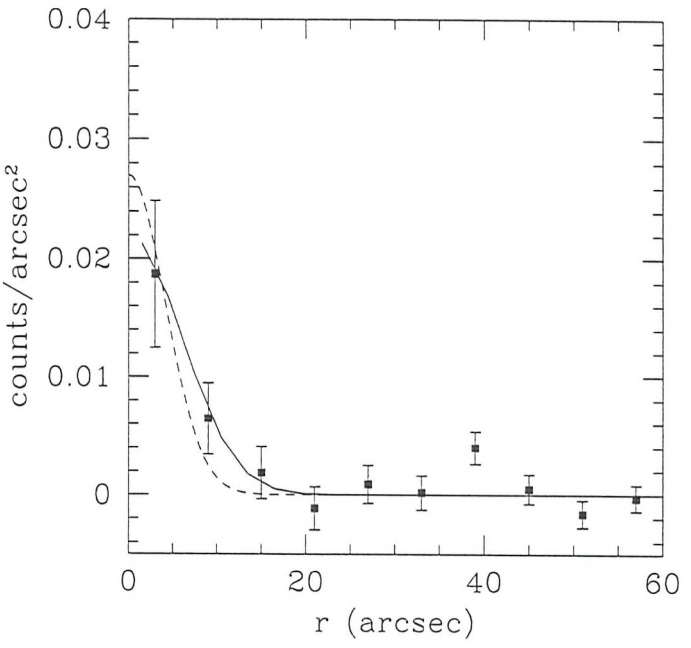

Figure 3.5: The combined surface brightness distribution of the 40 early-type galaxies, normalized to one galaxy. The profile is fitted by the measured HRI PSF (dashed line). The solid line represents the best fit spatially-extended model convolved with the PSF.

fit can be obtained by modelling the radial profile of the emission using a Gaussian, which is convolved with the PSF to model the observed profile. Fitting this model to the observations, a value of $4.3^{+2.2}_{-2.8}$ arcsec is found for the intrinsic width of the X-ray emission. The best-fit model is also shown in Fig. 3.5 (solid line).

The radii of the X-ray halos of early-type galaxies with optical luminosities comparable to those in this cluster have been shown to be $\sim$ 20 – 60 kpc (e.g. Fabbiano et al. 1992), with the lower values characterizing optically fainter galaxies. At the distance of Abell 2634 these values correspond to $\sim$ 20 – 60 arcsec, much larger than the upper limit of $\sim$ 7 arcsec that was found for the extent of the galactic X-ray emission. Thus, the X-ray emission from the cluster galaxies, although apparently extended, clearly does not originate from the large halos of hot gas found around comparable galaxies in poorer environments.

One possible explanation for the spatial extent of the emission from these galaxies is that it could arise from errors in the adopted positions for the galaxies. Such errors would broaden the distribution of X-rays when the data from different galaxies are co-added even if the individual sources are unresolved. However, the zero-point

of the X-ray reference frame is well tied-down by the detected point sources in the field. Further, the optical locations of the galaxies come from CCD photometry with positional errors of less than an arcsecond. It therefore cannot explain the ~ 4 arcsec extent of the observed X-ray emission.

Nearly half of the early-type galaxies that were used for the previous analysis have been imaged in the I-band by Scodeggio, Giovanelli & Haynes (1997). They have fitted the optical galaxy profile with a de Vaucouleur law, and found a mean value for their effective radii of $\sim$8 arcsec, with only 4 galaxies smaller than 3 arcsec and another 3 larger than 13 arcsec [Table 3.2 column (9)]. These values are directly comparable to the spatial extent of the X-ray emission derived above. Thus, it would appear that the observations are consistent with what we would expect if the X-ray emission from the galaxies in Abell 2634 originates from X-ray binaries in these systems, although the possibility that some fraction of the emission comes from AGN has not been ruled out.

3.3.2 The luminosity of the X-ray emission

A further test of the origin of the X-ray emission in the cluster galaxies comes from its luminosity. It has been found that the blue luminosities of galaxies correlate with their X-ray luminosities, with the optically brighter galaxies being more luminous in X-rays (e.g. Forman et al. 1985; Fabbiano et al. 1992). This correlation for the early-type galaxies in the Virgo cluster is presented in Fig. 3.6. The optical and X-ray luminosities of these galaxies are taken from Fabbiano et al. (1992). The line in this plot divides the $L_B - L_X$ plane into two distinct galaxy types (Fabbiano & Schweizer 1995). In addition to the differences in the ratio of X-ray-to-optical luminosities, galaxies in these two regions have been shown to possess different spectral properties. The spectra of the X-ray bright galaxies [group (I)] are well fitted by Raymond-Smith models of 1 keV temperature, and it is believed that these galaxies retain large amounts of hot ISM. In the spectra of the X-ray faint galaxies of group (II), on the other hand, a hard component is present; X-ray binaries are believed to be the major source of the X-rays in these galaxies.

In order to see where the galaxies of Abell 2634 lie in this plot, their optical and X-ray luminosities must be calculated. Butcher & Oemler (1985) measured J and F optical magnitudes for a large number of galaxies in Abell 2634. These J magnitudes were converted to the blue band by applying the colour relations provided by Oemler

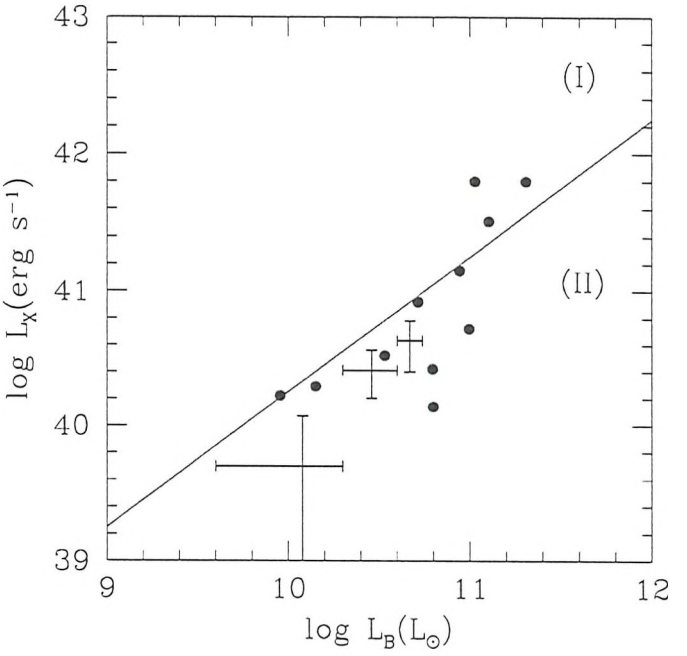

Figure 3.6: X-ray luminosity versus blue luminosity for the early-type galaxies. The line delineates the boundary between the locations of galaxies where the hot ISM makes a significant contribution to the total emission [region (I)], and the locations of galaxies where the entire emission can be ascribed to X-ray binaries [region (II)]. The locations in this plane of galaxies that belong to the Virgo cluster are marked by filled circles. The average properties of galaxies in Abell 2634 lying in different optical luminosity ranges are indicated by crosses.

(1974) and Butcher & Oemler (1985), which lead to the following equation:

$$B = J + 0.715 \tag{3.1}$$

The blue magnitudes (B) were subsequently corrected for Galactic extinction, which has a value of $A_B = -0.16$ for the direction of Abell 2634 (NED). The appropriate K-correction was also applied, using $K_B = 0.15$ for the redshift of Abell 2634 (Oke & Sandage 1968, Schild & Oke 1971). Finally, these magnitudes were converted to absolute blue magnitudes and blue luminosities. It was found that the absolute blue magnitudes of the galaxies in the HRI image lie in the range from -18.5 to -21.4. These galaxies were divided into three groups according to their optical luminosities: group A $(0.4 - 2.0) \times 10^{10}$ $L_\odot$ with 17 galaxies; group B $(2.1 - 3.7) \times 10^{10}$ $L_\odot$ with 8 galaxies; and group C $(3.8 - 5.5) \times 10^{10}$ $L_\odot$ with only 2 galaxies.

The X-ray luminosity of each group was obtained by repeating the analysis of §3.1.1 using just the galaxies in each sub-sample. Using the PIMMS software the observed count rate from the HRI image was converted to X-ray luminosity in the energy range 0.2-3.5 keV. The thermal model used for the conversion is the same as that used by Fabbiano et al. (1992) to derive the plot shown in Fig. 3.6, and is discussed in §3.1.1.

The resulting values for optical and X-ray luminosities in each sub-sample are shown in Fig. 3.6. The horizontal error bars represent the width of each optical luminosity bin and the vertical ones show the errors in the measured X-ray luminosities. This plot shows that the galaxies in Abell 2634 follow the established correlation: the optically brighter galaxies are also more luminous in the X-rays. The existence of this correlation also implies that the detected X-ray flux from the galaxies in Abell 2634 is not dominated by a few bright galaxies, but that the optically fainter galaxies also contribute to the detected X-ray emission.

The galaxies in Abell 2634 probe the fainter end of the $L_B - L_X$ relation as covered by Virgo galaxies. It should be borne in mind that there is a bias in the Virgo data which means that the two data sets in Fig. 3.6 are not strictly comparable. At the lower flux levels, a large number of Virgo galaxies have not been detected in X-rays, and so this plot preferentially picks out any X-ray-bright Virgo galaxies. For the Abell 2634 data, on the other hand, the co-addition of data from all the galaxies in a complete sample means that the data points represent a true average flux. However, it is clear that the X-ray fluxes from galaxies in these two clusters are comparable.

The similarity between the X-ray properties of galaxies in these two clusters is of particular interest because their environments differ significantly. The galaxies from the Virgo cluster shown in Fig. 3.6 lie in a region between 360 kpc and 2 Mpc from the centre of the cluster. Recent *ROSAT* PSPC observations have shown that the number density of the hot ICM of this cluster drops from 3×10^{-4} to 3×10^{-5} cm^{-3} in this region (Nulsen & Böhringer 1995). The galaxies from Abell 2634 that have gone into this plot lie in the inner 0.8 Mpc of Abell 2634, and in this region the number density of the ICM varies between 1×10^{-3} and 2×10^{-4} cm^{-3} (chapter 4). Thus, the galaxies in the current analysis come from a region in which the intracluster gas density is, on average, an order of magnitude higher than the density of the gas surrounding the Virgo cluster galaxies.

The location of the galaxies in region (II) of Fig. 3.6 adds weight to the tentative conclusion of the previous section that the X-ray emission from these galaxies can be explained by their X-ray binary populations, since any significant ISM contribution would place them in region (I). Similarly, the low X-ray fluxes of these galaxies leave

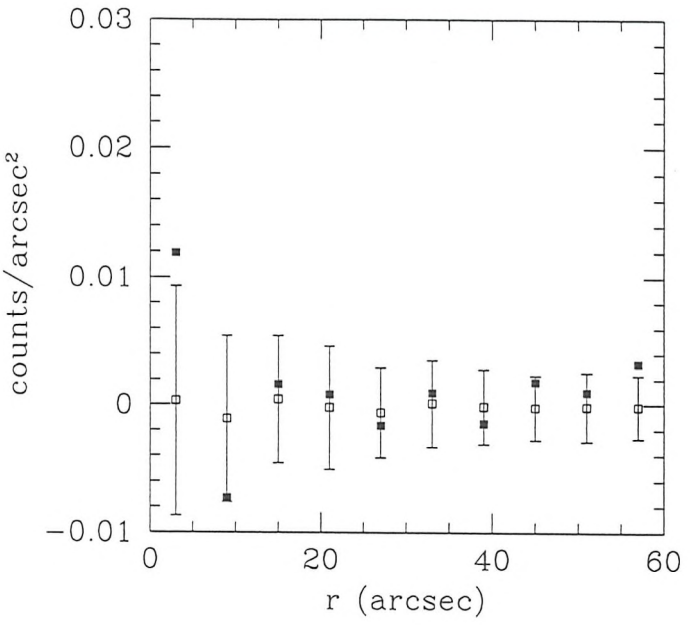

Figure 3.7: The combined surface brightness profile of the spiral galaxies that lie in the field of view of the HRI (filled squares) normalized to one galaxy. Open squares represent the average profile from the simulations.

little room for a significant contribution from weak AGN. If the X-ray binary populations are comparable to those assumed by Fabbiano & Schweizer (1995) in calculating the dividing line in Fig. 3.6, then essentially all the X-ray emission from these galaxies can be attributed to the X-ray binaries. Thus, any average AGN emission brighter than a few times 10^{40} erg s^{-1} can be excluded, as such emission would also move the galaxies into region (I) of the L_B – L_X plane.

3.4 Spiral galaxies

Having discussed the X-ray properties of the early-type galaxies in Abell 2634 at some length, we now turn briefly to the properties of the spiral galaxies in the cluster. Abell 2634 is a reasonably rich system, and therefore it is not expected that many spiral galaxies are located within it. Indeed, only 7 of the 62 galaxies whose redshifts place them at the distance of Abell 2634, and which lie within the field of the HRI, have been classified as spirals. The statistics are correspondingly poor when the X-ray emission around these galaxies is co-added: the combined profile is shown in Fig. 3.7,

together with the results from the control simulations (see §3.1.1 for details). It is clear from this figure that the spirals have not been detected in this observation, and a χ^2 fit confirms this impression.

The failure to detect these galaxies is not surprising. Not only are there relatively few of them, but their X-ray luminosities are lower than those of early-type galaxies. In the *Einstein* energy band (0.2 - 3.5 keV), their luminosities have been found to lie in the range $\sim 10^{38}$ to $\sim 10^{41}$ erg s^{-1} (Fabbiano 1989). Modelling this emission using a Raymond-Smith model with a higher temperature than for the early-type galaxies, as appropriate for spiral galaxies (Kim et al. 1992a), it is found that the expected count rate for these galaxies is a factor of ~ 40 lower than for the ellipticals in the cluster. It is therefore unsurprising that the small number of spiral galaxies present in the cluster has not given an appreciable count rate in this observation.

3.5 Summary and Discussion

X-ray emission from the normal elliptical galaxies in Abell 2634 has been detected. The limited spatial extent of this emission coupled with its low luminosity is consistent with it originating from normal X-ray binaries in the galaxies' stellar populations. These galaxies do not seem to have the extended hot ISM found around galaxies that reside in poorer cluster environments.

The simplest explanation for the absence of an extensive halo around a cluster galaxy is that it has been removed by ram pressure stripping as the galaxy travels through the ICM. A simple criterion for the efficiency of this process can be obtained by comparing the gravitational force that holds the gas within the galaxy to the force due to the ram pressure, which tries to remove it (Gunn & Gott 1972). The gravitational force is given by:

$$F_{\rm GR} \sim G \, \frac{M_{\rm gal} \, M_{\rm gas}}{R_{\rm gal}^2} \tag{3.2}$$

where $M_{\rm gal}$ is the total mass of the galaxy, $M_{\rm gas}$ is the mass of the X-ray emitting gas, and $R_{\rm gal}$ is the radius of the galaxy's X-ray halo. For typical values for the masses of the galaxy and the gas of 10^{12} $M_\odot$ (Forman et al. 1985) and 5×10^9 $M_\odot$ (e.g. Canizares et al. 1987) respectively, and a mean value for $R_{\rm gal}$ of 40 kpc (Canizares et al. 1986), which is a representative value for galaxies of the same optical luminosity as the galaxies in Abell 2634, equation (3.2) implies that $F_{\rm GR} \sim 1 \times 10^{30}$ N.

The force due to ram pressure is described by:

$$F_{\rm RP} = \rho_{\rm ICM}\ v_{\rm gal}^2\ \pi R_{\rm gal}^2 = \mu\ m_{\rm p}\ n_{\rm ICM}\ v_{\rm gal}^2\ \pi R_{\rm gal}^2 \tag{3.3}$$

where $\rho_{\rm ICM}$ is the density of the ICM, μ is the mean molecular weight, $m_{\rm p}$ is the proton mass, $n_{\rm ICM}$ is the number density of the ICM, and $v_{\rm gal}$ is the galaxy velocity. From the velocity dispersion profile of Abell 2634 presented by den Hartog & Katgert (1996) it can be found that the velocity dispersion, $\sigma_{\rm v}$, in the inner 15 arcmin radius of this system is ≈ 710 km s^{-1}. Assuming an isotropic velocity field, the characteristic three-dimensional velocity of each galaxy is hence $v_{\rm gal} = \sqrt{3}\ \sigma_{\rm v} \approx 1230$ km s^{-1}. The number density of the ICM in the same inner region has been derived from recent *ROSAT* PSPC data (Schindler & Prieto 1997) and this HRI observation (chapter 4), and is found to vary from 1×10^{-3} cm^{-3} down to 2×10^{-4} cm^{-3}, consistent with previous *Einstein* observations (Jones & Forman 1984; Eilek et al. 1984). Inserting these values into equation (3.3), the force due to ram pressure is $F_{\rm RP} \sim (1 - 10) \times 10^{30}$ N.

Thus, the ram pressure force exerted on the galaxies in Abell 2634 is found to be larger than the force of gravity, and so ram pressure stripping is possibly an effective mechanism for removing the ISM from these galaxies. In poorer environments, the density of the ICM is likely to be at least a factor of ten lower, and the velocities of galaxies will be a factor of ~ 3 smaller. In such clusters the ram pressure force ($F_{\rm RP}$) will be a factor of ~ 100 lower. Since such a change would make $F_{\rm RP} < F_{\rm GR}$, it is not surprising that galaxies in poor environments manage to retain their extensive halos.

Additional stripping of galactic gas could result from the tidal interactions between the cluster's galaxies. The mean time $t_{\rm C}$ between two successive galaxy collisions can be expressed as:

$$t_{\rm C} = (N_{\rm gal}\ \sigma_{\rm C}\ v_{\rm gal})^{-1} \tag{3.4}$$

where $N_{\rm gal}$ is the number density of the galaxies in the cluster, and $\sigma_{\rm C}$ the cross section of the process. Assuming that all 62 galaxies of Abell 2634 are located inside a sphere of radius 15 arcmin centered at the cluster centre, an upper limit can be set to the galaxy number density of 45 galaxies Mpc^{-1}. The time $t_{\rm C}$ between two very close encounters, with the impact parameter being less than $2R_{\rm gal}$, according to eq. (3.4) is $t_{\rm C} \sim 9 \times 10^8$ yr, smaller than the Hubble time (2×10^{10} yr). Therefore, it is expected that tidal interactions could have modified the appearance and properties of the galaxies in Abell 2634 over their lifetime.

The absence of extensive X-ray halos around the galaxies in Abell 2634 implies that stripping mechanisms dominate the processes of accretion and stellar mass loss

which can replenish the ISM. However, the details of all these mechanisms are not yet very well understood. For example, numerical simulations of interacting disk galaxies show that only a small amount of the gas is removed from the galaxy by tidal interactions, and a large fraction of it is driven towards the centre of the galaxy (Barnes & Hernquist 1991), possibly initiating the creation of a black hole. As mentioned in the introduction, the relative importance of each process that removes or adds gas to a galaxy depends on environmental and galactic parameters, and hence more sophisticated theoretical models are needed to find the exact rate at which gas is removed or added. By carrying out similar deep X-ray observations of clusters spanning a wide range of ICM properties, it will be possible to discover more precisely what sets of physical conditions can lead to the efficient ISM stripping that has been occured in Abell 2634.

Chapter 4

The distorted jets of 3C 465

4.1 Introduction

Abell 2634 is a nearby cluster of galaxies at a redshift of $z \sim 0.03$, classified by Abell (1958) as of richness class 1. It is located in a region in the sky of complex topology, in the background of the Pisces-Perseus supercluster (Batuski & Burns 1985; Giovanelli, Haynes & Chincarini 1986). Abell 2666, another rich cluster, is at a slightly lower redshift and 2.8 degrees east of the centre of Abell 2634.

Being nearby and in such a complex environment, Abell 2634 has been the target of many redshift measurements, and the object of studies, aimed at revealing its structure and dynamics. The first such investigation dates back to 1977, when Scott et al. obtained redshifts for 17 members of Abell 2634. By 1991, the number of galaxies with measured redshift had not increased much, and the interesting structure of Abell 2634 had to wait until 1993 to be understood.

In 1993, Pinkney at al., using the redshift of 126 galaxies with ($6000 < cz < 14000$) km s^{-1} in 2 degrees (~6.5 Mpc) around the cluster centre, found significant substructure in the distribution of the cluster's galaxies. Although the central part of the cluster appears relaxed in their data, there is statistically significant evidence that at least one group of galaxies is merging with the primary cluster from the northeast direction.

This result was subsequently confirmed by the findings of Scodeggio et al (1995), who increased the number of galaxies with measured redshift in a field around Abell 2634 by obtaining 211 new measurements. They recognised two groups of galaxies which are possibly falling into the main cluster: one at a distance of 1.1 degrees to the northeast of the cluster centre, which is the group that was previously identified by Pinkney et al. (1993); a second group is located 0.6 degrees to the southeast

of the cluster centre. Both these groups are spiral rich with 18 and 17 members respectively, and have lower velocity dispersion than the main cluster. The data also show that the early- and late-type galaxies of Abell 2634 do not behave in the same manner, but instead they have different kinematical characteristics. This result is consistent with the idea that the spiral population is currently infalling and has not suffered significant mixing with the virialized core. Pinkney et al. (1993) found that the spatial and kinematical distributions of galaxy velocities in the core, which are mainly early-type galaxies, are compatible with them being dynamically relaxed.

The complexity of the structure of Abell 2634 is compounded by the discovery of a large HI cloud by Giovanelli et al. (1995) located near the periphery of the cluster. Its size is $\sim 300 \times 200$ kpc, and it is found half a degree the southwest of the cluster centre. Additionally, the space density of galaxies in a larger area around this cloud is enhanced, with two kinematically separate groups of galaxies being well distinguishable. Both groups are spiral rich, like all the other groups identified by Scodeggio et al. (1995), and are presumably falling for the first time towards the cluster centre.

All these results generate a clear picture of the evolutionary history of Abell 2634: the main cluster captures small groups of galaxies from its surroundings, which start falling towards the core region of the cluster until they are well mixed with the old population of galaxies. This procedure of accreting new groups of galaxies presumably continues even at the present day.

In this complicated and continuously active environment, the WAT radio source 3C 465 resides. It is located inside the core region of the cluster which was found by both Pinkney et al. (1993) and Scodeggio et al. (1995) to be relaxed. Recalling the analysis of chapter 2 which revealed that WATs are heading towards the cluster centre, and combining this result with the current situation in the cluster, a possible history of the WAT can be constructed. The radio galaxy 3C 465 may once have been associated with one small group of galaxies, like the ones that are currently falling into the cluster. After being captured and accreted into the cluster, it is now crossing the core region of the main cluster, with the other galaxies of its group indistinguishable from the general population at the present day.

The host galaxy of the WAT is the big, first-ranked galaxy NGC 7720. This galaxy was classified as a cD galaxy by Matthews et al. (1964), but as a D galaxy by Dressler (1980). Another smaller galaxy, NGC 7720A, is projected about 12 arcsec from the nucleus of the cD galaxy, giving the impression that it is its companion. However, its association with NGC 7720 is questionable. Scott, Robertson & Tarenghi (1977) and

Jenner (1974) both measured a difference of 1000 km s^{-1} between the radial velocities of both galaxies, which was further confirmed by the recent measurements of Pinkney et al. (1993). Hubble Space Telescope (HST) images of the field around these two galaxies in the R band reveal no sign of interaction between the two objects, both showing well defined elliptical isophotes (Schindler & Prieto 1997).

The radio source was mapped initially by Riley & Branson (1973), later by van Breugel (1980), and by Leahy (1984) at 408 MHz and 1.4, 2.7 and 5 GHz, revealing the interesting structure of the radio jets, apparent in the more recent VLA map of Venturi et al. (1995). As seen in Fig. 4.1, two thin and very well collimated jets emanate from the opposite sides of the galaxy. Throughout this chapter this part of the jets is called the 'parsec-scale jet'. Suddenly, at a distance of ~30 arcsec ($\sim 30 h_{50}^{-1}$ kpc) from the core, the jets widen dramatically and start bending, forming the well-known shape of a WAT radio source. This fat and bent part of the jet is called the 'kiloparsec-scale jet'. The points where the transition from the parsec- to the kiloparsec-scale jet occurs are commonly referred to as 'hot-spots'.

The jet shape of 3C 465 has intrigued many researchers and led to a search for the causes of such a structure. Leahy (1984), assuming a constant jet velocity of $\sim$ 2000 km s^{-1}, attributed the overall bent shape of 3C 465 to ram pressure arising from the motion of the host galaxy through the ICM at a speed of 600 km s^{-1}. He also pointed out that such a model could not reproduce the details of the jets, such as the sudden flaring. For these reasons, he also proposed that the hot-spots may result from an instability in the jets as they enter the ICM from the protective ISM of the host galaxy, but he did not explore this hypothesis in any detail. This issue will be explained and discussed later in this chapter.

At that time, clusters of galaxies were perceived as fully-formed systems, isolated from their surroundings, which did not suffer any disturbance by infalling groups of galaxies and mergers. In such relaxed structures, the big cD galaxies would be at rest at the centre of the cluster. Therefore, the galaxy velocity which was found by Leahy (1984) to be necessary for the ram pressure model could not be reconciled with the existing picture of a cluster of galaxies. This discrepancy drove Eilek et al. (1984) to invoke more exotic forces for the bending of the jets in 3C 465, such as electromagnetic forces, which permitted a stationary galaxy. The applicability of such models was restrained by the lack of knowledge about the strength and order of magnetic fields in clusters of galaxies, and currents in the jets.

This chapter is focussed on the dynamics of the WAT radio galaxy in Abell 2634. Utilizing the *ROSAT* HRI observations presented in chapter 3, and the available PSPC

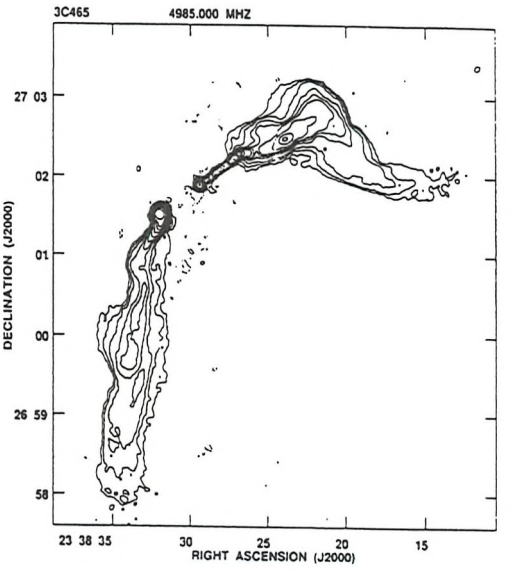

Figure 4.1: VLA radio map of 3C 465 at 5GHz taken by Venturi et al. (1995).

data retrieved from the archive, the interaction of the kiloparsec-scale jets with the surrounding ICM is studied. The detailed structure of the kiloparsec-scale jets is used to estimate the velocity of the galaxy and the velocity of the kiloparsec-scale jets (§4.3). The nature of the hot-spots and the causes for the transition from the parsec- to kiloparsec-scale jets are investigated and discussed in §4.4 and §4.5.

4.2 Properties of the ICM in Abell 2634

Early *Einstein* observations provided the basic parameters that describe the distribution of the gas in Abell 2634 (Burns et al. 1982; Jones & Forman 1984). Jones & Forman (1984) pointed out that, despite having a central dominant galaxy, the X-ray emission from Abell 2634 is not centrally peaked, but the distribution of the ICM is characterized by an uncommonly large core radius. Based on this observational fact, they concluded that Abell 2634 must be dynamically young and possibly the remnant of a merger event. More recently, Abell 2634 has been observed by the *ROSAT* PSPC, confirming the main results of the *Einstein* data (Cirimele et al. 1997; Schindler & Prieto 1997). New *ROSAT* HRI data were also presented in chapter 3, where the X-ray emission from the individual galaxies in the cluster was investigated. In this section the overall distribution of the ICM, as seen by the HRI detector, is presented and compared to the previous findings. Figure 4.2 shows the HRI image of the inner

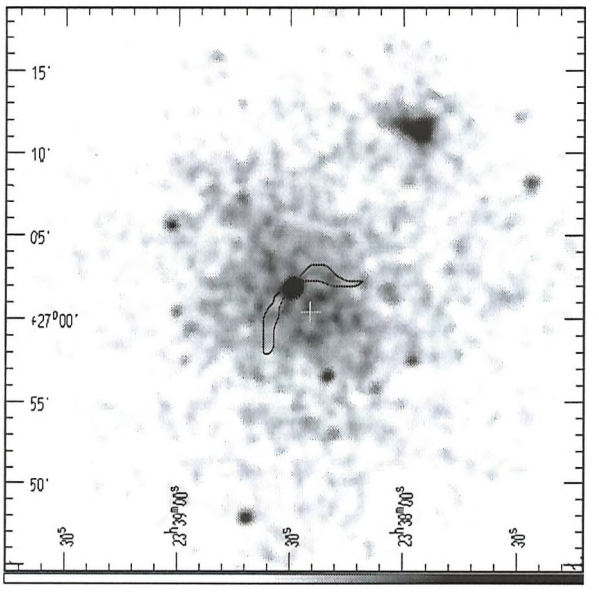

Figure 4.2: Grey-scale *ROSAT* HRI image of Abell 2634. The X-ray image pixel size is 8 arcsec; the image has been smoothed using a Gaussian kernel of σ=16 arcsec. An outline of the radio jets of the 3C 465 is also plotted. The cross marks the centre of the cluster found in chapter 2.

part of Abell 2634. This image is more heavily smoothed than the corresponding one presented in chapter 3, so that the overall structure of the ICM is more apparent. The WAT 3C 465 is associated with the bright peak at the centre of the image, and an outline of its jets is drawn against the X-ray emission.

As can be seen in Fig. 4.2 and also in the *Einstein* and *ROSAT* PSPC data, the X-ray emission from Abell 2634 is elliptical. However, in order to obtain the general characteristics of the ICM of the cluster and compare them with previous findings for cluster of galaxies, the traditional spatial analysis was performed. Such an analysis assumes that the ICM is spherically symmetric, in equilibrium within the gravitational potential of the cluster. These assumptions have been found to be very good first order approximations of the actual distribution by comparing the real X-ray images of clusters to simulated ones (Schindler 1996).

In order to obtain the light profile of the cluster, photons were counted from HRI data in circularly symmetric annuli, centered on the cluster centre, which was determined in chapter 2, and extending out to 12.5 arcmin. The width of each annulus was 25 arcsecs. The emission from the central galaxy that hosts the WAT and other bright sources projected on the HRI image (see Table 3.1 in chapter 3) were removed. The extracted surface brightness was then fitted by the traditional β-model (Appendix A).

Table 4.1: ICM distribution

	$\beta = 0.58$	$\beta = 0.65$	$\beta = 0.79$
I_0 ($\times 10^{-2}$counts arcsec^{-2})	3.4 ± 0.1	3.3 ± 0.1	3.2 ± 0.1
($\times 10^{-6}$ erg s^{-1} cm^{-2})	10.7 ± 0.3	10.4 ± 0.3	10.0 ± 0.3
r_c (arcmin)	5.6 ± 0.7	6.1 ± 0.8	7.1 ± 0.9
(h_{50}^{-1} kpc)	313 ± 39	341 ± 45	397 ± 50
n_0 ($\times 10^{-3}$ cm^{-3})	1.14 ± 0.08	1.12 ± 0.08	1.10 ± 0.07
χ^2	22.36	23.11	24.36

Since the HRI detector covers only the inner emission from the hot ICM, a background was not subtracted, but its constant surface brightness was left as a free parameter to be determined by the fit.

Leaving all four parameters free, [the central surface brightness (I_0), the core radius (r_c), the β factor, and the surface brightness of the background (I_{back})], the fits led to unrealistic small values for the β index and the core radius. The value of β is mainly constrained by the decline in the X-ray surface brightness at large radii. Since the X-ray emission from the cluster is truncated at large radii by the small field of view of the HRI detector, the poor determination of β is unsurprising. Consequently, the β index was fixed to the values calculated by Cirimele et al. (1997) ($\beta = 0.58$), and by Schindler & Prieto (1997) ($\beta = 0.79$). These values were obtained by fitting the cluster's surface brightness profile observed by the PSPC detector. Since the field of view of the PSPC is larger than the field of view of the HRI, it was possible to extract photons from a larger region around the cluster centre, and also to obtain an average value for the background emission, which was subtracted from the cluster's emission. The present HRI data were also fitted by the β-model with β=0.65, which is the average value for this index found by Jones & Forman (1984). The results of all these different fitting procedures are presented in Table 4.1. The 1σ errors for the calculated parameters are also given, and the χ^2 reported is for 27 degrees of freedom. As can be seen from this table, a slightly better fit to the HRI data is provided by the model with small β, which additionally requires smaller core radii. Figure 4.3 presents the observed surface brightness profile of the ICM along with the two best fit models with fixed β to 0.58 and 0.79. As can be seen from this figure, the two models are almost indistinguishable.

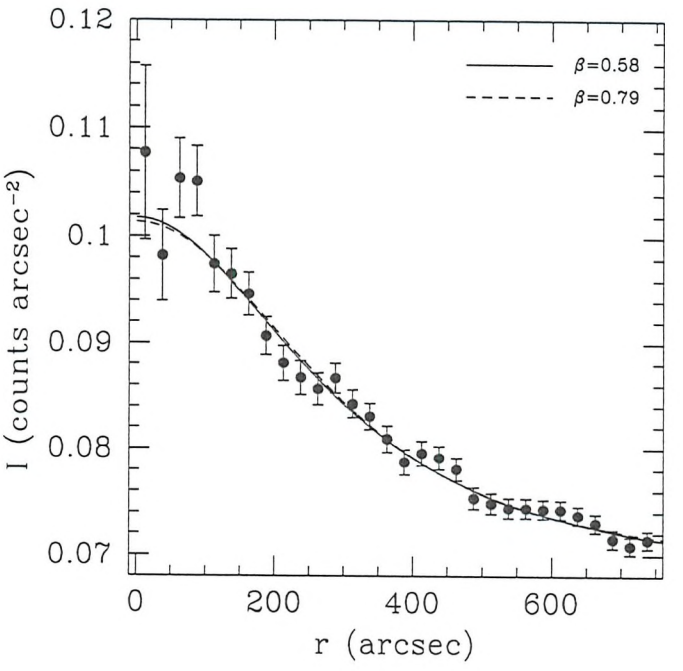

Figure 4.3: The surface brightness distribution of the ICM calculated from the HRI data. The solid line is the best fit King model for the β value fixed to 0.58, and the dashed line for β=0.79.

The deprojection of the surface brightness distribution provides the density distribution of the ICM and the value of the central number density (n_0) of the ICM. The method which is followed to derive the densities presented in Table 4.1 is described in Appendix A. The conversion of the central surface brightness from counts arcsec^{-2} to erg s^{-1} cm^{-2} and the calculation of n_0 [eq. (A.16)] require the temperature of the ICM. Both the *Einstein* and PSPC data agree on a temperature of $kT = 3.5^{+2.0}_{-1.0}$ keV, which is the value that is adopted throughout this chapter. The PIMMS software was used to convert I_0 (Table 4.1) from count rate to luminosity in the *ROSAT* energy band. The spectral model used for the conversion was a Raymond-Smith model with 25% solar abundance. As can be seen from Table 4.1, the central number densities calculated for different β values are the same within the errors. The value of $\beta = 0.58$ and the corresponding values for I_0 and n_0 are adopted for all the following calculations.

4.3 Bending of the jets

From the study of WATs in Abell clusters presented in chapter 2, it was inferred that the big galaxies which host these radio sources are not at rest at the minimum of the gravitational potential of their associated clusters. Furthermore, it was found that they move on approximately radial orbits, heading towards or away from the cluster centre. This result strongly suggests that the mechanism responsible for the large-scale bending of the jets is the ram pressure resulting from the motion of the galaxy through the ICM.

The amplitude of the force that acts on a unit volume of the jet and is due to the ram pressure ($P_{\rm rp}$) is given by

$$\boldsymbol{F}_{\rm rp} = \nabla P_{\rm rp} \;=\; \rho_{\rm gas}\,\frac{v_{\rm gal}^2}{h}\,\hat{\boldsymbol{v}}_{\rm gal}, \tag{4.1}$$

where $\rho_{\rm gas}$ is the density of the ICM, $v_{\rm gal}$ is the galaxy velocity, $\hat{\boldsymbol{v}}_{\rm gal}$ is the unit vector in the direction of the galaxy motion, and h is the scale height of the jet (O'Donoghue, Eilek & Owen 1993).

Additionally, since the jets are inside the potential of the cluster, it is expected that gravitational forces also contribute to shaping them. If they are less dense than their surroundings, buoyancy drags them towards regions in the ICM where the densities of the ICM and the material inside the jet are equal. The buoyancy force ($\boldsymbol{F}_{\rm B}$) that acts on a unit volume of the jet is described by

$$\boldsymbol{F}_{\rm B} = -(\rho_{\rm gas} - \rho_{\rm j})\;\boldsymbol{g}, \tag{4.2}$$

where $\rho_{\rm j}$ is the density of the jet. The gravitational acceleration of the cluster ($\boldsymbol{g}$) can be calculated from the properties of the ICM [see Appendix A, eq. (A.4)].

Thus, the usual Euler equation (B.3), which describes the flow of the material inside the jet, can be written

$$\frac{\partial \boldsymbol{v}_{\rm j}}{\partial t} \;+\; (\boldsymbol{v}_{\rm j}\cdot\nabla)\boldsymbol{v}_{\rm j} \;=\; \frac{1}{\rho_j}\;[\;\nabla P_{\rm rp} \;-\; (\rho_{\rm gas} - \rho_{\rm j})\;\boldsymbol{g}\;] \tag{4.3}$$

where $\boldsymbol{v}_{\rm j}$ is the velocity of the jet.

By resolving eq. (4.3) into intrinsic coordinates (see Appendix B), one finds that its perpendicular component at any point along the jet can be written

$$\rho_{\rm j}\frac{v_{\rm j}^2}{R} \;=\; \rho_{\rm gas}\frac{v_{\rm gal}^2}{h}\;\hat{\boldsymbol{v}}_{\rm gal}\cdot\hat{\boldsymbol{n}} \;+\; \frac{(\rho_{\rm gas} - \rho_{\rm j})}{\rho_{\rm gas}}\;\frac{kT_{\rm gas}}{\mu m_p}\;\nabla\rho_{\rm gas}\cdot\hat{\boldsymbol{n}} \tag{4.4}$$

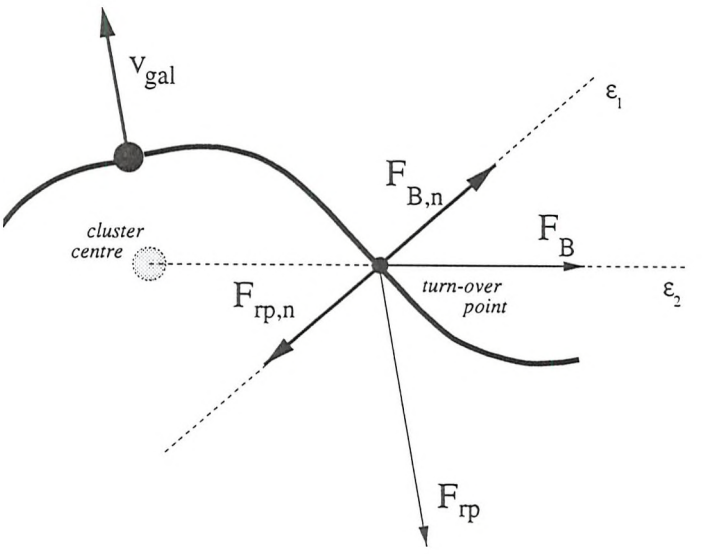

Figure 4.4: Schematic diagram of the bent jets in 3C 465. The turn-over point, which is the point in the jets where the curvature of the jets changes bending direction, is shown. The line ε_1 is normal to the jet (parallel to $\hat{\boldsymbol{n}}$), while ε_2 is the line that connects the cluster centre and the turn-over point. At this point the components of the ram pressure ($F_{\rm rp}$) and buoyancy ($F_{\rm B}$) parallel to ϵ_1 exactly balance.

where $\hat{\boldsymbol{n}}$ is the unit vector normal to the jet, and R is the radius of curvature of the jet at that point. In the last equation, the gravitational acceleration $\boldsymbol{g}$ has been substituted by eq. (A.4). Using the density distribution of the ICM [eq. (A.9)] to find the analytical form of $\nabla\rho_{\rm gas}$, and setting $\xi = \rho_{\rm j}/\rho_{\rm gas}$, eq. (4.4) takes the form:

$$\frac{v_{\rm j}^2}{R} = \frac{1}{\xi}\frac{v_{\rm gal}^2}{h}\,\hat{\boldsymbol{v}}_{\rm gal}\cdot\hat{\boldsymbol{n}} - \frac{3\beta kT_{\rm gas}}{\mu m_p r_{\rm c}}\,\frac{\frac{r}{r_{\rm c}}}{1+\left(\frac{r}{r_{\rm c}}\right)^2}\left(\frac{1}{\xi}-1\right)\,\hat{\boldsymbol{r}}\cdot\hat{\boldsymbol{n}} \qquad (4.5)$$

where $\hat{\boldsymbol{r}}$ is the unit vector along the direction of $\hat{\boldsymbol{g}}$. In this equation r is the distance of the point of interest from the cluster centre, $\hat{\boldsymbol{v}}_{\rm gal}\cdot\hat{\boldsymbol{n}}$ is the cosine of the angle between the two unit vectors $\hat{\boldsymbol{v}}_{\rm gal}$ and $\hat{\boldsymbol{n}}$, and $\hat{\boldsymbol{r}}\cdot\hat{\boldsymbol{n}}$ the cosine of the angle between $\hat{\boldsymbol{r}}$ and $\hat{\boldsymbol{n}}$. These last three parameters can all be measured from radio maps of the WAT source.

The two crucial unknowns in this equation are the jet and galaxy velocities, and eq. (4.5) cannot be used to give independent measurements of these two quantities unless an 'average' or 'representative' value is assumed for one of them. Thus, if one wants to calculate the galaxy velocity using eq. (4.5) it is necessary to make the difficult choice of an appropriate average value for the jet velocity. The literature is flooded with values for the jet velocities, which have been found by utilizing different

techniques such as detection of proper motion (Zensus 1991; Biretta, Zhou & Owen 1995), relativistic beaming (e.g., Biretta 1992), conversion of the radio luminosity to kinetic energy of the jets (e.g., O'Dea 1985; O'Donoghue et al. 1993), and the interaction of the jets with their surroundings (Bridle & Perley 1984; Kellermann & Owen 1988). The jet velocities cited span from a few hundred km s^{-1} to significant fractions of the speed of light, showing that an average value for the jet velocity has not yet been established.

However, as has been shown by Sakelliou et al. (1996), a special characteristic of the bent jets provides the means to overcome this problem of having two unknowns, and calculate the galaxy velocity independent from the jet velocity. As in 4C 34.16 (Sakelliou et al. 1996), the radio map of 3C 465 (Fig. 4.1) shows clearly that the radio jet exhibits a double bend. Near the hot-spot, the jet is bent towards the cluster centre but further downstream it changes direction, travelling away from the cluster centre. The first bend can be attributed to ram pressure resulting from the relative motion of the galaxy through the ICM. At larger radii, buoyancy takes over as the dominant force, and the jet changes direction towards lower density regions in the ICM.

The interplay between these two forces provides a useful constraint on the velocity of the galaxy and the properties of the jets. At the point at which the bend in the jets changes direction (the 'turn-over' point), the radius of curvature becomes infinite, and the left hand of eq. (4.5) is equal to zero. Therefore, at the turn-over point the components of ram pressure and buoyancy in the direction normal to the jet exactly balance (Fig. 4.4), providing an equation in which the only unknown is the velocity of the galaxy:

$$v_{\rm gal}^2 = \frac{3\beta k T_{\rm gas} h}{\mu m_p r_{\rm c}} \frac{\frac{r_{\rm to}}{r_{\rm c}}}{1+\left(\frac{r_{\rm to}}{r_{\rm c}}\right)^2} \frac{\hat{\boldsymbol{r}}\cdot\hat{\boldsymbol{n}}}{\hat{\boldsymbol{v}}_{\rm gal}\cdot\hat{\boldsymbol{n}}}\,(1-\xi) \qquad (4.6)$$

In this equation there is no dependence on the velocity of the jet, and $v_{\rm gal}$ can be calculated as a function of $\rho_{\rm j}$. The scale height h, is the width of the jet at the turn-over point. It can be measured from the width of the radio emission, suitably corrected for the resolution of the telescope, using $h = \sqrt{h_{\rm m}^2 - d^2}$, where $h_{\rm m}$ and d are the measured width and the resolution of the radio map. The quantity $r_{\rm to}$ is the distance of the turn-over point from the cluster centre.

Equations (4.5) and (4.6) are valid for any position of the jets relative to the cluster centre, and for their derivation knowledge of the 3-dimensional geometry was not required. But now, if the requisite distances and angles are to be measured, it must be understood how the real geometry corresponds to that apparent in the radio images, and how projection effects influence these measurements.

One basic assumption required to simplify the calculations is that the cluster centre lies on the plane defined by the bent radio jets. If so, the galaxy velocity vector will also be on this plane. Such an assumption is justified by the result of chapter 2 that the galaxies that host WATs are mainly heading directly towards or away from the cluster centre. Additionally, such an assumption places all the forces and vectors involved in equations (4.5) and (4.6) on the same plane.

However, there is some evidence that this plane does not coincide with the plane of the sky. Venturi et al. (1995) have recently presented and analysed VLBI observations of 3C 465. These observations, as in the VLA map of Fig. 4.1, the parsec-scale radio jets appear asymmetric: the northern one is brighter than the jet emerging from the opposite side of the galaxy. Such an asymmetry has been seen in other radio galaxies, and is normally interpreted as the result of Doppler favoritism. If two intrinsically symmetric relativistic jets do not lie on the plane of the sky, the one that points towards us appears brighter than the counterjet, due to relativistic effects. The observed ratio R of the radio brightness of the jet divided by the radio brightness of the counter-jet depends on both the velocity of the jet, and the angle θ between the plane on which the radio source lies with the line of sight:

$$\beta \cos\theta = \frac{R^s - 1}{R^s + 1} \tag{4.7}$$

where $\beta = v_j/c$. The parameter s is defined as $s = 1/(2+\alpha)$, where α is the spectral index of the radio emission (Blandford 1990).

Since the counter-jet in the case of 3C 465 is not visible, Venturi et al. (1995) assigned a limit of $R > 30$. Using a spectral index of $\alpha = 0.5$, they derived that $\beta \cos\theta \gtrsim 0.59$. It is clear that eq. (4.7) on its own cannot constrain both the velocity of the jet and the angle θ. A second independent constraint used by Venturi et al. (1995) and also by Giovannini et al. (1994), is the ratio of the core flux at 5 GHz to the core power at 408 MHz, which also depends on the Doppler boosting. Using both constraints, they found that $\theta \lesssim 54$ degrees, and the velocity of the parsec-scale jet is $v_j \gtrsim 0.6c$. Thus, the plane mentioned earlier, on which the jets of 3C 465 lie, does not coincide with the plane of the sky, but it is at an angle $\theta \lesssim 54$ degrees with the line of sight.

Whatever the real orientation in space of the plane that contains the radio jets, its actual position can be found by rotating twice its projected image on the sky: one rotation around the line parallel to the projection of the galaxy velocity on the sky by the appropriate angle θ, implied by the results of Venturi et al. (1995); and a

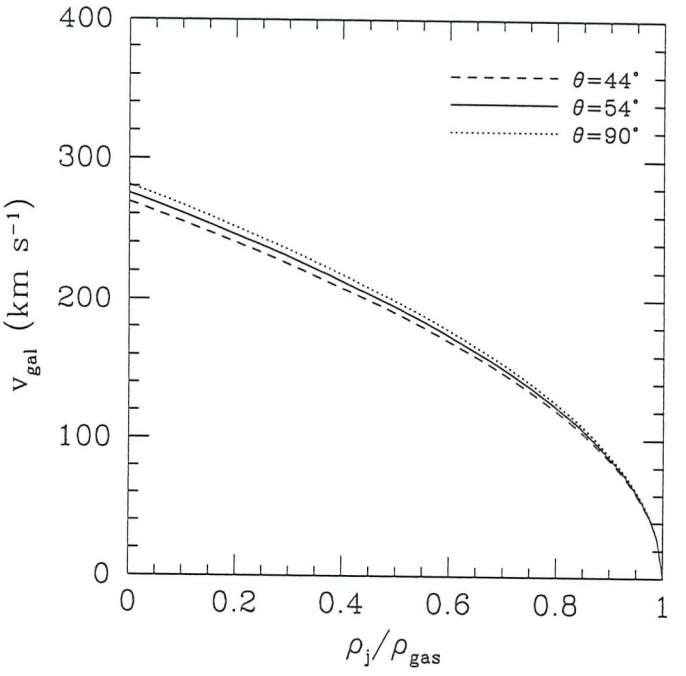

Figure 4.5: The derived galaxy velocity as a function of the density of the jet. The calculations are done taking into account the inclination of the source with respect to the plan of the sky. The angle $\theta = 54°$ is the upper limit set by Venturi et al. (1995) for the angle between the jets and the line of sight.

second rotation around a perpendicular line. By correcting eq. (4.6) for the projection effects introduced by the first rotation, the real component of the galaxy velocity on the plane of the sky can be found. A correction for the second rotation would provide the amplitude of the galaxy velocity in space. However, such a calculation is not required since a measure of the galaxy velocity along the line-of-sight already exists from optical observations (Pinkney et al. 1993; Scodeggio et al. 1995).

The way that the distance r_{to} and the angles of interest were transformed is presented in Appendix C. Using the transformed values for these quantities, eq. (4.6) was solved to give the component of the galaxy velocity on the plane of the sky. The result, for different angles θ is presented in Fig. 4.5. Interestingly, there is an upper limit on the galaxy velocity of 3C 465 relative to the ambient gas of $v_{gal} \leq 280$ km s^{-1}, and surprisingly this result is almost unaffected by projection effects.

As mentioned earlier, the line-of-sight component of the galaxy velocity has been measured by Pinkney et al. (1993) and Scodeggio et al. (1995). They both agree with a value of 85 ± 95 km s^{-1}, which combined with the previous result of the perpendicular

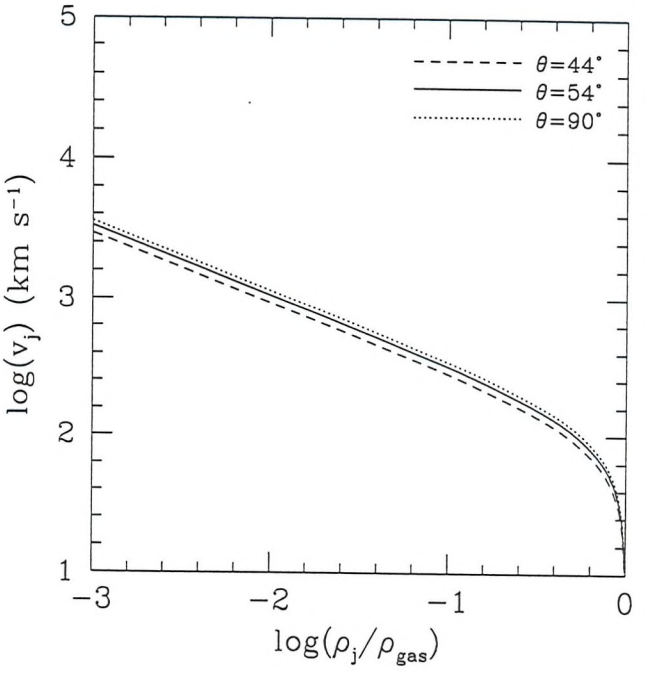

Figure 4.6: The derived jet velocity as a function of the density of the jet. The results for different inclination angles is shown.

component, implies that the total galaxy velocity is less than 293 km s^{-1}.

Combining equations (4.5) and (4.6), and correcting for projection effects as before, the jet velocity for a point near to the hot-spots can be found. The result is given in Fig. 4.6, again for a set of different inclination angles θ. According to this figure, if the kiloparsec-scale jets are a hundred of times less dense than the surrounding ICM their velocity can reach a value of $\sim$ 1000 km s^{-1}. Even for very rarefied jets ($\rho_j/\rho_{gas} = 10^{-3}$), v_j cannot be greater than 3200 km s^{-1}.

The previous result reveals a large difference between the measured values of the parsec- and kiloparsec-scale jet velocities. As has already been mentioned, the parsec-scale jets of this radio galaxy have been found to be relativistic. Venturi et al. (1995) set a lower limit for the jet velocity of 0.6c. In contrast to this relativistic velocity, the above analysis points towards much slower kiloparsec-scale jets. In the next sections the reasons for this difference are discussed, and possible links between the relativistic, parsec-scale and subrelativistic, kiloparsec-scale radio jets are investigated.

4.4 From relativistic to subrelativistic jets

A property characteristic of many radio galaxies is a pronounced and abrupt flaring of their radio jets; as Fig. 4.1 illustrates, the initially-narrow jets become suddenly wider and are transformed into large radio lobes. In almost all the cases, this dramatic transition occurs in both jets at approximately the same distance from the core of the radio emission. High resolution radio maps of WATs (O'Donoghue et al. 1990) show this sudden transformation happening symmetrically in both jets at a distance of (10-100) kpc from the radio core, where they widen by a factor of 3-10 (O'Donoghue at al. 1993).

Several possible scenarios have been proposed to explain this jet/lobe transition. The first one proposes that a jet may disrupt as a result of the growth of an instability, in which it becomes turbulent, loses its coherence, and turns into a less-collimated lobe structure. It has been believed for some time that instabilities and turbulence play an important role in the morphological appearance and characteristics of radio jets (Birkinshaw 1991). The notion that the hot-spots indicate the position where a laminar flow becomes turbulent was supported by the correlation found by Birkinshaw et al. (1978) between the radio power of the core and the length of the parsec-scale radio jet. They found that the more powerful the core is, the greater the length of the relativistic jet. This correlation could be explained if powerful cores produce more energetic and strong jets. A powerful jet can travel undisrupted from instabilities to greater distances away from the galaxy before it becomes turbulent, and loses its well collimated structure. Recent numerical simulations of jet flows seem to reproduce the observed morphology, with the sudden flaring from jet to lobe occurring at the transition from laminar to turbulent flow (Loken et al. 1995). However, the results of these studies are still fairly preliminary, and rely on physically-unmotivated devices such as imposed perturbations on the initial jet. Therefore, it is not clear yet what could induce the instabilities in the jets.

When a jet becomes turbulent, it can more easily entrain matter from its surroundings. The collision of the jets' particles with the nearly stationary particles of the entrained matter result to the deceleration of the jet from relativistic to subrelativistic velocities (Bicknell 1994; 1995), and thus explaining the difference in the velocities between the parsec- and kiloparsec-scale jets found in many radio galaxies, including 3C 465.

A second plausible explanation is that the sudden flaring occurs as the jet passes through the interface between the ISM of the galaxy in which it originated and the ICM of any surrounding cluster of galaxies. This scenario has been analytically inves-

tigated by Gopal-Krisna & Wiita (1987), and also by several groups using numerical simulations. Although such simulations have successfully modelled the sudden flaring of radio jets, and have demonstrated the significant change of the nature of the jet flow immediately after the interface, some of the adopted model parameters cannot be applicable for all radio galaxies. Loken et al. (1995), for instance, assumed that the density of the medium drops by an order of magnitude at the ISM/ICM boundary, accompanied by a similar increase in the temperature (so that the two media are in pressure balance). A more realistic model of the galactic atmosphere and the surrounding ICM was adopted by Hooda & Wiita (1996). They allowed the density of the ISM to decrease with the distance from the centre of the galaxy, and the density at the interface dropped by a factor of 5. The main result of all these numerical studies is that indeed, the jet becomes turbulent immediately after crossing the interface. These simulations have not advanced enough to predict the terminal jet velocity, but a deceleration of the jet is expected again due to entrainment of external matter after it becomes turbulent.

A third possible scenario is that the jet crosses a shock wave (Norman, Burns & Sulkanen 1988; Loken et al. 1995). Numerical studies of such a process predict again that the jet widens abruptly after crossing the shock, and decelerates from relativistic to subrelativistic velocities. Shock waves can exist in the ICM of a cluster of galaxies. For example, when two clusters merge violently, the two ICMs collide forming shocks (Schindler & Müller 1993). However, these shocks are oriented at random angles, and are located at various positions within the cluster, making difficult to explain the symmetrical position of the hot-spots in the radio galaxies. Alternatively, the necessary shock for this model might be a bow shock: if the radio galaxy is moving through the ICM at a speed greater than the local speed of sound a bow shock is expected to be formed in front of it (Balsara, Livio & O'Dea 1994). The disadvantage of this explanation is that it is only applicable to radio galaxies which are moving relative to the ICM.

As is clear from the above discussion, there are a number of competing possible scenarios for the mechanisms that can produce the sudden flaring of the jets. Although these explanations were originally advanced some time ago (e.g. Burns & Gregory 1982), it has not been possible to decide which one depicts the real physical process that takes place in these radio galaxies.

4.5 Testing one hypothesis: the ISM/ICM interface

X-ray data of radio galaxies and their surroundings can be used to test one of the above hypotheses. In chapter 3 it was discussed that the ISM of a normal (non-active) elliptical galaxy is in a hot phase, emitting in the X-ray (X-ray haloes). The jets of a radio galaxy originate from a host galaxy which shares similar characteristics with non-active ellipticals. For this reason, it is expected that part of the galaxy's X-ray emission comes from its X-ray halo.

However, in radio galaxies, as in other active galaxies, another component is also expected to contribute to the total X-ray emission from the host galaxy. It is well known that active galaxies are the brightest sources in the X-ray sky, and this large amount of emission is linked with the properties of the central engine. It is widely believed that black holes reside at the centres of active galaxies, giving rise to the production of the energetic jets in radio galaxies. The component of the X-ray emission that comes from the core region of the active galaxy mainly represents the gravitational energy released as material is accreted onto the black hole. The jet itself can also contribute to the X-ray emission, as has been found for the jets in M87 (Neumann et al. 1997).

The spectrum of this emission is non-thermal (compared to the thermal origin of the X-ray emission from the ISM) and it is not expected to be extended in X-ray images of these galaxies, since it comes from a region in the galaxy smaller than the resolution of any X-ray detectors. This spectrum is normally fitted by a power law model with $F(E) \sim \nu^{-\Gamma}$ (in photons cm^{-2} s^{-1} keV^{-1}). The photon index Γ varies according to the type of active galaxy. Brinkmann & Siebert (1994) cross-correlated the *ROSAT* All Sky Survey with the existing radio surveys, and performed the spectral analysis on the X-ray emission from the bright sources. Their analysis yielded that the spectra of radio galaxies are well fitted by a power law model with a photon index of $< \Gamma >= 1.96 \pm 0.60$. This value for Γ is also in good agreement with the measurements from a much larger radio/X-ray sample compiled from the *ROSAT*-Conden/Molongo correlations (see Brinkmann, Siebert & Boller 1994). Prieto (1996) also agreed on a photon index of $\Gamma \sim 2$ for the sources he found, after cross-correlating the RASS with the 3CRR sample of radio galaxies and quasars.

Some of the X-ray emission also originates from the stellar population of the galaxy, due to X-ray binaries. This emission is expected to be extended, following the distribution of the optical light profile. The spectrum of this component of the X-ray

emission is better fitted by a Raymond-Smith thermal model of ~ 5 keV temperature (Kim et al. 1992b).

The mechanism that produces the non-thermal X-rays is very efficient, yielding a luminosity in FRI radio galaxies, in the energy range from 0.1 to 2.4 keV, of $(10^{41} - 10^{45})$ erg s^{-1} (Siebert et al. 1996). X-ray haloes are on average weaker X-ray emitters, having luminosities in the (0.2-3.5) keV energy band of $(10^{39} - 10^{42})$ erg s^{-1} (Kim et al 1992a, b). Given this difference in the X-ray power of the two components, it can be seen that it is difficult to detect the underlying component coming from the X-ray halo, and separate it from the strong emission from the active nucleus.

Previous studies yielded conflicting answers to the question of the origin of the X-ray emission from radio galaxies. In an X-ray study of 40 3CR radio galaxies, Fabbiano et al. (1984) found that the X-rays are correlated with the radio power at 5 GHz, and they concluded that it is nuclear emission. Using a smaller but similar sample, Feigelson & Berg (1983) found that the emission is thermal. Rhee, Burns & Kowalski (1994) studied the X-ray emission from the radio galaxies in the Perseus cluster. They found that the spectrum of the head-tailed radio galaxy IC 310 is represented by a power law model, while the spectrum of another head-tailed source (NGC 1265) is thermal, although its spectrum can be fitted by a very steep power law. The *ROSAT* satellite has recently succeded in revealing the presence of two components. Using PSPC data, Worrall et al. (1994) proved the existence of an unresolved and an extended, thermal component, in the images and spectra of the radio galaxies they studied.

The aim of the following sections is to uncover the properties of the ISM of the galaxy that hosts 3C 465. Then, the surface brightness profile of the X-ray halo will provide its density distribution. Since the properties of the surrounding ICM are already known, the position of the ISM/ICM interface can be found as the position where the two media are in pressure balance. The density drop that the jet feels as it crosses the interface can also be calculated.

4.5.1 Spatial analysis

The PSPC image of 3C 465 presented by Schindler & Prieto (1997) provides a first indication that the emission from the galaxy may be extended. Although throughout their paper it is stated that the emission from the cD galaxy is not resolved, the comparison of the PSPC PSF with the central emission (see Fig. 4 of their paper) gives the impression that, after removing the emission due to the ICM, the unbroadened PSF would not give an acceptable fit to the remaining profile. The HRI detector,

with its better spatial resolution, provides the means to clarify this issue, and test the possibility that there is an extended component associated with NGC 7720. In this section the galaxy profile detected by the HRI detector is compared to the appropriate PSF for this particular set of observations. This PSF was calculated in chapter 3 by fitting the profile of point sources detected on the HRI image, and a Gaussian function with σ of (4.1 ± 0.1) arcsec was found to be a good representation of it.

The X-ray emission from the host galaxy appears circularly symmetric in the HRI image. The peak of the emission, which was used to define its centre ($\alpha = 23^h\ 38^m\ 29.4^s$, $\delta = 27^\circ\ 01'\ 53''$, J2000) coincides with the location of the radio core (Venturi et al. 1995). In order to obtain the surface brightness profile, photons were counted in 25 concentric circular annuli around the galaxy centre. The width of each annulus was 2 arcsec. Figure 4.7 illustrates the radial profile of the light distribution out to 50 arcsec from the galaxy centre. No background was subtracted in order to better define the size of the galaxy emission. First, the derived galaxy profile was fitted by the HRI PSF. A χ^2 test gives a probability of 20-30% (χ^2=28.3 for 24 degrees of freedom) that the representation of the galaxy profile by the PSF is good. As is seen in Fig. 4.7, the observed profile appears more extended between 10 and 30 arcsec. One concern is that this excess of emission might be due to the wings of the HRI PSF, which were not incorporated in the modelling. However, if this is the case then the total number of photons detected between 10 and 30 arcsec in this observation would comprise ~30% of the PSF. This amount is much larger than what is expected to come from the wings of the on-axis PSF (NGC 7720 lies at the centre of the HRI image).

Subsequently, the galaxy's light profile was modelled by a composite model consisting of two components. One component describes the distribution of the X-ray emitting gas, which sits in the gravitational potential of the galaxy. This distribution is well described by the β-model (see Appendix A), which has already been used to fit the surface brightness profile of the ICM in a cluster of galaxies. The second one is an unresolved component, appropriate for the X-ray emission from the nuclear region. The construction of the combined model, and the final fitting procedure to the data were performed as follows.

A series of synthetic images, which show how the hot ISM would have been registered by the HRI detector, if NGC 7720 was a non-active elliptical galaxy, were constructed. For each image this X-ray emission was represented by a β-model. The core radius increased from a minimum value for the first image to a maximum value for the last one by a constant step. The β index was held fixed to the value of 0.65

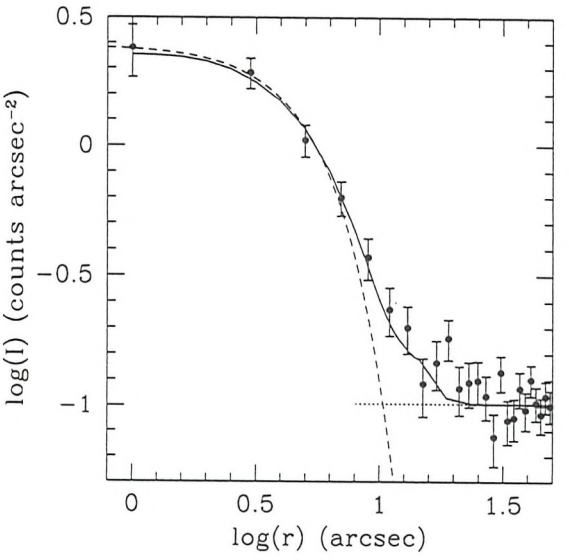

Figure 4.7: The surface brightness distribution of NGC 7720. The profile is fitted by the HRI PSF (dashed line), and a composite model that consists of an unresolved and an extended component (solid line). The horizontal dotted line shows the level of the emission due to the surrounding ICM.

for all these images, which is a value that represents well the slope of the X-ray emission in elliptical galaxies (Trinchieri et al. 1997). All these synthetic images were subsequently 'smoothed' with a Gaussian kernel of width σ=4.1 arcsec, in order to take into account the smearing due to the PSF of the HRI detector. They were also normalized so that the total number of photons registered on the HRI detector was equal to one. A similarly-normalized image of the HRI PSF was then added. The peak of the emission from the PSF was placed such that it coincides with the peak of the β-model. The radial profile of each final synthetic image was obtained in the same manner as for the real data. A constant value for the background emission due to the cluster's ICM, equal to the previously-obtained value for the central surface brightness I_0, was added to the synthetic data. Each model profile was then fitted to the real data. The normalizations of the PSF-convolved β-model (N_β) and the PSF ($N_{\rm PSF}$) were left as free parameters, to be determined by the best fit model. The fit of each model for a given core radius yielded the values for the minimum χ^2, and the best fit values for the normalizations N_β and $N_{\rm PSF}$. Repeating this fitting procedure for all the model images with different core radii, the core radius that gives the minimum χ^2 was determined. A minimum χ^2 of 18.4 (for 18 d.o.f) was obtained for a core radius of $14.5^{+10.5}_{-12}$ arcsec. The derived best fit values for the normalizations are:

$N_{\rm psf} = 223^{+2}_{-81}$ counts, and $N_\beta = 122^{+64}_{-21}$ counts. Given the way that the two models were initially normalized, these numbers correspond directly to the total number of photons detected from each component. The errors given for all three calculated quantities are their 1σ limits. The best fit model is also shown in Fig. 4.7.

Therefore, although the inner X-ray emission from NGC 7720 is mainly due to the unresolved component, an extended component also appears to be present. The light distribution of this component is satisfactorily described by a β-model with $\beta = 0.65$, and $r_{\rm c} = 14.5^{+10.5}_{-12}$ arcsec. The central surface brightness I_0 can be found by integrating this β-model, and setting the result to be equal to the total number of photons detected (N_β):

$$N_\beta = \int_{\phi=0}^{2\pi} \int_{r=0}^{\infty} I_0 \left[1 + \left(\frac{r}{r_{\rm c}}\right)^2\right]^{-3\beta/2+1} r d\phi dr \qquad (4.8)$$

Substituting the previously calculated values for N_β, and $r_{\rm c}$, in eq. (4.8), a value of $0.13^{+0.20}_{-0.12}$ counts arcsec^{-2} was found for I_0.

4.5.2 Spectral analysis

The *ROSAT* PSPC data of Abell 2634 were splitted into two pointings: the first observation was obtained at the end of June 1991, with an exposure of ~9900 seconds; the second part was performed in December 1992 for ~10500 seconds.

A first attempt to define the spectrum of the X-ray emission from the galaxy that hosts 3C 465, using the PSPC data was made by Prieto (1996). In his study of the X-ray properties of 3C radio loud sources, he used only the second data set, and fitted the detected spectrum with a power law model. He found that this model requires an extreme spectral slope with a correspondingly high $N_{\rm H}$. He concluded that a thermal model would provide a better fit, but he did not attempt to use it, because of the specific target of his investigation. Subsequently, Schindler & Prieto (1997), investigating the properties of the hot gas in Abell 2634, performed a spectral analysis, again using only the second dataset. They fitted the counts detected in a region of one arcmin radius ($\sim 55 h_{50}^{-1}$ kpc) around the centre of NGC 7720 by both a Raymond-Smith and a power law model. They obtained a value of $1.2^{+0.2}_{-0.1}$ keV (χ^2/ν=18.6/31) for the temperature of the single Raymond-Smith model, and a photon index of $5.4^{+1.7}_{-2.2}$ (χ^2/ν=20.3/29) for the single power law model. In both spectral fits there was strong evidence that the absorption of the X-rays was not only due to the Galactic hydrogen. Based on these results, they concluded that the central

Table 4.2: Spectral Analysis : Comparison of the two data sets

Data set Resp. matrix	set1 dtmat6	set2 dtmat36	set1+set2 dtmat6	set1+set2 dtmat36
POWER LAW				
χ^2/ν	17.29/24	14.99/24	35.53/24	34.41/24
α	0.6	0.7	0.6	0.6
	(0.1 - 1.0)	(0.3 - 1.0)	(0.3 - 0.8)	(0.3 - 0.8)
N_{po}	0.6	0.6	0.6	0.6
($\times 10^{-4}$ cnts keV^{-1} cm^{-2} s^{-1})	(0.5 - 0.8)	(0.5 - 0.8)	(0.5 - 0.7)	(0.5 - 0.7)
RAYMOND				
χ^2/ν	7.01/24	6.83/24	11.14/24	10.51/24
kT (keV)	1.0	1.0	1.0	1.0
	(0.8 - 1.3)	(0.7 - 1.4)	(0.9 - 1.1)	(0.9 - 1.2)
N_{ray}	0.8	0.9	0.9	0.9
($\times 10^{-4}$ cm^{-5})	(0.5 - 1.3)	(0.4 - 1.4)	(0.6 - 1.2)	(0.7 - 1.2)

X-ray emission was of thermal origin, and that the active nucleus was not present in the X-ray spectrum of the host galaxy.

Given the availability of a further 10 ksec of PSPC data, we have attempted to combine the two data sets, and perform the spectral analysis using the merged set. The main difficulty in merging the two data sets is that the response matrices appropriate for them are different. The first part of the observations was performed a few months before the gain of the PSPC detector was reduced in order to eliminate some problems that had appeared. The second dataset was obtained after the gain changed.

In order to test the feasibility of an addition of the counts from the two different data sets, the spectra of the same test region in both data sets and the merged one were compared. The spectral analysis of all data sets was performed using the IRAF/PROS and the XSPEC software. Only photons in the energy range 0.2-2.2 keV were used (PI channels 6-33). The exclusion of the first PI channels is recommended because the contribution of charged particles is not well modelled in these channels. The two higher energy channels (33-34) have uncertain calibrations (Briel et al. 1997).

Inspection of the profiles of point sources detected in both data sets shows that the two PSPC images do not exactly register. In order to account for this displacement, the second data set was shifted towards the east by 15 arcsec and towards the north by 7.5 arcsec. After performing this correction, the two sets were merged and folded by both matrixes, the old and the new version (dtmat6 and dtmat36 respectively in Table 4.2). The extracted source spectra were all fitted by a Raymond-Smith and a

power law model separately. In all cases, the absorption by the Galactic hydrogen for the direction of Abell 2634 was taken into account, by using the value for its column density given by Stark et al. (1992). For the Raymond-Smith model solar abundance were assumed. The results of the spectral analysis are presented in Table 4.2. This table contains the best fit parameters for the two spectral models, using the different data sets: the second column gives the results for the first data set folded with the old version of the response matrix (dtmat6); for the results presented in column 3 the second data set folded with the new version of the response matrix (dtmat36) was used; columns 4 and 5 contain the results of the merged set folded with the old version (column 4) and the new version (column 5) of the response matrix. In parenthesis, the 1σ limits of each parameter are given. As is seen from this table, all combinations of the datasets show the same trends. One striking difference is that the χ^2 is larger for the merged sets. Such behaviour can be understood because the errors of the number of counts detected in each energy channel in the separate sets are larger (due to small number of counts), compared to the number of counts in the merged sets. Therefore, the separate sets are consistent with a wider variety of spectral models.

Having established that the merged set does not give different results from the separate ones, it was used, folded with the new version of the response matrix to obtain the spectrum of the radio galaxy. The source region was taken to be a circle centered on the peak of the X-ray emission from the galaxy and extending out to 30 arcsec, which is half of the radius previously used by Schindler & Prieto (1997) for the spectral analysis they performed. The background was an annulus outside the source region from 0.5 to 3.3 arcmin. The spectrum of the background was consistent with the previous results for the spectral properties of the ICM of Abell 2634, and it is therefore expected that the photons due to the ICM were efficiently subtracted from the spectrum of the radio galaxy.

First, the derived spectrum was fitted by a power law model. The absorption was held fixed at the Galactic value. The extracted spectrum and a χ^2 grid are presented in Fig. 4.8 (a) and (b). As can be seen from this plot, this model does not describe the observed spectrum of the source very well. The best fit value of the photon index is 1.5 (χ^2=33.0, d.o.f.=24). Leaving the Galactic absorption free led to high spectral index ($\sim$ 5.0) and high $N_{\rm H}$, following the behaviour previously noticed by Prieto (1996) and Schindler & Prieto (1997).

A better spectral fit was obtained when the data were fitted with a Raymond-Smith model. The metal abundance was held fixed to the solar value; the derived temperature of the gas is not strongly affected by the choice of the metal abundance. The

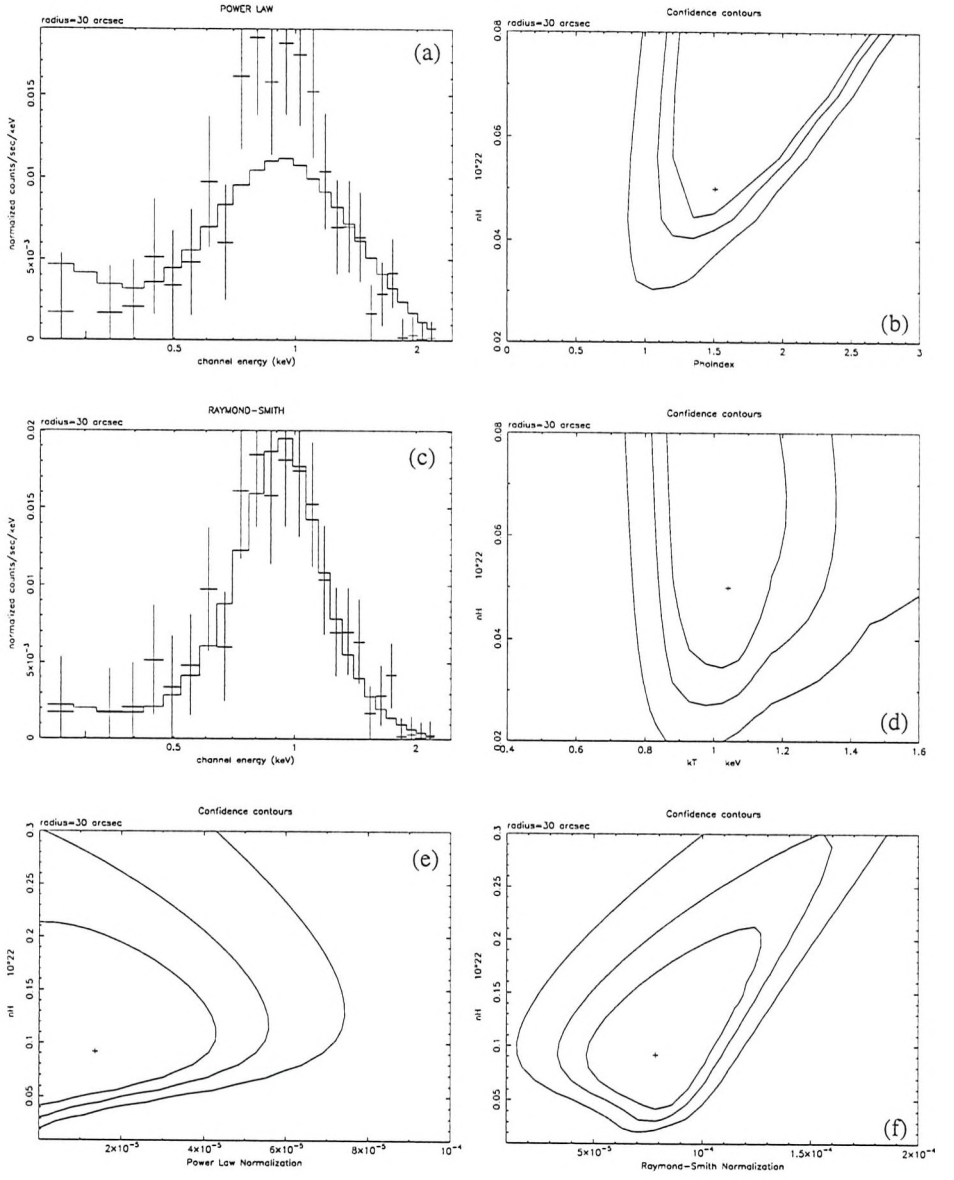

Figure 4.8: Spectral fit with a power law model: (a) The extracted counts per energy channel, and the best fit model. (b) Confidence ellipses of the Galactic $N_{\rm H}$ versus the photon index. Spectral fit with a Raymond-Smith thermal model: (c) The extracted counts per energy channel, and the best fit model. (d) Confidence ellipses of the Galactic $N_{\rm H}$ versus temperature. Composite model of power law plus Raymond-Smith model. The photon index is fixed to $\Gamma = 1.96$, and the temperature to 1 keV: (e) Confidence ellipses of the Galactic $N_{\rm H}$ versus the normalization of the power law model, and (f) confidence ellipses of the Galactic $N_{\rm H}$ versus the normalization of the Raymond-Smith model.

column density of the atomic hydrogen was fixed to the Galactic value. The observed source spectrum is compared to the best fit Raymond-Smith model in Fig. 4.8 (c). Figure 4.8 (d) presents a χ^2 grid of the $N_{\rm H}$ versus the temperature of the spectral model. The best fit value for the temperature is 1 keV (χ^2=10.8, d.o.f.=24), which is slightly lower than the temperature reported by Schindler & Prieto (1997) for a larger source region, but consistent with temperature of the X-ray haloes (Davis & White 1996). When the galactic column density was left free, the χ^2 was reduced slightly, but the best fit value for the temperature did not change significantly. As can be seen in Fig. 4.8 and in agreement with previous studies, there is not an upper limit for the absorption, when fitting with a power law model.

The last model that was compared to the observed galaxy spectrum was a combined model that consisted of a power law and a Raymond-Smith models. The photon index of the power law was held fixed at the average value found by Brinkmann & Siebert (1994) for similar sources (Γ=1.96). The temperature of the Raymond-Smith model was also fixed to the value of 1 keV. The absorption by the atomic hydrogen was left as a free parameter. This model gave a χ^2 of 9.7 for 23 degrees of freedom. A χ^2 grid plot of the $N_{\rm H}$ versus both the normalization of the power law and the normalization of the thermal model are presented in Fig. 4.8 (e) and (f) respectively. This model, as with all the previous ones, requires an excess of absorption above the Galactic value by an amount of $\sim 0.5 \times 10^{21}$ cm^{-2}.

The requirement of an extra absorption, implied by all previous fitting procedures, is justified by the presence of a very pronounced dust lane, discover by the HST (Fig. 2 in Schindler & Prieto 1997). Since the dust is always associated with neutral material, its presence in NGC 7720 suggests that there must be atomic hydrogen bound to the galaxy. This hydrogen might cause extra absorption of the X-rays, more than what is expected from the Galactic value. The dust itself also absorbs and scatters the X-rays away from the line-of-sight of the observer.

The dust lane cannot have long been associated with NGC 7720, being in an environment dominated by hot X-ray emitting gas. Dust grains can be destroyed by the collisional interactions with the hot gas particles. Such collisions transfer charge, momentum, mass and energy between the two phases. The typical grain lifetimes in environments with densities of the order of $\sim 10^{-3}$ to 10^{-2} cm^{-3} and temperature of 10^7 to 10^8 K (similar to the densities and temperatures of X-ray haloes) are $\sim 10^7$ to 10^8 yr (Dwek & Arendt 1992). Thus, the origin of the dust lane must be sometime in the recent history of NGC 7720, and its presence might explain the excess of absorption required by the spectral model fits.

4.5.3 X-ray halo, X-ray binaries, or cooling flow?

The analysis of the HRI data (§4.5.1) has revealed an extended component, which contributes to the total X-ray emission from NGC 7720. One possible explanation for its presence, which is also supported by the results of the spectral analysis, is that it is the X-ray image of the hot ISM. However, the bent radio jets imply that NGC 7720 is moving relative to the ICM in Abell 2634. As was explained in chapter 3, such a motion can strip off the gas content of a galaxy if ram pressure is efficient enough. Is NGC 7720 able to retain its ISM? As in chapter 3, the answer will come from the comparison of the gravitational force that holds the gas within the galaxy with the force due to ram pressure.

The maximum gravitational restoring force [$F_{\rm GR}$; eq. (3.2)], that holds the ISM inside the galaxy is:

$$F_{\rm GR} = \frac{4}{3}\pi\ R_{\rm gal}^3 \rho_{\rm ISM}\ \frac{GM_{\rm gal}}{R_{\rm gal}^2}, \tag{4.9}$$

where $M_{\rm gal}$, and $R_{\rm gal}$ are the total mass and radius of the galaxy, and $\rho_{\rm ISM}$ the density of the galaxy's ISM. The force due to ram pressure ($F_{\rm RP}$) is given by eq. (3.3).

Gas is liberated from the galaxy when:

$$F_{\rm RP} > F_{\rm GR} \tag{4.10}$$

$$n_{\rm ICM} v_{\rm gal}^2 > \frac{4}{3} n_{\rm ISM} \frac{GM_{\rm gal}}{R_{\rm gal}} \tag{4.11}$$

A measure of the strength of the galactic gravitational potential is provided by the line-of-sight velocity dispersion of its stars. If T is the total kinetic energy of the stars, and Ω the gravitational potential energy, according to the virial theorem:

$$2T + \Omega = 0 \tag{4.12}$$

These two quantities are connected to the total mass of the galaxy, the radius of the galaxy, and the line-of-sight velocity dispersion (σ_r), as follows (Lang 1980):

$$T \approx \frac{M_{\rm gal}\sigma_r^2}{2},\ \ \Omega \approx -\frac{GM_{\rm gal}^2}{R_{\rm gal}} \tag{4.13}$$

From (4.12) and (4.13) it follows that:

$$\sigma_r^2 \approx \frac{GM_{\rm gal}}{R_{\rm gal}} \tag{4.14}$$

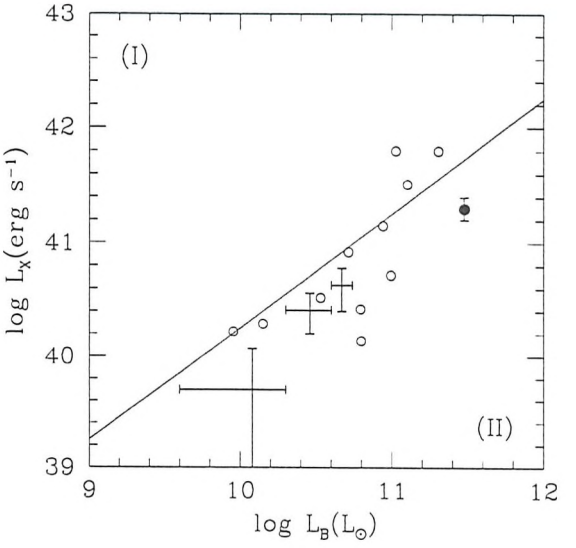

Figure 4.9: X-ray luminosity versus blue luminosity for early-type galaxies. The locations in this plane of the galaxies that belong to the Virgo cluster are marked with open circles, and to Abell 2634 with crosses (see chapter 3). The position of NGC 7720 is shown as a filled circle.

Taking (4.14) into account, the condition of (4.11) takes the form:

$$n_{\rm ICM} v_{\rm gal}^2 > \frac{4}{3} n_{\rm ISM} \sigma_r^2 \tag{4.15}$$

The line-of-sight velocity dispersion of NGC 7720 is $\sigma_r = 305$ km s^{-1} (Mobasher & James 1996). In §4.3 it was found that the maximum velocity at which it is moving relative to the ICM is $v_{\rm gal} = 293$ km s^{-1}. Since the galaxy is now located inside the core region of Abell 2634, a reasonable value for the density of the ICM is the central number density calculated in §4.2 ($n_0 = 1.14 \times 10^{-3}$ cm^{-3}). Under these conditions, NGC 7720 can retain an ISM with number density of $\simeq 0.01$ cm^{-3} (the common density of X-ray haloes; Trinchieri, Fabbiano & Kim 1997), since $F_{\rm GR}/F_{\rm RP} \simeq 15$.

Another clue for the origin of the extended X-ray component comes from the comparison of the optical and X-ray properties of NGC 7720 with those of early-type galaxies, as was done for all the galaxies of Abell 2634 in chapter 3.

The apparent blue magnitude of NGC 7720 is $m_{\rm B}$=13.4 mag (NED). After correcting for the galactic extinction, and applying the appropriate K-correction, the absolute blue magnitude is found to be $M_{\rm B}$=-23.25 mag, which corresponds to a blue luminosity of $L_{\rm B} = 3.0 \times 10^{11}$ L$_\odot$.

The normalization of the β-model (N_β) calculated in §4.5.1 provides a measure of the X-ray luminosity of the extended component. Using the PIMMS software to convert the count rate detected by the HRI detector to X-ray luminosity, it is found that $L_{X,\beta}(0.2-3.5 \text{ keV}) = 2.0^{+1.0}_{-0.4} \times 10^{41}$ erg s^{-1}, where $L_{X,\beta}$ is the X-ray luminosity of the extended component. For this conversion, the spectrum of the source was modelled by a Raymond-Smith model of 0.862 keV temperature, and the absorption due only to the Galactic hydrogen was taken into account.

This set of optical and X-ray luminosities specify a position on the $L_B - L_X$ plane where the X-ray emission is believed to come only from the stellar population of the galaxy (region II in Fig. 4.9). Thus, the comparison of the X-ray and optical properties of NGC 7720 supports a stellar origin for the extended X-ray emission found by the HRI. Additionally, the surface brightness distribution in the X-ray energy range follows closely the light distribution of the galaxy in the optical presented by Colina & de Juan (1995), which further favours a stellar origin. However, if this is the explanation of the origin of the extended component, the spectrum of this emission should be harder, giving a best fit temperature for the Raymond-Smith model around 5 keV.

Schindler & Prieto (1997), based on the results of the spectral analysis of the PSPC data, which revealed a decline in the temperature of the ICM towards the cluster centre, proposed that the centre of Abell 2634 harbours a cooling flow. In the central region of some clusters of galaxies, where the atmosphere is densest, the ICM cools rapidly. The weight of the overlying gas causes a slow inflow towards the centre of the cluster, and a cooling flow is established. Cooling flows have been found many times to peak at the cD galaxy which is located in the core region of the cluster, as for example in A2597 (Sarazin & McNamara 1997), and in A1795 (Pinkney et al. 1996). The extent of this cooling region varies from 100 to 250 kpc.

A cluster of galaxies has had time to develop a cooling flow only if the radiative cooling time [$t_{cool} = (d \ln T_{ICM}/dt)^{-1}$; Sarazin (1986)] is smaller than the age of the Universe (Fabian 1994). The cooling time is well approximated by:

$$t_{cool} = 8.5 \times 10^{10} \left[\frac{n_{ICM}}{10^{-3} \text{ cm}^{-3}}\right]^{-1} \left[\frac{T_{ICM}}{10^8 \text{ K}}\right]^{1/2}, \text{ yr} \qquad (4.16)$$

Applying eq. (4.16) for the conditions in Abell 2634, it is found that the cooling time is $t_{cool} = 5 \times 10^{10}$ yr, larger than the Hubble time. This calculation argues against the presence of a cooling flow that peaks on the cD galaxy. Besides, according to the results of chapter 2, NGC 7720 has not always been at the centre of the cluster, and

even at the present time it is not stationary relative to the ICM. So, one would not expect any cooling flow to be centered on this galaxy.

From the above discussion it is apparent that the origin of the X-ray emission from NGC 7720 is far from a clear cut. The high spatial resolution of the HRI detector has uncovered the presence of two components that contribute to the total X-ray emission: an unresolved component, which is possibly due to the emission from the active nucleus; and an extended component, whose origin is not yet clear. The luminosities of these two components are: $L_{\rm PSF}(0.2-2.2\ {\rm keV}) = 5.1^{+0.1}_{-1.8} \times 10^{41}$ erg s^{-1}, and $L_\beta(0.2-2.2\ {\rm keV}) = 2.0^{+0.3}_{-0.4} \times 10^{41}$ erg s^{-1} respectively. These luminosities were obtained from the total counts detected from each component using the PIMMS software. The unresolved emission was modelled by a power law with $\Gamma = 1.96$, and the extended one by a Raymond-Smith model of kT=1 keV. Although the strength of the emission from both components appears similar in the HRI detector, the spectrum of the galaxy is dominated by the thermal emission.

The position of NGC 7720 on the $L_{\rm X}-L_{\rm B}$ plane and the comparison with the optical light distribution suggest a stellar origin for the extended component. Ram pressure does not seem to be effective at the present time, but gas could have been removed at an earlier date, while the galaxy was heading towards the central region of the cluster at higher speeds. However, if the stars and the X-ray binaries are responsible for this emission, one would have expected a higher characteristic temperature for the emission.

4.5.4 The ISM/ICM interface

In this section the feasibility of a search for the interface between a putative ISM and the ICM of Abell 2634 is tested. This test will give a better understanding of the limitations inherent in such an investigation.

If all the X-ray emission from the extended component detected by the HRI comes from the hot gas associated with NGC 7720, the deprojection of the X-ray light profile provides the density distribution of the gas, just as has previously been done for the ICM of clusters of galaxies. Following the method explained in Appendix A, it is found that the central number density of the ISM is $10.0^{+12.2}_{-0.5} \times 10^{-3}$ cm^{-3}, which is in excellent agreement with the recent results from PSPC observations of early-type galaxies by Trinchieri, Fabbiano & Kim (1997).

The position of the interface between the ISM and the ICM is defined by the position where the two media are in pressure balance. Figure 4.10 (a) shows the pressure distribution of both the ISM and the ICM. The position of the ISM/ICM interface

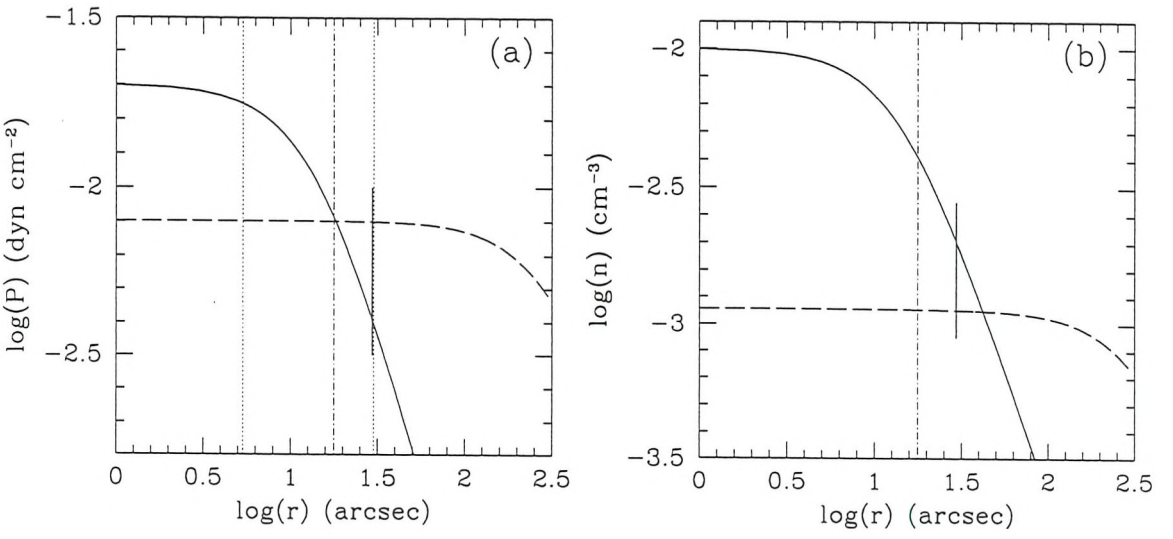

Figure 4.10: (a) The pressure distribution of the gas associated with NGC 7720 (solid line) and the ICM of Abell 2634 (dashed line). The perpendicular dot-dashed line shows where the two media are in pressure balance, which is taken to be the position of the ISM/ICM interface. The two dotted perpendicular lines show the 1σ limits of the position of the ISM/ICM interface, after taking into account the errors of the central number density and core radius of the ISM distribution. The short solid perpendicular line shows where the flaring in the jets of 3C 465 occurs. (b) The density distribution of the two media as in (a). The perpendicular dot-dashed line is the position of the ISM/ICM interface, and the solid perpendicular line the position of the flaring of the jets.

is marked with the perpendicular dot-dashed line. Both pressure distributions were calculated using the relationship $P = 2nkT$. For the density distributions of the ISM and ICM the functions derived in §4.5.3 and §4.2 were used respectively. The temperatures of the ISM and the ICM were taken to be 1 keV and 3.5 keV respectively. The 1σ limits for the position of the interface were also calculated taking into account only the error in the core radius of the ISM distribution, and are shown in Fig. 4.10 (a) as perpendicular dotted lines. Figure 4.10 (b) presents the density distribution of both media. In both figures the solid perpendicular line marks the projected position of the hot-spots in the jets of 3C 465. For any position of the interface within the allowed range, the density drop from one medium to the other was found to be always $R_\rho = \rho_{\rm ISM}/\rho_{\rm ICM} \sim 3.6$. This value is closer to the density difference used in the simulations of Hooda & Wiita (1996; $R_\rho = 5$), but it is not as high as the value used in the simulations of Loken et al. (1995) ($R_\rho = 10$).

However, if the uncertainty of the central number density of the ICM and especially the uncertainty of its temperature [1σ limits of $T_{\rm ICM}$ are 2.5 and 5.5 keV (Schindler & Prieto 1997)] are taken into account, the permitted range for the position of the interface becomes much wider (it could, for example, be at a distance of 40 arcsec). Therefore, even if the extended component discovered using the HRI detector represents the emission from the X-ray halo of NGC 7720, the present X-ray data cannot lead us to a firm conclusion for the position of the ISM/ICM interface. The nature of such an investigation requires accurate measurements of the temperature of the two media, and hence X-ray data with high spectral resolution.

4.6 Another hypothesis: a shock wave

As mentioned in §4.4, another explanation for the flaring of the radio jets is that they cross a shock wave, for instance the bow shock formed in front of a supersonically moving galaxy. The sound speed of the ICM in Abell 2634 is $c_s^2 = \gamma k T_{\rm ICM}/\mu m_p \sim$ 750 km s^{-1}. In §4.3 it was found that NGC 7720 is not moving at a speed greater than 293 km s^{-1}, relative to the ICM. Thus, the motion of NGC 7720 is not supersonic, a bow shock cannot have been created, and therefore this scenario does not account for the flaring of the jets in 3C 465.

4.7 Summary and Conclusions

ROSAT HRI data of Abell 2634 have been used in combination with observations obtained by the PSPC detector to study the morphology of the jets in 3C 465. The jets in this radio galaxy originate from the host galaxy as narrow, well collimated structures. Suddenly, at a distance of $\sim 30 h_{50}^{-1}$ kpc, they widen and bend into the well-known C-shape of a WAT source.

The large scale bending of 3C 465 can be attributed to the combined action of ram pressure and buoyancy. By using the properties of the ICM inferred from the X-ray data, and looking at a special point in the jets of this radio galaxy where ram pressure and buoyancy exactly balance, the velocity of the galaxy relative to the ICM has been calculated, independent from the jet velocity. It has been found that a galaxy velocity lower than 280 km s^{-1} on the plane of the sky can account for the bending of the kiloparsec-scale radio jets. Taking into account the galaxy's line-of-sight velocity, it has been found that 3C 465 is not moving at a speed greater than 293 km s^{-1} relative to the ICM.

Using the calculated galaxy velocity, and applying the hydrodynamical model that describes the bending of the jets for a different point on the jets, the velocity of the kiloparsec-scale jets has also been calculated. Even if the jets are very rarefied ($\rho_j/\rho_{ICM} = 10^{-3}$), their velocity can not be greater than ~ 3200 km s^{-1}. This result shows that the jets must decelerate by a large factor ($\gtrsim 55$) at the hot-spots.

Several explanations have been proposed for the sudden flaring and the subsequent deceleration of the radio jets. One of them suggests that the hot-spots designate the position of the interface between the ISM and the ICM of the surrounding cluster. The *ROSAT* HRI and PSPC data have been used to test this hypothesis by exploring the properties if the X-ray emitting ISM.

The nature of the X-ray emission from the galaxy that host 3C 465 is rather puzzling. The main results can be summarized as follows:

1. The HRI data reveal the presence of an unresolved component and a weaker, extended component in the X-ray image of 3C 465.

2. The PSPC spectrum is better fitted by a thermal model of $kT \sim 1$ keV, although the presence of a weak power law component cannot be ruled out. Such a temperature is characteristic for X-ray haloes.

3. Theoretical arguments indicate that ram pressure is not efficient at the present time in removing the ISM from within the galaxy.

4. The deprojection of the light profile of the extended component gives a number density in excellent agreement with the densities of X-ray haloes.

5. Comparison of the optical and X-ray properties of NGC 7720 with those of early-type galaxies supports a stellar origin for the X-ray emission.

6. The optical light profile of NGC 7720 seems to follow its profile in the X-rays.

Given these contradicting results a firm conclusion as to the nature of the hot-spots cannot be reached. This investigation is mainly hampered by the poor spectral resolution of the X-ray detectors. Future observations of higher spatial and spectral resolution with the *AXAF* satellite will help us to accurately calculate the parameters of interest, and answer the question whether the hot-spots indicate the position of the ISM/ICM interface.

Chapter 5

A WAT in a poor cluster: 4C 34.16

5.1 Introduction

The WAT radio source 4C 34.16 is located in a nearby (z=0.078; Gregory & Burns 1982) Zwicky cluster (Z0357.9+3432) of richness class 0 – 1 (Burns, Gregory, Holman 1981). This radio galaxy has a very symmetric structure which suggests that the bending of its jets might be explained by a simple dynamical model. Additionally, it has a steep low frequency radio spectrum, with a spectral index of $\alpha > 1.2$ ($F_\nu \sim \nu^{-\alpha}$) in the frequency range from 38 MHz to 178 MHz (Baldwin & Scott 1973). Such steep spectra arise when jets are confined against adiabatic dissipation for so long that radiative losses steepen the spectrum right down to low frequencies. This confinement is almost certainly provided by the ICM of a surrounding cluster of galaxies.

Previous X-ray observation performed with the *Einstein* IPC (Burns et al. 1981) revealed that 4C 34.16 is indeed surrounded by the ICM of a poor cluster of galaxies. Although the poor spatial resolution of the IPC (FWHM $\sim$ 1.5 arcmin) did not reveal the fine structure of the gas, the *Einstein* image gives the first hint that the ICM of this cluster is perturbed and that it is worthy of more detailed examination. Additionally, Z0357.9+3432, being a poor cluster, is a good candidate for revealing details of any interactions since the energy density stored in such an ICM is relatively low, and so its response to the impact from the jets will be much more apparent than in richer systems. Further, this response is more readily detectable in poor systems because any X-ray perturbations in larger clusters will be diluted by the long column of non-interacting hot gas through which the interaction is observed.

Therefore, in order to uncover the fine structure of the ICM surrounding 4C 34.16, and investigate the mechanisms responsible for the bending of the jets, *ROSAT* PSPC X-ray observations of the field around the radio galaxy were obtained. In the next

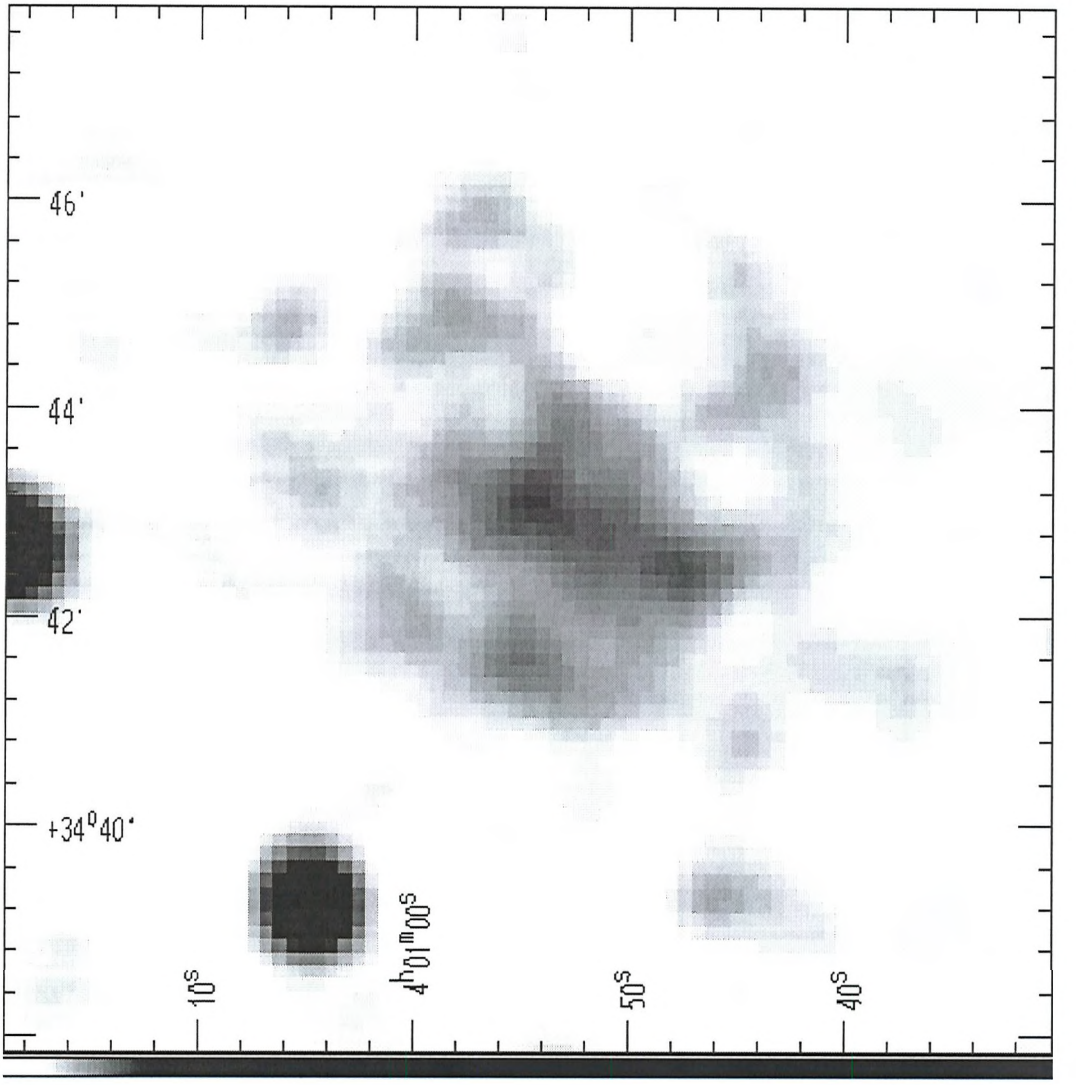

Figure 5.1: Grey-scale *ROSAT* PSPC image of the field around the WAT source 4C 34.16 overlaid by the radio map at 20 cm. The X-ray image pixel size is 7.5 arcsec, the image has been smoothed using a Gaussian kernel of σ=15 arcsec and plotted with high contrast so that the detailed structure of the ICM is apparent. The contour levels of the radio map are at 1.0, 2.0, 5.0, 10.0, 20.0, 40.0, and 80.0, per cent of the peak value (126.83 mJy beam^{-1}).

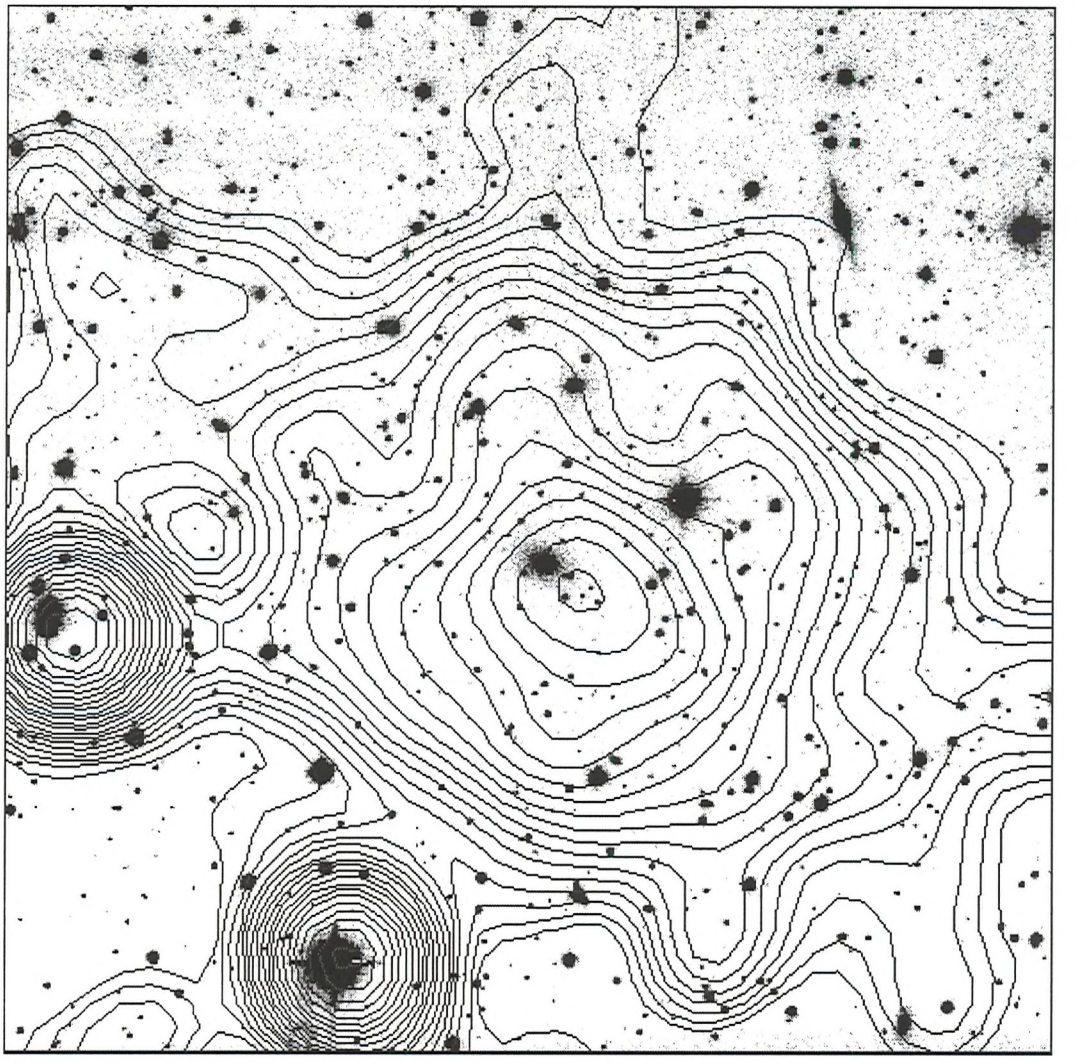

Figure 5.2: Contour map of the inner part (11×11 arcmin^2) of the 0.4-2.2 keV X-ray image overlaid upon the optical image of the same area in the sky. The data have been quite heavily smoothed using a Gaussian kernel with dispersion of $\sigma = 30$ arcsec in order to reveal the large-scale distribution of gas in the system. The contour lines are from 10 to 100 percent of the peak value, and are spaced logarithmically in intervals of 0.05 dex.

section the X-ray data along with their spatial and spectral analysis are presented. In §5.3 the model for the bent jets described in §4.3 is used to calculate the galaxy and jet velocities. The last sections are devoted to the interpretation of a feature of X-ray emission revealed by the PSPC image, the X-ray wake.

5.2 X-ray Observations

The field that contains 4C 34.16 was observed using the PSPC on the *ROSAT* satellite in September 1993 for 22792 seconds. Extended X-ray emission was detected around the radio source, as expected for the ICM of a poor cluster. The cluster emission is completely contained within the central ~ 0.3 circular aperture bounded by the PSPC rib-support structure. The source is therefore only mildly affected by the energy-dependent vignetting function of the X-ray telescope. A grey scale image of the X-ray emission from the cluster covering the full (0.1-2.5 keV) energy range of the PSPC is presented in Fig. 5.1, overlaid by the radio map at 20 cm. Figure 5.2 is the optical image (Sakelliou et al. 1996) of the field around the big galaxy that hosts the radio source overlaid by a contour map of the X-ray emission.

5.2.1 Spatial analysis

Spatial analysis of the PSPC data was performed using the IRAF PROS 'xspatial' package. In order to obtain the general characteristics of the ICM of the cluster (ie. its central density) and to compare them with previous findings of similar systems, the traditional analysis was performed. Such an analysis assumes that the ICM is spherically symmetric, in equilibrium within the gravitational potential of the cluster, and it has been found to be a very good first order approximation (e.g. Schindler 1996).

The X-ray image shows that the emission from the group can be traced out to ~ 7.5 arcmin ($\simeq 1$ Mpc). The peak of the emission, which is used to define the centre of the cluster, does not coincide with the position of the galaxy, but lies ~ 38 arcsec to the southwest [$\alpha = 04^{\rm h}\ 00^{\rm m}\ 52.2$, $\delta = 34^{\circ}\ 42'\ 50.5''$ (J2000)]. The surface brightness profile of the intra-cluster gas was obtained from an unsmoothed 0.4-2.2 keV image. Photons were counted in 20 concentric circular annuli around the cluster centre and extending out to the limits of the cluster. The width of each annulus was 22.5 arcsec. The emission from other point sources detected within the field was removed and the background, taken from an annulus between 7.5 arcmin and 15 arcmin, was subtracted.

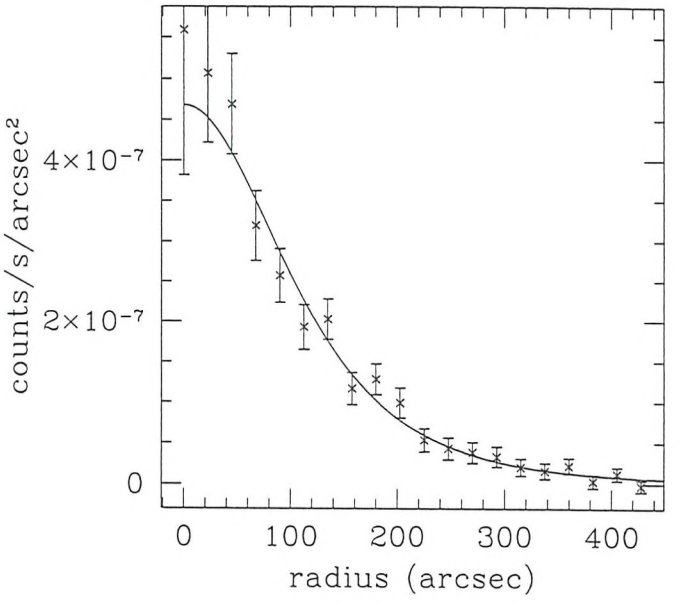

Figure 5.3: Radial surface brightness profile in the energy range 0.4 to 2.2 keV. The solid line represents the best fit model.

The X-ray data were fitted by the β-model of eq. (A.15), leaving the central surface brightness (I_0), the core radius (r_c), and the β index as free parameters. The extracted counts from each annulus and the best fit model are presented in Fig. 5.3. The best fit model yielded a value for the β parameter of 0.9 ± 0.2, which is on the high side of the values found from *Einstein* observations of poor clusters of galaxies ($\beta = 0.4 - 0.7$; Price et al. 1991). This result indicates that the gas distribution is steeper and more centrally concentrated than in most of the groups and poor clusters of galaxies studied by Price et al. Interestingly, such a high β value was also found for the gas distribution in the 'fossil' group RX J1340+4018 (Ponman et al. 1994), which is similarly dominated by a single large elliptical galaxy. The other two parameters of the fit are: core radius $r_c = (3.0 \pm 0.7)$ arcmin $= (0.4 \pm 0.1)$ Mpc; and $I_0 = (2.4 \pm 0.1)$ cnts pix^{-1} (χ^2=13.76 for 17 degrees of freedom). The central surface brightness can be converted to unabsorbed energy flux of the source once we take into account the spectrum of the emitting gas and the galactic hydrogen absorption (see §5.2.2). This calculation yields $I_0 = (3.6 \pm 0.2) \times 10^{-6}$ erg s^{-1} cm^{-2} . Previous X-ray observations (e.g. Price et al. 1991; Doe et al. 1995) have found the core radii of groups and poor clusters of galaxies to be less than 250 kpc; a value as large as

400 kpc is usually reserved for rich clusters (e.g. Jones & Forman 1984). However, larger than average core radii have been found in systems which show evidence of dynamical activity such as a recent merger event (e.g. Burns et al. 1995). Therefore, the large value for 4C 34.16 provides an indication that the ICM in this cluster might have been recently disturbed.

Inspection of Fig. 5.3 seems to indicate that the β-model does not fit the central points particularly well. Excesses in the central emission above the values predicted by the conventional β-model have previously been seen in many clusters of galaxies (e.g. Jones & Forman 1984; Edge, Stewart & Fabian 1992). Accompanied by a drop in gas temperature towards the cluster centre, these features have been attributed to the existence of cooling flows (Fabian, Nulsen & Canizares 1984; Fabian 1994). However, given the poor statistics in the current data, this central excess is not significant, and exclusion of the central points from the data set did not improve the fit.

As is discussed in Appendix A, the density of the X-ray emitting gas can be obtained by deprojecting its surface brightness distribution, using eq. (A.16). Assuming a gas temperature of $kT_{\rm gas} = 1$ keV (§5.2.2), a central number density of $n_0 = (0.8 \pm 0.2) \times 10^{-3}{\rm cm}^{-3}$ is derived. This number density is in agreement with the value obtained by Burns et al. (1981) in their analysis of the *Einstein* satellite observations of this cluster, and it is also consistent with the central densities found in other poor clusters of galaxies (e.g. Doe et al. 1995; Mulchaey et al. 1993).

5.2.2 Spectral analysis

Spectral analysis of the gas around the 4C 34.16 radio source was performed with the IRAF/PROS 'xspectral' package. A circle centered at the cluster centre and extending out to 5.83 arcmin was used to extract the spectrum of the extended emission around 4C 34.16. The background region was specified by an annulus around the source region and extending out to 12.5 arcmin. The point sources embedded in the source and the background regions were excluded. After background subtraction the source region yielded 847 ± 50 counts.

The extracted spectrum was fitted by an absorbed Raymond-Smith (1977) thermal plasma model which takes into account the free-free continuum and the line emission from heavy elements. The model was convolved with the calibrated telescope and instrument response, and fitted to the data. During the fit, the normalization, the temperature $T_{\rm gas}$, and the galactic hydrogen column density $N_{\rm H}$ were left as free parameters, while the redshift, internal absorption, and metal abundance were held fixed. A negligible internal absorption at the cluster was assumed. A series of fits

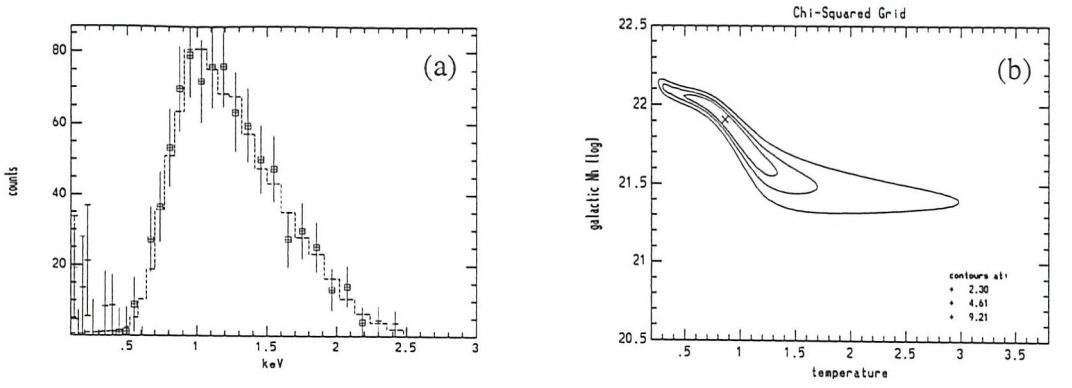

Figure 5.4: (a) The extracted total counts per energy channel and the best fit Raymond-Smith (1977) spectrum model (dashed line). Only the points which are marked with boxes were included in the calculations of the best fit model. (b) Confidence ellipses of the galactic $N_{\rm H}$ versus the temperature $T_{\rm gas}$ in the χ^2 grid. Contours at 67, 90, and 99 per cent are shown.

were performed with different values of the abundance, ranging from 10 to 100 per cent the cosmic abundance. The minimum χ^2 was found for an abundance of 40 per cent, in agreement with the abundances previously found in clusters of galaxies (e.g. Edge & Stewart 1991). Figure 5.4(a) shows the extracted spectral data and the best fit spectrum, and Fig. 5.4(b) presents the confidence limits on $N_{\rm H}$ and $T_{\rm gas}$ in a χ^2 grid at significance levels of 68, 90, and 99 per cent. The Raymond-Smith model gives a galactic absorption column density which is significantly greater than the value obtained from 21-cm observations ($N_{\rm H} = 1.2 \times 10^{21}$ cm^{-2}; Stark et al. 1992). This difference could be an indication either of a local excess in the galactic $N_{\rm H}$, as previously suggested for other sources (e.g. Johnstone et al. 1992), or it could imply the existence of a cool component of atomic hydrogen in the gas around 4C 34.16. The first possibility is favoured by the fact that 4C 34.16 is at low galactic latitude, where hydrogen column density can vary rapidly with position; since the beam width of the radio telescope which was used to map the atomic hydrogen distribution in the Stark et al. survey is 2.5 degrees, any small-scale excess in the hydrogen column would not appear in their data. Under these circumstances our spectral fit is not able to give a reliable result for the gas temperature, since the source of the absorption is not clearly known. Throughout the remainder of this chapter a credible temperature for the gas of $kT_{\rm gas} = 1$ keV is adopted, and where necessary the way that the results depend on the adopted temperature is stated.

An estimate of the unabsorbed X-ray luminosity at the rest frame of the cluster is

Table 5.1: Parameters of the group.

z	0.078
β	0.9 ± 0.2
r_c	(0.4 ± 0.1) Mpc
n_0	$(0.8 \pm 0.2) \times 10^{-3}\mathrm{cm}^{-3}$
kT_{gas}	~ 1 keV
$L_x(0.2-2.2$ keV)	2×10^{43} erg s^{-1}

given in Table 5.1. This luminosity was calculated assuming a hydrogen column equal to the value given by Stark et al. (1992); it is higher than the value calculated by Burns et al. (1981) because they did not include the absorption of the X-ray emission by the galactic hydrogen in their analysis.

5.3 The bending of the jets

The radio galaxy 4C 34.16 was the first WAT source whose jets' shape was used to derive the projection of the galaxy velocity onto the plane of the sky (Sakelliou et al. 1996), in a similar way as to that developed in chapter 4.

The radio map of 4C 34.16 (Fig. 5.1) shows clearly that the radio jets exhibit the double bend, encountered previously in chapter 4. Near the galaxy, the jets are bent towards the cluster centre but further downstream they change direction, travelling away from the cluster centre. As for the WAT 3C 465 (chapter 4), the first bend can be attributed to ram pressure resulting from the relative motion of the galaxy through the ICM. At larger radii buoyancy takes over as the dominant force, and the jets change direction towards lower density regions in the ICM. In this section, the results of the analysis presented in Sakelliou et al. (1996) and in chapter 4 are given. The special characteristics of the turn-over point (the position where the curvature of the jets changes direction) were used to calculate the galaxy velocity. Although there is no additional information of the true orientation of the source in the 3-dimensional space, as was available for 3C 465, the assumption that 4C 34.16 lies on the plane of the sky is fair and safe: the symmetry of this radio source in the radio maps (Fig. 5.1) supports such an assumption; the analysis of chapter 4 shows that projection effects do not severely affect the calculated values of the galaxy and jet velocities.

The projection of the galaxy velocity onto the plane of the sky was calculated using

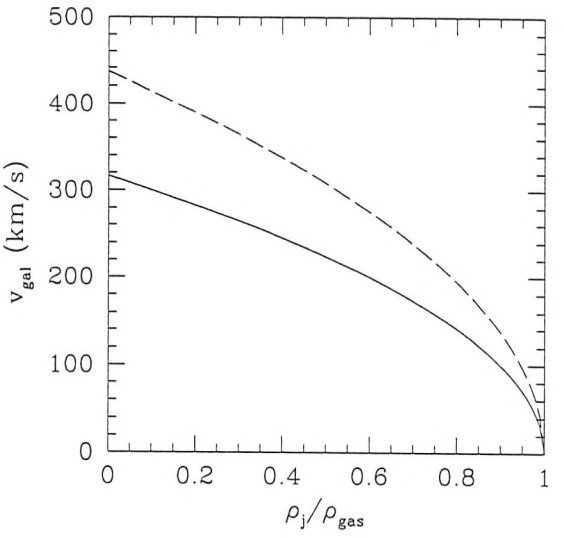

Figure 5.5: The calculated galaxy velocity ($v_{\rm gal}$) versus the $\rho_j/\rho_{\rm gas}$ ratio. The solid line represents the result for a gas temperature of $kT_{\rm gas} = 1$ keV, while the dashed line is for $kT_{\rm gas} = 2$ keV.

eq. (4.6), and the result is plotted in Fig. 5.5.

As expected, there is an upper limit on the velocity of 4C 34.16 relative to the ambient gas of $v_{\rm gal} \leq 300$ km s^{-1}. Due to the uncertainty in the gas temperature (§5.2.2) the same calculations were conducted with a gas temperature of 2 keV. The resulting galaxy velocity is also shown in Fig. 5.5 (dashed line). The increase in the permitted galaxy velocity can be understood by noting that as the temperature of the ICM becomes higher, buoyancy becomes more effective. Consequently, ram pressure must increase to balance buoyancy. Since the dependence of the gas density on the temperature is not very strong, increase in the ram pressure must be accompanied by an increase in the galaxy velocity.

It should also be recalled that $v_{\rm gal}$ only measures the velocity of the galaxy on the plane of the sky. If the galaxy also has a significant line-of-sight component to its velocity, then the total speed of the system will be somewhat higher. In principle, of course, the line-of-sight component can be measured directly by comparing the redshift of the galaxy to the average of other cluster members. However, the paucity of this cluster would render such a measurement very difficult in practice.

Away from the turn-over point, the shape of the jets also depends on the jet velocity v_j. An estimate of the velocities of the jets in this system is obtained by

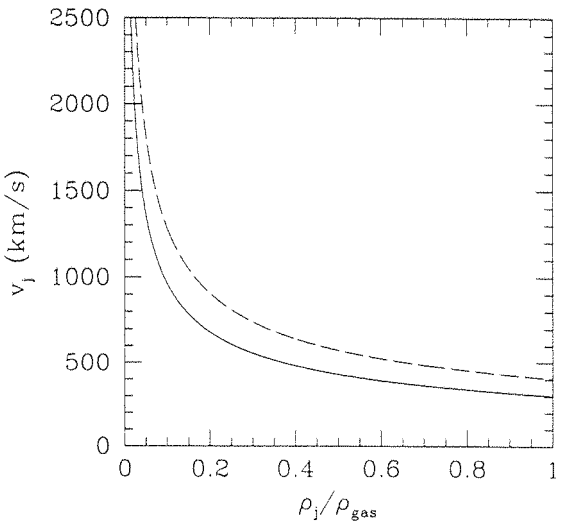

Figure 5.6: The velocity of the jets (v_j) at a point close to the galaxy as a function of the $\rho_j/\rho_{\rm gas}$ ratio, calculated for $v_{\rm gal} = 300$ km s^{-1} (solid line), and $v_{\rm gal} = 400$ km s^{-1} (dashed line).

applying eq. (4.5) to a part of the jet closer to the galaxy. The results of such an analysis are presented in Fig. 5.6, which shows a plot of the predicted jet velocity versus the $\rho_j/\rho_{\rm gas}$ ratio, where ρ_j and $\rho_{\rm gas}$ are the densities of the jet and the ICM respectively. In these calculations, galaxy velocities of $v_{\rm gal} = 300$ km s^{-1} (solid line), and $v_{\rm gal} = 400$ km s^{-1} (dashed line) were used, as inferred from the previous analysis. The radius of curvature at that point measured from our radio map is $R = 50$ arcmin and the scale height $h = 37.5$ arcsec. In agreement with the jet velocities calculated in other 'C' shape radio sources using similar arguments (chapter 4, Bridle & Perley 1984), the derived velocity for the jet is restricted to low values.

5.4 Substructure in the X-ray image

Inspection of the X-ray emission in figures 5.1 and 5.2 reveals that the simple axisymmetric model which was used in §5.2.2 to describe the surface brightness distribution of the gas around 4C 34.16 is an oversimplification. The large scale emission is elongated (Fig. 5.2). On smaller scales the most striking and dominant feature in the *ROSAT* data is a strong wake of X-ray emission between the radio lobes. Such structures in the ICM have been previously observed in other clusters of galaxies such as

Abell 400 (Beers et al. 1992; Burns et al. 1994), Abell 2634 (Burns, Eilek & Owen 1982; Pinkney et al. 1993; Burns et al. 1994), the NGC 5044 group of galaxies (David et al. 1994), and the cluster which hosts the 1919+479 radio source (Pinkney et al. 1994). If we attribute the bending of the radio jets to the effect of ram pressure (see §5.3), we can identify the direction in which the radio galaxy is traveling relative to the ICM with the direction traced by the wake. As was mentioned in the introduction (chapter 1), such a trailing wake occurs naturally as a consequence of the motion of the galaxy relative to the ICM: the ICM is focussed by gravitational interaction as it passes the galaxy, and is thus concentrated downstream. This mechanism was first explored by Bondi & Hoyle (1944) in the context of stellar accretion (Bondi-Hoyle accretion). Hunt (1971) performed quantitative calculations of subsonic and supersonic accretion flows for the case of a point source moving through an adiabatic gas, simulating the relative motion of a galaxy through the ICM. Such a wake has also been mooted as the source of the asymmetries in the X-ray emission from the Coma cluster, where even slow subsonic motion of one of the cluster's dominant galaxies through the surrounding ICM, with a velocity of $\sim$ 200 km s^{-1}, can account for the concentration of material behind the galaxy and the creation of a wake (De Young, Condon, Butcher 1980). Recently, more sophisticated three-dimensional simulations of Bondi-Hoyle accretion have been performed (Ruffert & Arnett 1994; Ruffert 1994; Ruffert 1995; Ruffert 1996). In these simulations totally absorbing spheres of varying sizes (from 0.01 to 10 accretion radii) move at speeds spanning from subsonic (M=0.6; M is the Mach number) to supersonic (M=10) relative to homogeneous media of different adiabatic indices. One of the most important results of these simulations is that they make it clear how sensitively the detailed structure of the perturbed medium depends on the initial conditions of each individual case. We therefore do not know in detail how the resulting structure (e.g. the density, length, and age of the wake) will be affected if, for example, the 'totally absorbing sphere' were replaced by a more realistic galaxy model. It is important also to note that the results presented in these papers generally show the systems at the end of the simulations, when in most cases a steady state has developed. Interestingly, in the early parts of these simulations all systems display a local density maximum downstream from the accretor, and these structures appear remarkably similar to the wake seen in the X-ray image of 4C 34.16.

A further strange feature in the X-ray emission is the ring apparent in Fig. 5.1 at a distance of $\sim$ 2.5 arcmin from the galaxy. It is not clearly seen in Fig. 5.3 because it is not concentric with the annuli we used to obtain the surface density distribution of the ICM. This structure appears remarkably similar to the lens-shaped shock front seen

in simulated images of merging clusters (Schindler & Müller 1993, Schindler 1996).

In the next sections the properties of the wake are calculated from the X-ray data. Whether these properties are consistent with the derived limits on the galaxy velocity calculated in §5.3 is also investigated.

5.5 The X-ray wake

The range of galaxy velocities found by modelling the interaction of the jets with the ICM imply that the galaxy is moving subsonically relative to the ICM, since the speed of sound in an adiabatic gas of temperature 1 keV is $c^2 = \gamma kT/\mu m_p \sim 550$ km s^{-1}. The characteristic length scale for the Bondi-Hoyle accretion is the accretion radius $R_A = 2GM_{\rm gal}/v_{\rm gal}^2$ (Hunt 1971). This length defines the distance from the galaxy at which the kinetic energy of an ICM's particle ($\sim \frac{1}{2}v_{\rm gal}^2$) equals its dynamical energy ($\sim G\frac{M_{\rm gal}}{R}$, where R is the distance of the particle from the centre of the galactic potential). Therefore, particles that are inside the sphere centered on the galaxy and with a radius equal to R_A are the ones that are severely affected by the gravitational attraction of the galaxy, and are deflected into the wake. The accretion radius is large in this system: for a massive elliptical galaxy moving at ~ 300 km s^{-1}, the accretion radius is $R_A \sim 100$ kpc, which is larger than the physical extent of the galaxy itself. Analysis of the optical image of the field around 4C 34.16 (Sakelliou et al. 1996) shows that the effective radius of the galaxy that hosts the radio source is ~30 kpc. For such a system in which a small accretor moves subsonically through gas, the gas flow is dictated by the gravitational attraction of the accretor and the relative motion between the accretor and the medium. Thus, a simple ballistic model provides a good approximation for estimating the properties of the wake associated with 4C 34.16. In such a model the overdensity Δn at a distance b from the axis along which the galaxy is moving is given by:

$$\Delta n \approx \frac{2GM_{\rm gal}}{v_{\rm gal}^2\, b} n \qquad (5.1)$$

where n is the ambient gas density, and $M_{\rm gal}$ is the mass of the moving galaxy (Chandrasekhar 1943). Thus, if the overdensity of the wake is known, we can see if the estimate of the galaxy's velocity is consistent with a sensible value for its mass.

In order to calculate the density of the wake its temperature is needed. Unfortunately, the number of counts from the small region of the wake is not sufficient to constrain the full spectral fit. A simpler indication of the temperature is provided by the mean energy per photon. Calculating the mean energy for photons coming

from the wake ($E_{\rm wake}$) and for photons coming from the surrounding ICM ($E_{\rm ICM}$), it is found that $E_{\rm wake} = 1.08 \pm 0.09$ keV, and $E_{\rm ICM} = 1.03 \pm 0.03$ keV. These results indicate that the temperature of the wake is not very different from the temperature of the surrounding ICM, and so for the calculations that follow a value of 1 keV is adopted.

Assuming that the gas in the wake emits via thermal bremsstrahlung, its luminosity ($L_{\rm wake}$) is proportional to its density squared ($L_{\rm wake} \sim n^2_{\rm wake}\, T^{1/2}$). By choosing a rectangular source region within which the wake is located, and a background region from immediately outside the enhanced wake, the excess unabsorbed luminosity due to the wake in the rest frame of the source, $L_{\rm wake}$ can be calculated. This analysis yields $L_{\rm wake} = (1.2 \pm 0.4) \times 10^{42}$ erg s^{-1}, assuming a galactic $N_{\rm H}$ equal to the Stark et al. value. Consequently, the density of the wake is found to be $(1.6 \pm 0.3) \times 10^{-3}$ cm^{-3}, which exceeds the central density of the gas by $\Delta n = (0.8 \pm 0.3) \times 10^{-3}$ cm^{-3}.

As a characteristic value for the radius of the wake [b in eq. (5.1)], the half width at half maximum of the wake (~ 30 arcsec) is adopted. If the elliptical galaxy which hosts 4C 34.16 is moving at a speed of 300 km s^{-1}, which is an average value of the galaxy velocities found in §5.3, then eq. (5.1) implies that the elliptical galaxy must have a mass of $\sim 10^{12}$ M$_\odot$ in order to reproduce the observed wake overdensity. This value is consistent with what we would expect for a giant cluster elliptical, and so the observed properties of the wake do, indeed, seem consistent with what we would expect from this simple gravitational focussing model.

5.6 The lifetime of the wake

In the previous section it was suggested that the strange feature lying between the radio lobes of 4C 34.16 could be explained as the wake produced by the moving galaxy. Its density and temperature were calculated from the X-ray image and their values, when compared with the corresponding values for the density and temperature of the ICM indicate that the wake is over-pressured: the pressure inside the wake is $P = 2nkT = 5.12 \times 10^9$ dyn cm^{-2}, where n and T are the density and temperature of the wake, twice as much as the pressure of the surrounding ICM. The natural consequence of this fact is that such a structure is not stable, but it will expand until its pressure equals the pressure of the surrounding medium. As it expands its density drops. Since its luminosity mainly depends on the number density, it is clear that such an expansion will be accompanied by a rapid decrease of the surface brightness, and will lead to values comparable to the luminosity of the surrounding medium.

Then, the wake will not be a pronounced structure in the X-ray image, but will be diluted by the emission from the ICM. The question is how fast such a physical process takes place. If the structure discovered in the X-ray image of 4C 34.16 expands and disappears more rapidly than it is created, then either the simplistic ballistic model used in the previous section is not valid, or another explanation for this structure must be found.

In this section these questions are investigated by following the evolution of the over-dense wake. The aim is to find how fast the radius of the wake increases and to calculate its expansion velocity. If the X-ray structure associated with 4C 34.16 is indeed the wake of the moving galaxy, its creation rate is proportional to the galaxy velocity. Therefore, the expansion velocity must be found to be at most of the order of the galaxy's velocity.

The expansion of such a condensation into another medium is generally governed by the difference of pressures of the wake (P) and the ICM ($P_{\rm ICM}$), and is regulated by the conservation of energy. Consider a cylinder of radius R and length l representing the dense region occupied by the wake. As this cylinder is expanding, its outer shell of infinitesimal width, which is in contact with the ICM, is driven into the ICM by the net pressure acting on it. The change of the momentum of the shell is:

$$m_{\rm shell}\Delta v_{\rm exp} = (P - P_{\rm ICM})\ 2\pi R l\ \Delta t \tag{5.2}$$

where $m_{\rm shell}$ is the mass of the shell, and $v_{\rm exp}$ is the expansion velocity.

As the wake is expanding its internal energy ($E_{\rm int}$) is reduced. A fraction of it is radiated away via thermal bremsstrahlung and another fraction is consumed to drive the outer shell into the ICM:

$$\Delta E_{\rm int} = \Delta\left(\frac{3}{2}PV\right) = L_X\Delta t + P\Delta V \tag{5.3}$$

where V and L_X are the volume and the luminosity of the wake, and both vary with time. During the expansion, the temperature of the wake also changes according to the ideal gas law:

$$\frac{PV}{T} = const. \tag{5.4}$$

The last three equations, the conservations of momentum [eq. (5.2)] and energy [eq. (5.3)], and the ideal gas law [eq. (5.4)] are always valid during the expansion of the wake. In order to solve this problem and calculate the change of the parameters of interest with the lapse of time, a numerical simulation was performed. The radius

of the wake was allowed to change by a small amount during a small time interval. At the end of this time step the new values of the radius, pressure, and temperature were calculated and used as initial conditions for the next step. The time step was chosen such that the radius of the wake increased by an amount of less than 5% its initial value. Such a calculation assumes that at the beginning and end of each time interval the density in the wake is uniform and that the pressure and temperature remain constant inside the volume of the wake.

If at a time $t_{\rm n}$ the radius, pressure, and density of the wake are $R_{\rm n}$, $P_{\rm n}$, and $n_{\rm n}$ respectively, the radius $R_{\rm n+1}$ at $t_{\rm n} + \Delta t$ can be calculated :

$$\left(\frac{R_{\rm n+1}}{R_{\rm n}}\right)^3 - \left(\frac{R_{\rm n+1}}{R_{\rm n}}\right)^2 - \left(\frac{R_{\rm n+1}}{R_{\rm n}}\right) + 1 = \frac{2(P_{\rm n} - P_{\rm ICM})\Delta t^2}{R_{\rm n}^2 \mu m_{\rm p} n_{\rm n}} \tag{5.5}$$

This equation was derived from eq. (5.2) after substituting the mass of the shell by:

$$m_{\rm shell} = \mu m_{\rm p} n_{\rm n} (V_{\rm n+1} - V_{\rm n}) \tag{5.6}$$

where $V_i = \pi R_i^2 l$. The expansion velocity $v_{\rm exp}$ in eq. (5.2) was written as:

$$\Delta v_{\rm exp} = \frac{R_{\rm n+1} - R_{\rm n}}{\Delta t} \tag{5.7}$$

Having calculated the radius $R_{\rm n+1}$ the pressure inside the wake at $t_{\rm n+1}$ can be found using eq. (5.3), which becomes:

$$\frac{3}{2} P_{\rm n+1} V_{\rm n} - 2 P_{\rm n} V_{\rm n} + \frac{1}{2} P_{\rm n} V_{\rm n+1} - L_{X,{\rm n}} \Delta t = 0 \tag{5.8}$$

The luminosity of the wake at time $t_{\rm n}$ ($L_{X,{\rm n}}$) is calculated by integrating the volume emissivity over the volume of the wake at the time $t_{\rm n}$:

$$L_{\rm n} = 6.8 \times 10^{-38} \, \frac{k}{h} \, g_{\rm B} \, T_{\rm n}^{1/2} \int n_{\rm n}^2 dV \tag{5.9}$$

where k the Boltzmann constant, h the Planck constant, and $g_{\rm B}$ the Gaunt factor. The integration of eq. (5.9) gives:

$$L_{X,{\rm n}} = C \, T_{\rm n}^{1/2} \, R_{\rm n}^{-2} \tag{5.10}$$

where $C = 4.83 \times 10^{83}$ (cgs units). Finally, the temperature of the wake at $t_{\rm n+1}$ is

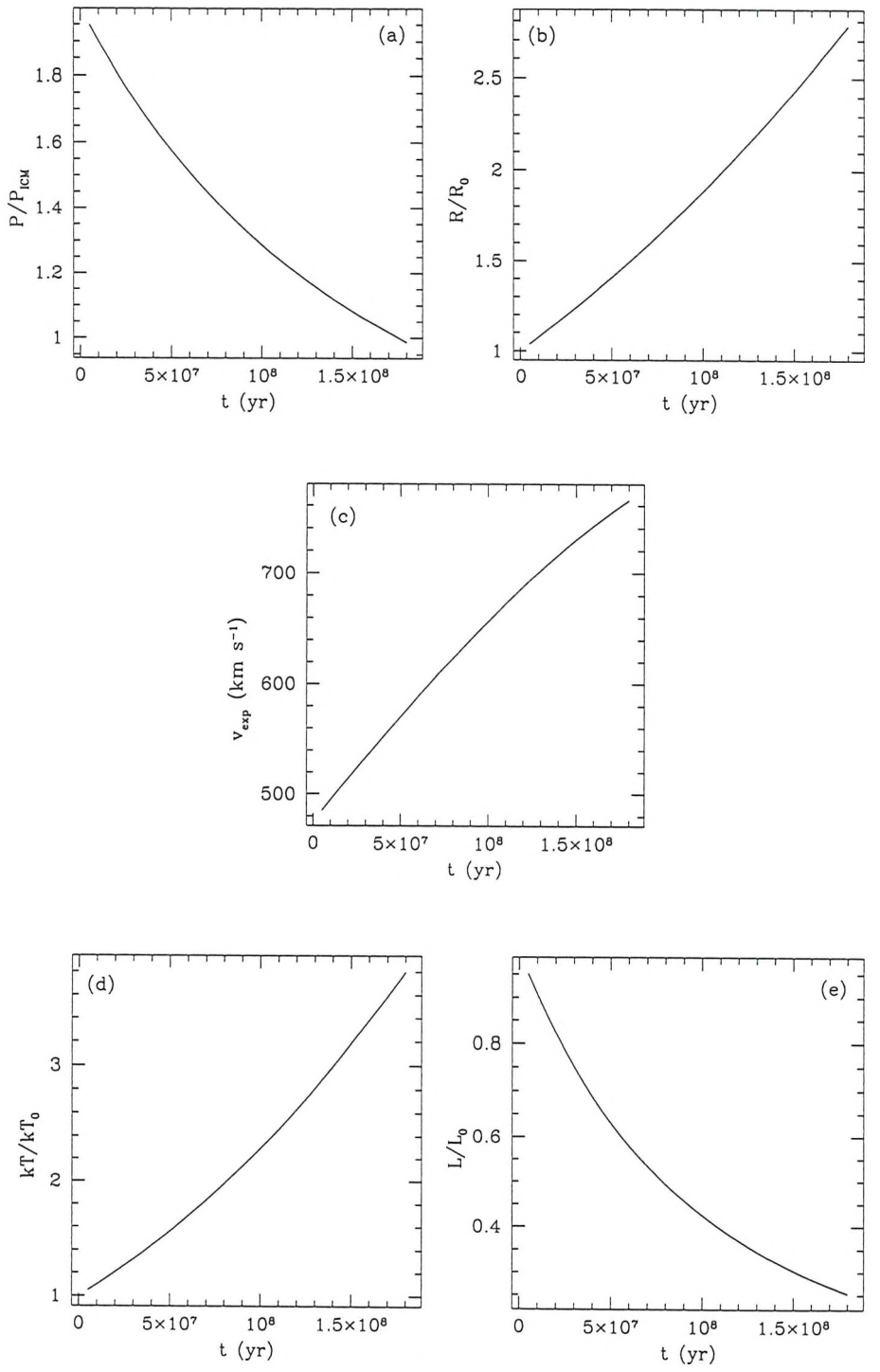

Figure 5.7: Time evolution of the parameters of the X-ray wake: (a) the pressure (P) relative to the pressure of the surrounding medium ($P_{\rm ICM}$), (b) the radius (R) relative to the initial radius (R_0), (c) the expansion velocity ($v_{\rm exp}$), (d) the temperature (kT) relative to the initial kT_0, and the luminosity (L_X) relative to the initial value ($L_{X,0}$).

calculated from eq. (5.4):

$$T_{n+1} = \frac{T_n}{P_n V_n} P_{n+1} V_{n+1} \tag{5.11}$$

The time evolution of the properties of the wake was calculated as described above. As initial values for the radius R_0, density n_0 and temperature kT_0 the values found from the X-ray data in §5.6 were used. The results are presented in Fig. 5.7.

According to Fig. 5.7(c), the expansion velocity varies between $500 - 800$ km s^{-1}, which is slightly higher than the galaxy velocity found in §5.3. The radius of the wake [Fig. 5.7(b)] will become double its initial value after 1.1×10^8 yr. At that time the luminosity of the wake will have decreased to 40% its observed value at the present time. If the galaxy continues to travel at the constant velocity of 300 km s^{-1}, at the same time it will have traveled a distance equal to $0.51 R_0$, and a new part of the wake will have been created. It is therefore reasonable that a galaxy which moves at the velocity of 4C 34.16 through the ICM of a similar cluster could sustain a wake visible in the X-ray images.

The same calculations were also performed for an adiabatic expansion, setting the energy loss by radiation to zero. The results are not different from the ones presented here, indicating that radiation losses are not important, and the dynamics of the wake can be described by an adiabatic expansion.

The model that has been presented in this section does not fully describe the dynamics of the wake, since it does not take into account its continuous replenishment with new material deflected by the moving galaxy. The consequences of such a continuous accretion will be: (i) extra confinement of the wake, since the external pressure must be larger than the thermal pressure of the ICM by an amount proportional to the momentum of the deflected particles, and (ii) the pressure inside the wake also increases, since its density increases. The results of such a treatment of the wake's dynamics cannot be easily predicted, and detailed numerical simulations are needed.

5.7 Summary

ROSAT PSPC observations of the field which contains the WAT source 4C 34.16 have been presented. In the radio maps, 4C 34.16 appears as a very symmetric bent radio galaxy. Its jets exhibit a double bend with their ends directed away from the peak of the X-ray emission. The spectral analysis of the X-ray data indicates that the gas around 4C 34.16 is relatively cool, although it is difficult to assess the exact temperature due to the apparent excess of absorption by cool atomic gas implied by

the fits. The results of the spatial and spectral analysis are summarized in Table 5.1.

Analysis of the X-ray data revealed substantial substructure in the gas, strongly reminiscent of the images simulated by Roettinger et al. (1993) and Schindler & Müller (1993) for merging clusters of galaxies. In particular, the X-ray emission is elongated; the X-ray image revealed a faint outer ring of emission, which could be the 'lens-shaped' shock front pointed out by Schindler & Müller (1993) and Schindler (1995), generated after the collision of two clusters of galaxies; and there is a wake which can be explained as arising from the gravitational focussing of the ICM by the motions of the central galaxy. The large core radius of the X-ray emission is also unusual for a poor cluster dominated by a single central galaxy, but is expected in a system which has undergone a recent merger.

These features provide evidence for significant dynamical activity in the ICM around 4C 34.16, perhaps due to a recent merger event. We would not expect such an event to be as dramatic and violent as a collision between richer clusters, and it is more likely in this case that we are witnessing the infall of a cloud of gas into a poor group. Such an infall of relatively cool, possibly primordial, gas has already been mooted as the cause of the substructure seen in Abell 548 (Davis et al. 1995) and Abell 2597 (Sarazin et al. 1995). This result is in agreement with the main conclusion of chapter 2, that WATs indicate the site where a recent merger event has occurred. However, more investigation is required, focussed on WATs in poor environments, in order to confirm that we are observing the same process as in richer clusters.

The combination of ram pressure and buoyancy provides a credible explanation for the double bend in the jets in 4C 34.16. By using the X-ray data to measure the properties of the ICM which cause these bends, strong constraints can be set on the remaining unknown quantities, such as the galaxy and jet velocities. By looking just at the point where buoyancy and ram pressure forces balance, a strong upper limit on the velocity of the galaxy was obtained. This limit implies that the galaxy is moving at ≤ 300 km s^{-1}. Such a relative velocity between the galaxy and the ICM might reasonably be induced in the minor cluster merger scenario that has been discussed above. As for 3C 465 (chapter 4) the derived velocity of the kiloparsec-scale jets is restricted to low values. It has also been shown that a large elliptical galaxy moving at such velocities would induce the wake-like density enhancement in the ICM that we observe.

Chapter 6

Epilogue

The study of the physical processes in clusters of galaxies presented in the previous chapters has shown different aspects of the interactions between the galaxies and the hot ICM. As galaxies move through the ICM, their interstellar media may be removed via ram pressure stripping, and wakes may be formed behind them tracing their direction of motion. If they happen to be radio galaxies, the nature and properties of their jets might change as, for instance, they cross the ISM/ICM interface, and they can lose their well collimated shape, appearing as bent jets.

The results of this thesis can be used to gain more insight into the related physical processes, and to investigate the dynamics of clusters of galaxies. For example, the direction in which the jets of WAT radio sources are bent has successfully been used in Chapter 2 to uncover their preferred orbits in clusters. On that basis, it was suggested that WATs are those radio galaxies which happen to be captured by forming clusters, and at the present time are falling towards their centres. Given the limited sensitivity of X-ray observations relative to radio observations, WATs can be used to identify the sites of merging clusters, without having to resort to deep X-ray or optical observations.

Another tool for the study of cluster dynamics is X-ray wakes. Wakes, similar to the one discovered associated with 4C 34.16 in Chapter 5, are expected to exist behind every moving galaxy in a cluster. As shown by Merrifield (1998), the directions of galactic wakes revealed by X-ray observations combined with redshift observations can be used to calculate the gravitational potential of clusters of galaxies.

The structure and properties (density and temperature) of wakes must depend on the velocity of the associated galaxies. Future observations with the *AXAF* and *XMM* satellites will provide us with high quality images and spectra of these features, which will help us to accurately define their shapes and characteristics. These obser-

vational results combined with theoretical predictions will permit the calculation of the 3-dimensional galaxy velocity. This achievement will be a step towards a better understanding of the way that galaxies move in clusters. At the moment we only can derive the line-of-sight galaxy velocity from redshift measurements and there is no way of calculating the component of the galaxy velocity on the plane of the sky.

The analysis of the X-ray emission from the early-type galaxies in Abell 2634 revealed that this emission is due to the stellar population of the galaxies, suggesting that they are depleted of their interstellar media. In this cluster, stripping mechanisms seem to dominate the replenishment mechanisms which add gas onto the cluster galaxies. By performing the analysis of chapter 3 for clusters of different richness, it will be possible to better understand the results of ram pressure and tidal stripping, and define how their effectiveness depends on the properties of the clusters.

In chapter 4 an effort was made to explain observationally the sudden flaring of radio jets. It was shown that if we want to reach firm conclusions X-ray data of high spatial and especially spectral resolution are required, which will be achieved with observations obtained by the new satellites *AXAF* and *XMM*.

Finally, the survey of WAT sources in clusters of galaxies presented in chapter 2 has given rise to a question concerning the evolution of radio galaxies: are WATs a transient phase in the evolution of radio galaxies of FRIIs to FRIs? Since the large-scale bending in WATs seems to be produced while they are falling towards the centres of clusters, it is probable that their jets were straight before being captured by the cluster. It was also found in chapter 2 that the galaxies which host WATs will soon settle at the centres of clusters, and that there is a high probability that their jets will lose their well defined shape. In Table 6.1 the properties of FRIIs, WATs, and

Table 6.1: PROPERTIES OF RADIO GALAXIES

	FRII	WATs	FRI
Radio Luminosity (W Hz^{-1})	$> 10^{25}$	$\sim 10^{25}$	$< 10^{25}$
Jet velocity	$\sim c$	$\sim c$ near the galaxy, $(10^3 - 10^4)$ km s^{-1} on larger scales	$(10^3 - 10^4)$ km s^{-1}
Environment	poor	falling into rich clusters	rich
Space density	more at high z	?	more at low z

FRIs are compared. In order to establish a connection between these different types of radio galaxies, and uncover the role of WATs in a generalized picture of the radio galaxy phenomenon, several lines of enquiry must be pursued: i) calculation of the space density of WATs and its evolution with redshift; in such a scenario, the number density of WATs is expected to decline with redshift. ii) theoretical and observational investigation of how radio jets decelerate; it is during the WAT phase that the jets decelerate from relativistic to subrelativistic velocities.

Appendix A

Cluster's gravitational potential - ICM distribution

A.1 The isothermal model

The motion of a fluid in a gravitational potential Φ is described by the Euler's equation:

$$\frac{\partial \boldsymbol{v}}{\partial t} + (\boldsymbol{v} \cdot \nabla)\boldsymbol{v} = -\frac{1}{\rho}\nabla P - \nabla\Phi \tag{A.1}$$

where P is the thermal pressure of the fluid, ρ its density, and $\boldsymbol{v}$ its velocity. Commonly, the ICM of a cluster of galaxies is treated as being in hydrostatic equilibrium, which means that it sits in the gravitational potential of the cluster, supported by its own thermal pressure. Equation (A.1) for the case of hydrostatic equilibrium becomes:

$$0 = -\frac{1}{\rho}\nabla P - \nabla\Phi \tag{A.2}$$

Additionally, if it is assumed that the gas is isothermal, its thermal pressure ($P_{\rm gas}$) is given by:

$$P_{\rm gas} = n_{\rm gas} k T_{\rm gas} = \frac{\rho_{\rm gas} k T_{\rm gas}}{\mu m_p} \tag{A.3}$$

where $n_{\rm gas}$, $\rho_{\rm gas} = \mu m_p n_{\rm gas}$, and $T_{\rm gas}$ are the number density, the density in gr cm^{-3}, and the temperature of the ICM, μ the mean molecular weight, and m_p the proton mass. Substituting the pressure P in (A.2) by the thermal pressure of the gas given by (A.3), the gravitational acceleration of the cluster is found to be:

$$g = \nabla\Phi = -\frac{k T_{\rm gas}}{\mu m_p}\frac{\nabla \rho_{\rm gas}}{\rho_{\rm gas}} \tag{A.4}$$

The galaxies in the cluster experience the same gravitational drag, and if it is assumed that they are in hydrostatic equilibrium, equation (A.2) is also valid for their distribution. For an isothermal distribution, the pressure of the galaxy 'gas' is:

$$P_{\rm gal} = n_{\rm gal} k T_{\rm gal} = \frac{1}{3}\rho_{\rm gal} < v^2 > \tag{A.5}$$

where $< v^2 >$ is the mean square velocity dispersion. Substituting (A.5) in (A.2) :

$$\nabla\Phi = -\frac{< v^2 >}{3}\frac{\nabla\rho_{\rm gal}}{\rho_{\rm gal}} \tag{A.6}$$

Finally, equating (A.4) and (A.6) and assuming spherical symmetry:

$$\frac{< v^2 >}{3}\frac{1}{\rho_{\rm gal}}\frac{d\rho_{\rm gal}}{dr} = \frac{kT_{\rm gas}}{\mu m_{\rm p}}\frac{1}{\rho_{\rm gas}}\frac{d\rho_{\rm gas}}{dr}$$

$$\frac{\mu m_p < v^2 >}{3kT_{\rm gas}} \ln\left[\frac{\rho_{\rm gal}(r)}{\rho_{\rm gal}(0)}\right] = \ln\left[\frac{\rho_{\rm gas}(r)}{\rho_{\rm gas}(0)}\right]$$

$$\frac{\rho_{\rm gas}(r)}{\rho_{\rm gas}(0)} = \left[\frac{\rho_{\rm gal}(r)}{\rho_{\rm gal}(0)}\right]^{\beta} \tag{A.7}$$

The so-called β-factor appearing in (A.7) is the ratio of the energy density per unit mass stored in the galaxies to the energy density per unit mass in the gas:

$$\beta = \frac{\mu m_p < v^2 >}{3kT_{\rm gas}} = \frac{\mu m_{\rm p}\sigma_{\rm r}^2}{kT_{\rm gas}} = \left(\frac{\sigma_{\rm r}}{\sqrt{\frac{kT_{\rm gas}}{\mu m_p}}}\right)^2 \tag{A.8}$$

where $\sigma_{\rm r}$ is the line-of-sight velocity dispersion.

The observed galaxy distribution is well described by King's approximation to a self-gravitating isothermal sphere. In such a model the galaxy density at a distance r from the centre of the cluster is approximated by:

$$\rho_{\rm gal}(r) = \rho_{\rm gal}(0)\left[1 + \left(\frac{r}{r_{\rm c}}\right)^2\right]^{-3/2} \tag{A.9}$$

where $\rho_{\rm gal}(0)$ is the central galaxy density, and $r_{\rm c}$ defines the core radius of the distribution (Sarazin 1988).

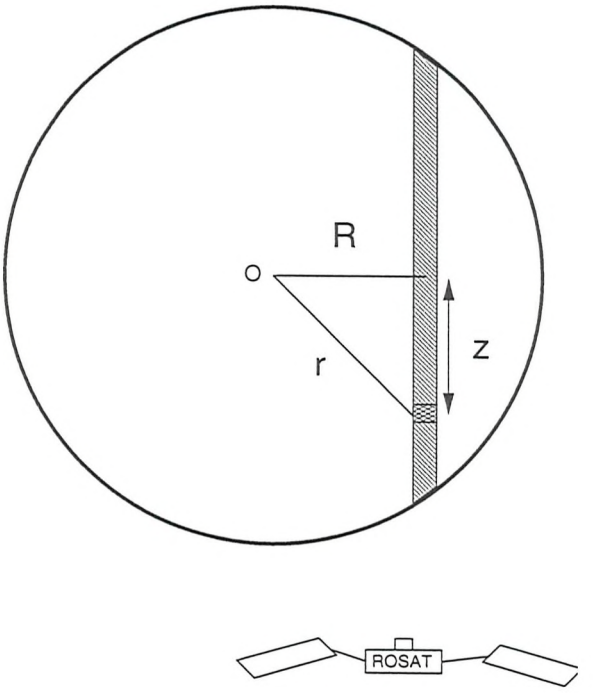

Figure A.1: Diagram of a spherically symmetric cluster of galaxies used to derive the surface brightness distribution of the X-ray emission from the ICM. The emission at a distance R from the cluster centre O received by the detector is the integrated emission along the marked column.

From equations (A.7) and (A.9) the density distribution of the ICM is obtained:

$$\rho_{\rm gas}(r) = \rho_{\rm gas}(0)\left[1+\left(\frac{r}{r_{\rm c}}\right)^2\right]^{-3\beta/2} \qquad \text{(A.10)}$$

References to the β-model include Cavaliere & Fusco-Femiano (1976), Sarazin & Bahcall (1977), Gorenstein et al. (1978), Fabricant & Gorenstein (1983), Forman, Jones & Tucker (1985), Trinchieri, Fabbiano & Canizares (1986), Killeen & Bicknell (1988).

A.2 Surface brightness distribution

Assuming that the ICM is distributed according to (A.10). The gas emits isotropically in the X-rays via thermal bremsstrahlung. The surface brightness at a distance R from the cluster centre recorded by the X-ray detectors is the integrated bremsstrahlung

emissivity along a column (Fig. A.1) :

$$\Sigma(R) = C \int n_{\rm gas}^2(r)\, dz \tag{A.11}$$

The constant C is given by:

$$C = 1.42 \times 10^{-27} g T_{\rm gas}^{1/2} (e^{-E_1/kT_{\rm gas}} - e^{-E_2/kT_{\rm gas}}),\ {\rm erg\ s^{-1}\ cm^3} \tag{A.12}$$

where g is the integrated Gaunt factor, and $E_1 - E_2$ is the energy band through which the ICM is viewed, for example the energy range covered by the *ROSAT* PSPC. According to Fig A.1:

$$r^2 = R^2 + z^2 \Leftrightarrow dz = \frac{rdr}{\sqrt{r^2 - R^2}} \tag{A.13}$$

and A.11 becomes:

$$\Sigma(R) = 2C \int_{r=R}^{\infty} n_{\rm gas}^2(r)\, \frac{rdr}{\sqrt{r^2 - R^2}} \tag{A.14}$$

Substituting the density distribution of the ICM by (A.10) and integrating over r, the surface brightness distribution is found to obey:

$$\Sigma(R) = \Sigma(0) \left[1 + \left(\frac{R}{r_c}\right)^2\right]^{-3\beta+1/2} \tag{A.15}$$

The central surface brightness is found to be:

$$\Sigma(0) = \frac{C r_c}{n_{\rm gas}^2(0)} \frac{\Gamma(3\beta - 1/2)\ \Gamma(1/2)}{\Gamma(3\beta)} \tag{A.16}$$

where Γ is the complete gamma function, and its values for a range of arguments are given in tables.

Equation (A.15) is the model that is extensively used to fit the X-ray emission from clusters of galaxies. After having determined the central surface brightness $\Sigma(0)$ from the observations, and knowing the temperature of the ICM, which is necessary to calculate the constant C, equation A.16 is used to obtain the value of the central number density $n_{\rm gas}$.

Appendix B

Euler's equation in intrinsic coordinates

The equation of motion of a volume element in a fluid is:

$$\rho \frac{d\boldsymbol{v}}{dt} = \boldsymbol{F} \tag{B.1}$$

where ρ is the density of the fluid, $d\boldsymbol{v}/dt$ the acceleration, and $\boldsymbol{F}$ the total force that acts on the unit volume of the fluid. The acceleration that appears in eq. (B.1). denotes not only the change of the fluid velocity at a fixed point in space, but also the change of the velocity of a given fluid particle as it moves in space. The derivative $d\boldsymbol{v}/dt$ can be separated into two terms (Landau & Liftshitz 1959), where each one expresses one of these two changes :

$$\frac{d\boldsymbol{v}}{dt} = \frac{\partial \boldsymbol{v}}{\partial t} + (\boldsymbol{v} \cdot \nabla)\boldsymbol{v} \tag{B.2}$$

Substituting (B.2) in (B.1), the equation of motion takes the traditional form of Euler's equation:

$$\frac{\partial \boldsymbol{v}}{\partial t} + (\boldsymbol{v} \cdot \nabla)\boldsymbol{v} = \frac{1}{\rho}\boldsymbol{F} \tag{B.3}$$

In order to simplify eq. (B.3) and model the bending of jets in radio galaxies, several investigators (e.g., Kellermann & Owen 1988) in the past have assumed that:

$$\frac{\partial \boldsymbol{v}}{\partial t} = 0, \text{ and } (\boldsymbol{v} \cdot \nabla)\boldsymbol{v} \simeq \frac{v^2}{R} \tag{B.4}$$

where R is the scale length over the jet bends, or the radius of curvature.

A similar but more accurate result can be obtained by resolving Euler's equation

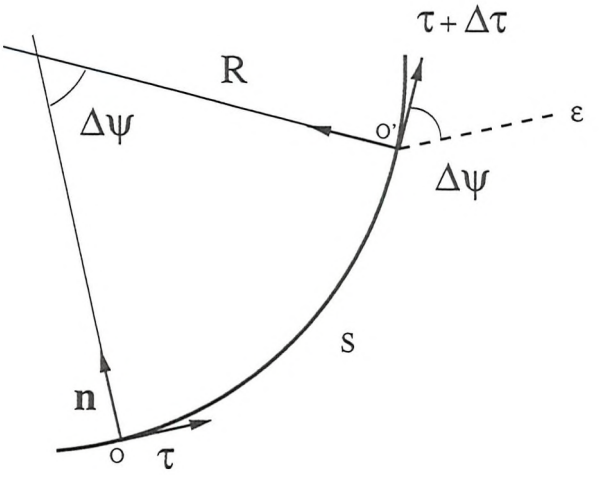

Figure B.1: Schematic diagram of the intrinsic coordinate system into which Euler's equation is resolved. At the position O, $\boldsymbol{\tau}$ and $\boldsymbol{n}$ are the unit vectors parallel and perpendicular to the flow. At O' the parallel vector has become $\boldsymbol{\tau} + \Delta\boldsymbol{\tau}$. The line ϵ is parallel to the vector $\boldsymbol{\tau}$.

into 'intrinsic' (or 'natural') coordinates. Such a system is defined by two axes which always lie parallel and perpendicular to the flow stream (the jet in this case). In Fig. B.1, $\boldsymbol{\tau}$ is the unit vector along the parallel direction, while the unit vector $\boldsymbol{n}$ indicates the perpendicular direction. The velocity of the volume element of the fluid at the position O is:

$$\boldsymbol{v} = v\ \boldsymbol{\tau} \tag{B.5}$$

and its acceleration:

$$\frac{d\boldsymbol{v}}{dt} = \frac{dv}{dt}\boldsymbol{\tau} + v\frac{d\boldsymbol{\tau}}{dt} \tag{B.6}$$

Assume that a volume element travels a distance s along the trajectory, going from O to O', where the system of coordinates has changed orientation. For small angles $\Delta\psi$, the change of the unit vector $\boldsymbol{\tau}$ is $\Delta\boldsymbol{\tau} = \Delta\psi\ \boldsymbol{n}$, and $\Delta\psi = \Delta s/R$, where R is the radius of curvature. Thus:

$$\frac{d\boldsymbol{\tau}}{dt} = \frac{1}{R}\frac{ds}{dt}\boldsymbol{n} = \frac{v}{R}\boldsymbol{n} \tag{B.7}$$

Using this result, (B.6) becomes:

$$\frac{d\boldsymbol{v}}{dt} = \frac{dv}{dt}\boldsymbol{\tau} + \frac{v^2}{R}\boldsymbol{n} \tag{B.8}$$

Having resolved the derivative of the vector velocity of the fluid into the intrinsic

coordinates, the equation of motion given by eq. (B.1) takes the form:

$$\rho\left[\frac{dv}{dt}\boldsymbol{\tau}+\frac{v^2}{R}\boldsymbol{n}\right]=\boldsymbol{F}\cdot\boldsymbol{\tau}+\boldsymbol{F}\cdot\boldsymbol{n} \tag{B.9}$$

The perpendicular component is:

$$\frac{v^2}{R}=\frac{1}{\rho}F_{\mathrm{n}} \tag{B.10}$$

where $F_{\mathrm{n}}=\boldsymbol{F}\cdot\boldsymbol{n}$ is the component of the force perpendicular to the jet. Therefore, it is not necessary to assume that $\partial\ \boldsymbol{v}/\partial t=0$, and the term v^2/R is not equal to the force acting on the jet, as previously assumed, but only to its component perpendicular to the jet.

Appendix C

Projection of the jets

C.1 Projection of an angle

Our knowledge is limited and the models we construct to describe several physical phenomena are affected by the lack of information on the 3D structure of the sources considered, since everything is projected onto the plane of the sky. A simple example of this effect is presented in Fig C.1. The lines ε_1 and ε_2 define a plane which is at an angle α with the plane of the sky, on which ε_2 and ε_3 lie. Furthermore, ε_3 is the projection of ε_1 onto the plane of the sky. Only if the angle α between the two planes is known, the measurement of the angle ϕ could provide the real value of the angle χ formed by ε_1 and ε_2. In such a case the real angle x can be derived as follows:

In Fig. C.1, AB and BC are both perpendicular to the line ε_2, while AC is perpendicular to ε_3. Since the triangle ABC forms an angle at point B which is equal to the known angle α, it is valid that:

$$\cos\alpha = \frac{\mathrm{BC}}{\mathrm{AB}} \tag{C.1}$$

Using the triangles AOB and BOC, is it found that:

$$\tan\chi = \frac{\mathrm{AB}}{\mathrm{OB}}, \quad \text{and} \quad \tan\phi = \frac{\mathrm{BC}}{\mathrm{OB}} \tag{C.2}$$

The true value of x is obtained by combining equations (C.1) and (C.2):

$$\tan\chi = \frac{\tan\phi}{\cos\alpha} \tag{C.3}$$

where ϕ can be measured, since it lies on the plane of the sky. This equation gives

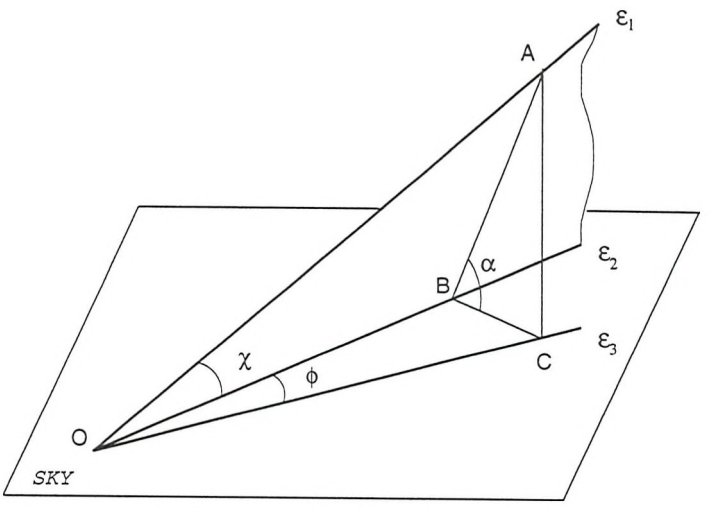

Figure C.1: Projection of an angle χ onto the plane of the sky which is defined by the lines ε_2 and ε_3. The line ε_3 is the projection of ε_1 onto the plane of the sky. AB and BC are both perpendicular to ε_2, while AC is perpendicular to ε_3.

that the projection of an angle $\chi = 90°$ is always $\phi = 90°$ independently from the value of α, as expected.

C.2 Equation of bent jets

In chapter 3 the shape of the radio jets as seen in the radio maps was used to calculate the velocity of the galaxy relative to the ICM, and the velocity of the material inside the jet. Such calculations involve the measurement of distances and angles from the available radio maps. Independent measurements suggest that the plane on which all these parameters of interest lie does not coincide with the plane of the sky, but that it is at some angle α. Such a geometry introduces projection effects to the measurements of distances and angles. However, knowing the angle α, these projection effects can be removed, and the correct distances and angles revealed.

In Fig. C.2 a schematic diagram of the problem considered in chapter 3 is presented, as it would be seen if $\alpha = 0°$. At the point A on the jet, the normal vector is $\hat{\boldsymbol{n}}$, and the line ε_1 indicates the direction tangential to the jet at that position. The cluster centre coincides with the point C. To solve the problems of chapter 3, the parameters that are needed are:

- the distance r of the point A from the cluster centre,
- the angle ϕ, which is the angle between the velocity of the galaxy ($\hat{\boldsymbol{v}}_{\rm gal}$) and the

normal to the jet ($\hat{\boldsymbol{n}}$), and

- the angle θ, which the angle between $\hat{\boldsymbol{n}}$ and $\nabla\rho_{\rm ICM}$, which is the gradient of the density distribution of the ICM and lies on the line that connects the cluster centre to the point A.

It is also argued that this plane is tilted around the line ε_2, which is parallel to the velocity of the galaxy. In this and the following sections the method to recover the actual values of the above parameters is presented.

Before the presentation of the calculations some general remarks must be made, in order to understand the reasons why this particular method is used to conduct them. The position of the point on the jet considered in each problem is not shifted along the jet after the projection. For example, the turn-over point is always the point where the curvature of the jet changes direction. Since the direction of curvature does not change with projection, the position of the turn-over point on the jet is always correctly found from the projected picture of the jet on the radio maps. For the same reason, the tangential line to the jet at that point is always correctly drawn. It is the normal to the jet that can not be found from the projected image. Therefore, the position of the point E on the line ε_3 is not known when $\hat{\boldsymbol{n}}$ is not on the plane of the sky.

C.2.1 The correct distance r

In the triangle ABC it is valid that:

$$r^2 = \mathrm{AB}^2 + \mathrm{BC}^2 \tag{C.4}$$

where BC, being parallel to the line ε_3 around which the plane is tilted, remains constant after the rotation. The real length of AB is:

$$\mathrm{AB}_{\rm real} = \frac{\mathrm{AB}_{\rm proj}}{\cos\alpha} \tag{C.5}$$

Combining (C.4) and (C.5) the real value of the distance r can be found, when the projected distance $\mathrm{AB}_{\rm proj}$ is measured from the radio maps.

C.2.2 The correct angle ϕ

As OA is perpendicular to AE the angle of interest is $90^\circ - \omega$. Attention must be given to the fact that the projected value of ϕ ($\phi_{\rm proj}$) is not equal to $90^\circ - \omega_{\rm proj}$, but

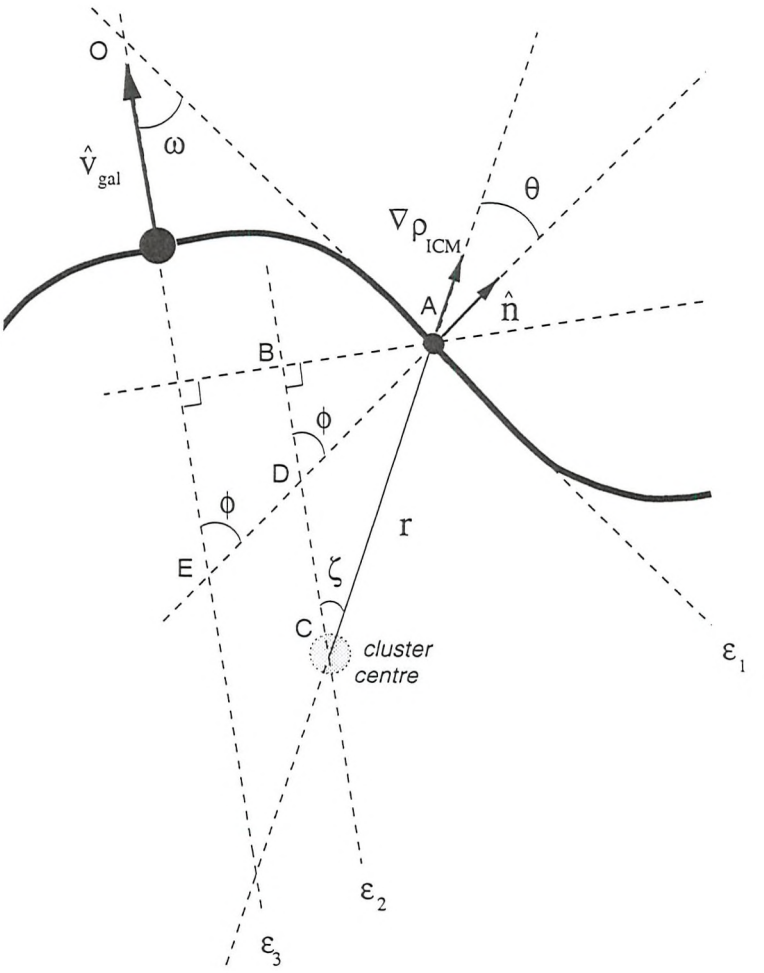

Figure C.2: Schematic diagram of the geometry used to calculate the galaxy and jet velocities.

only in the case that the whole system lies on the plane of the sky. Additionally, the projected value of ϕ can not be measured from the radio maps, since the line normal to the jet can not be drawn. The real value of ω is given by (C.3).

C.2.3 The correct angle θ

From the triangle ACD the wanted angle is equal to $180° - (180° - \phi) - \zeta$. The angle ϕ has been calculated in C.2.2, and ζ is transformed according to (C.3).

Appendix D

Notes on individual WATs

Abell 160: The X-ray structure of this cluster is irregular, showing distinctive condensations. From early *Einstein* observations these clumps of X-ray emission have been identified with emission from the cluster's galaxies. The *ROSAT* HRI image reveals the same situation. The definition of the X-ray centre is rather difficult, even after the removal of the bright point sources. The present data do not permit the calculation of the core radius, since the β-model does not provide a good fit to the surface brightness distribution of the ICM. Additionally, the jets of the radio galaxy are not severely bent, a fact that indicates the lack of a very dense ICM.

Abell 400: This cluster hosts the extraordinary radio source 3C 75, which consists of a dumbbell pair of radio galaxies. The jets of both radio galaxies are bent in the same direction, suggesting that they are both bent by the same cause. The interpretation of Balcells et al. (1995) that this source is the result of a merger of two different clusters, where each cluster hosted each radio galaxy does not look plausible. In such a scenario it is difficult to explain the bending of the jets in the same direction. This source is treated as one radio galaxy in the present survey.

Abell 562: This cluster is at a relatively high redshift ($z = 0.11$), the emission from the host galaxy is not pronounced, and is confused with the peak of the X-ray emission. For the definition of the cluster centre the emission from the galaxy is not subtracted.

Abell 569: The PSPC image is dominated by the emission from galaxies and point sources. The distribution of the cluster's ICM is not clearly revealed.

Abell 1446: The PSPC data reveal the regular appearance of this cluster. No point sources are removed for the definition of the cluster centre.

Abell 1552: This cluster lies behind the Virgo cluster. Therefore, its X-ray emission is contaminated by the emission from the ICM of the Virgo cluster [Fig. 2.5 (a)]. The

cluster centre reported here coincides with the position of the brightest galaxy of the cluster. This galaxy is also a radio galaxy, and the radio maps (Owen & Ledlow 1997) show that its jets are not distorted, which implies that the galaxy is not in motion relative to the ICM. An attempt to fit only the southern part of the cluster with the β-model yielded inconsistent results, and therefore, a measurement of the core radius can not be provided.

Abell 1763: The redshift of this cluster that has been extensively used (0.187; Struble & Rood 1991) was originally calculated using the redshift of only one galaxy (Noonan 1981). Recently, Owen, White & Thronson (1988) and Owen, Ledlow & Keel (1995) have measured the redshift of the galaxy that hosts the WAT and find it to be 0.2278, which is the value that is used here. The host galaxy possibly contributes to the total X-ray emission. However, the present data do not permit the separation of the different components contributing to the X-ray emission from the cluster. The cluster centre that is reported here is the peak of the X-ray emission.

Abell 1890: The X-ray emission from this relatively poor cluster appears to be clumpy in this short HRI observation.

Abell 2214: This cluster is clearly bimodal. Thus, a calculation of the cluster centre would be misleading. Both peaks are used for the definition of the cluster centre. However, the choice of a cluster centre does not influence much the value of the angle θ, since the position of the WAT is nearly aligned with both peaks.

Abell 2220: As it is clear from Fig. 2.5 (d) the definition of the cluster centre is difficult. Apart from a peak of X-ray emission that coincides with the galaxy that hosts the WAT there are two more peaks of the X-ray emission aligned. The position of the middle peak coincides with a big (non-active) galaxy which belongs to Abell 2220, while the eastern peak does not have any pronounced optical counterpart in the Palomar plates. For this reason, the middle peak is adopted as the cluster centre. Besides, this choice for the cluster centre does not influence the measurement of the angle θ, since both peaks are aligned with the position of the galaxy that hosts the WAT. Additionally, the present selection puts the WAT nearer to the cluster centre. The surface brightness distribution presented in Fig. 5.3 is obtained by counting photons around the cluster centre in concentric annuli excluding the X-ray emission from the east and west.

Abell 2304: The calculated cluster centre coincides with the peak of the X-ray emission.

Abell 2306: The X-ray image is clumpy. For the determination of the centre of the cluster only the central part of the image was used.

Abell 2462: The X-ray emission from the host galaxy is not subtracted.

Abell 2634: This cluster is studied in more details in chapters 3 and 4, where the *ROSAT* HRI and PSPC data are presented.

Abell 2637: There is no sign of X-ray emission coming from the cluster in the available X-ray image.

Appendix E

The *ROSAT* satellite

This thesis is based on the analysis of data obtained by the X-ray detectors (PSPC and HRI) on the *ROSAT* satellite. This Appendix describes the characteristics of the *ROSAT* satellite and its detectors. The discussion is restricted to those properties related to the analysis presented in the previous chapters. For instance, the timing capabilities of the X-ray detectors are not mentioned. Most of the information has been obtained by the *ROSAT* Users' Handbook (Briel et al. 1996) and from Fraser (1989).

E.1 General

The *ROSAT* satellite was launched on 1^{st} June 1990 into a low Earth orbit (initial altitude 580 km) with a period of 96 min. The word *ROSAT* is an abbreviation for the German word 'Röntgensatellit', after the Nobel prize winning physicist Röntgen, who discovered X-rays.

The scientific payload consists of the X-ray telescope (XRT), and the Wide Field Camera (WFC). The WFC covers the $0.05 - 0.21$ keV energy band, and it is of no concern here. The XRT covers the $0.12 - 2.4$ keV range, and a schematic diagram of it is shown in Fig. E.1.

Focusing systems for soft X-ray energies are based on the total external reflection of photons incident at small grazing angles, which are less than some critical angle. The critical angle depends on the composition of the reflecting material and decreases with increasing X-ray energy. A paraboloid of rotation (Fig. E.2) is the simplest focusing element for X-rays. With such mirrors, the image of a point source at infinity is a circle in the focal plane, whose radius is proportional to the off-axis angle of the source. Therefore, such a paraboloid cannot be used to form an image; nor can any

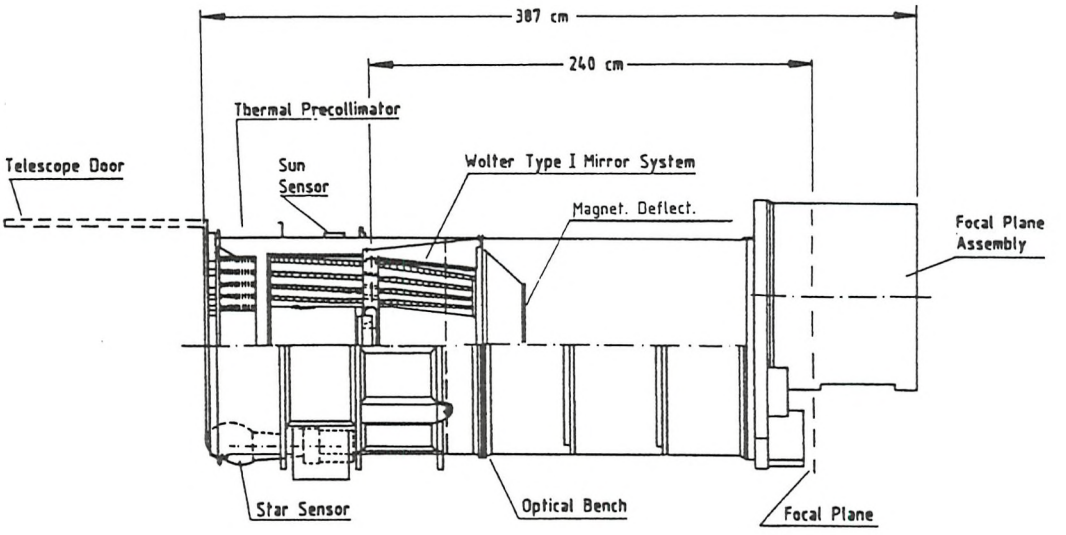

Figure E.1: Schematic cross-sectional view of the *ROSAT* telescope tube housing the fourfold nested 80 cm Wolter type I mirror system and the focal plane turret containing two PSPCs and one HRI.

single-reflection X-ray optic. Instead a configuration which permits a double-reflection of the X-ray photons is wanted, in order to achieve X-ray imaging.

On *ROSAT*, the focusing optics consist of four nested (coaxial) pair (Fig. E.2) of paraboloid-hyperboloid mirrors known as Wolter-I configuration (Fig. E.1), and is called the X-ray Mirror Assembly (XMA). The paraboloid and hyperboloid mirrors are confocal. Paraxial rays are reflected towards the common focus by the paraboloid and then by the hyperboloid towards its other focus.

Off-axis X-rays strike the mirror surface at a shallower angle such that the projected geometric area decreases. Furthermore, the average reflectivity of the mirror surface is reduced. In addition, off-axis X-rays suffer a higher degree of obstruction due to the radial struts which stabilize the XMA. Together these effects lead to an energy-dependent decrease of the effective area of the XRT as a function of the off-axis angle, known as 'vignetting'.

The focal plane instrumentation on *ROSAT* consists of a carousel on which there are two Position Sensitive Proportional Counters (PSPCs) and a High Resolution Imager (HRI).

The main aim of the *ROSAT* mission was a soft X-ray all-sky survey (RASS), which was completed in the first 6 months after launch. During this phase, the satellite scanned the sky continuously along circles perpendicular to the earth-sun direction.

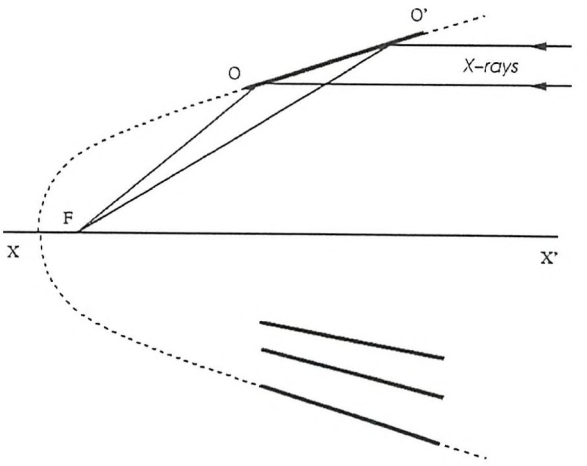

Figure E.2: Cross-section of a paraboloidal mirror OO'. The X-rays, incident parallel to the axis XX', are focused to the point F. The lower part of the image shows the nesting of paraboloid section, with the same focus.

In this way the ecliptic poles received up to 50 ksec exposures, while sky fields near the ecliptic plane were observed for some hundreds of seconds. No further all-sky survey is planned in the near future with missions like *AXAF* and *XMM*.

The survey was followed by the Pointed Observation Phases. Usually the observation times during these mission phases are much longer than during the survey.

E.2 The Position Sensitive Proportional Counter (PSPC)

The PSPC is a gas-filled multiwire counter. All X-ray proportional counters consist of a gas cell, subdivided into a number of low- and high-electric field regions by some arrangement of electrodes (Fig. E.3). The signals induced on these electrodes by the motions of electrons and ions in the gas contain information on the energies, arrival times and interaction positions of the photons entered the detector.

An X-ray photon, passing through the thin plastic entrance window of the proportional counter, will be photo-electrically absorbed by the gas producing a photo-electron. This electron is thermalized and in the process it causes the ionization of other gas atoms forming a secondary electron cloud, which begins to drift towards the nearest anode (A1 in Fig. E.3) under the influence of the applied electric field. The

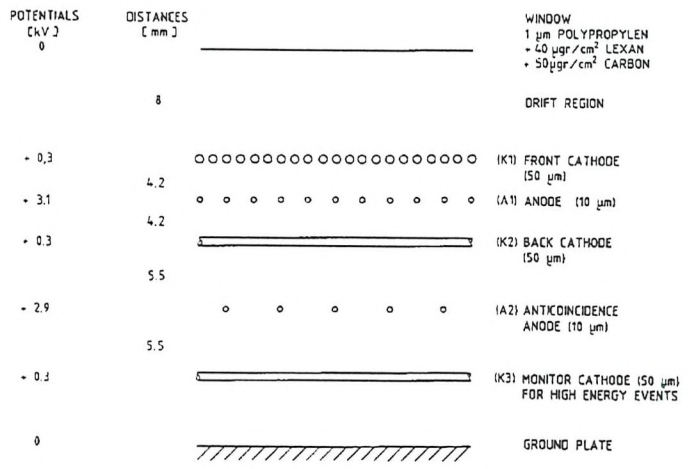

Figure E.3: Schematic cross-sectional view of a *ROSAT* PSPC. The mutually perpendicular cathode grids (K1 & K2) are gold-plated molybdenum wires with a 0.5 mm spacing used to determine the position of events. The A1 anode grid consists of gold-plated tungsten wires of 1 mm separation used to determine the energy of events. The A2 anode is of identical construction as A1 (except with a 2 mm wire separation) and used as an anti-coincidence counter. The filling gas is a mixture of 65% argon, 20% xenon and 15% methane.

number of electrons contained within the secondary electron cloud is approximately proportional to the energy of the incident photon. Once in a high-field region of the counter (close to the anode wire), electrons may gain sufficient energy between successive collisions to excite or ionize the molecules of the filling gas. The electrons released by collisional ionization themselves create further electron-positive ion pairs. Electron avalanches propagate towards the anode. Gas gains G (the number of electrons collected at the anode per electron in the X-ray induced charge cloud) of $10^3 - 10^5$ may be obtained in this manner. This gain is proportional to the applied anode voltage. The electrons induce a charge cloud onto the cathode grids (K1 and K2 in Fig. E.3), which consist of wires connected to independent preamplifiers. In this way the position of the event can be calculated. Anode A2 is the 'back veto counter' and senses background events originating from the central mounting plate of the PSPC, as well as charged particles passing the whole detector system, helping to efficiently rejecting the PSPC background.

The thin plastic entrance window of the *ROSAT* PSPC is supported by the well known 'wagon wheel' structure, which consists of a rigid circle with eight equally spaced radial struts. On smaller scales there are two wire mesh systems which can cause significant shadowing. In order to prevent this shadowing the telescope's point-

Table E.1: *ROSAT* PSPC and HRI Performance Summary

	PSPC	HRI
Field of view	2 degrees	38 arcmin
Spatial Resolution	25 arcsec	1.7 arcsec
Energy Resolution	27% FWHM at 1.5 keV	–
Quantum Efficiency (at 1 keV)	~50%	~30%
Background (counts arcmin^{-2} s^{-1})	$(4-32)\times10^{-4}$	3.8×10^{-3}

ing direction was slowly moving back and forth (wobble) by ~ 3 arcmin with a period of 400 sec diagonally to the wire mesh.

Two such detectors were initially in the focal plane of XRT (PSPC-B and PSPC-C). The PSPC-C was the primary detector, and was used for the RASS until its destruction during the Solar slew following a glitch of the *ROSAT* Attitude Measurement and Control system (AMCS) on 1991 January 25. The reserved PSPC-B has been used thereafter.

The energy resolution of a proportional counter depends on the gas mixture, the energy of the X-ray photons, the gain, and generally increases with increasing energy. Over the entire sensitive area of the *ROSAT* PSPC, its energy resolution is $\Delta E/E = 0.43(E/0.93)^{-0.5}$ (FWHM).

The spatial resolution of a proportional counter depends on fundamental gas physics, such as the diffusion of the electron cloud in the drift space of the counter, the X-ray penetration into the gas, and the readout technique. The combined XMA and PSPC position resolution is ~ 25 arcsec, and degrades with off-axis angle.

The detectability of X-ray sources depends on the background against which they are registered. In general for the *ROSAT* satellite, four components contribute to the background: instrumental background, background produced by the local space environment, usually charged particles, scattered solar radiation by atoms and molecules in the earth's atmosphere, and the diffuse celestial X-ray background due to galactic and extragalactic sources. The PSPC has essentially no internally produced background, because of the very efficient background rejection. Its total background is mainly due to: i) *charged particles* [$(2.5-30)\times10^{-5}$ counts arcmin^{-2} s^{-1}], ii) *scattered solar radiation* [$(0-8)\times10^{-4}$ counts arcmin^{-2} s^{-1}], and iii) *diffuse celestial radiation* [$(4.2-21)\times10^{-4}$ counts arcmin^{-2} s^{-1}].

The characteristics of the PSPC are summarized in Table E.1.

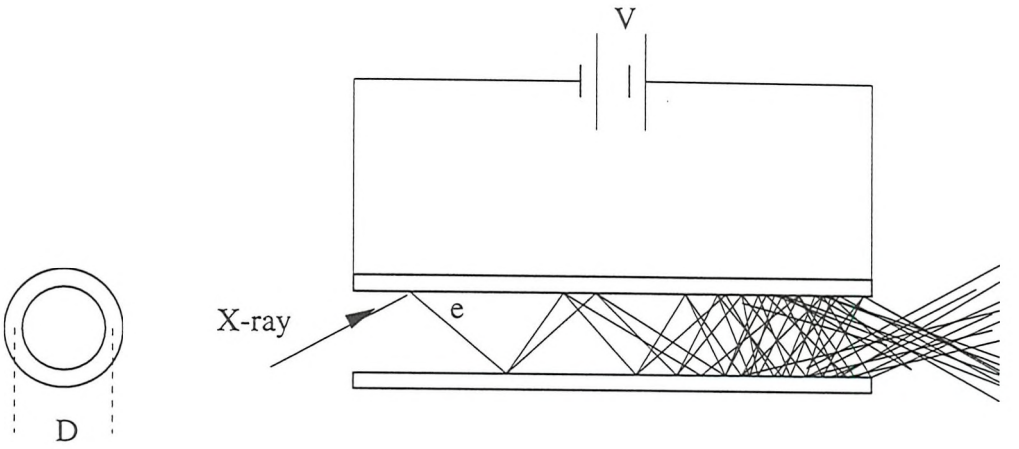

Figure E.4: Schematic cross-sectional of a continuous-dynode electron multiplier. The cross section of the channel is D.

E.3 The High Resolution Imager (HRI)

The *ROSAT* HRI is a position sensitive detector comprised of two cascade microchannel plates (MCPs), and is very similar to the HRI on the *Einstein* satellite. Its characteristics are presented in Table E.1.

A MCP is essentially an array of miniature photomultipliers. It typically consists of $\sim 10^7$ close-packed channels of common diameter D, which can be as small as ~ 2 μm. MCPs are therefore used in X-ray astronomy as in many other fields for distortionless imaging with very high spatial resolution. The principles of a channel electron multiplier are illustrated in Fig. E.4. X-rays incident at the low potential end of the multiplier release photoelectrons from its semiconducting surface. These photoelectrons are accelerated in vacuum by the applied electric field, strike the opposite wall of the multiplier and, provided the secondary electron emission coefficient of the surface is greater than one, release secondaries and initiate a cascade. $G > 10^8$ is the gain achieved. The gain and response of the MCPs to a specific energy range depends on the composition of the plates. In a microchannel detector (such as the *ROSAT* HRI) the microchannel plates are followed by a readout system (e.g., a cross-grid charge detector) which senses the output of each channel and encodes the position of each event.

The point spread function (PSF) describes the surface brightness distribution of point sources as registered by a detector. For the *ROSAT* HRI images, there are three components that contribute to the width of the PSF: the XRT PSF ($\sim$ 3 arcsec FWHM), the internal HRI PSF (1.7 arcsec FWHM), and a residual blurring

attributable to the aspect correction. Its functional form has been determined by fitting the azimuthally averaged surface brightness of known point sources. A good description for the on-axis PSF, which includes aspect solution effects, out to a radius of 2 arcmin is given by :

$$PSF(R) = A_1 e^{-0.5(\frac{R}{S_1})^2} + A_2 e^{-0.5(\frac{R}{S_2})^2} + A_3 e^{-\frac{R}{S_3}} \quad \text{(E.1)}$$

where A_1, A_2, A_3, S_1, S_2, and S_3 are constants with $A_1 = 0.96$, $A_2 = 0.18$, $A_3 = 0.001$, $S_1 = 2.19$, $S_2 = 4.04$, and $S_3 = 31.69$. R is the radial distance from the peak of the emission in arcsec. It has been found that for on-axis point sources approximately 15% of the total power is scattered beyond 10 arcsec, 7% beyond 1 arcmin, and less than 1% beyond 2 arcmin.

The off-axis PSF is dominated by the XRT PSF, and it becomes asymmetrical beyond 12 arcmin off-axis. An approximation to the azimuthally averaged off-axis PSF can be obtained by allowing the width of the larger Gaussian in eq. (E.1) to vary with off-axis angle θ:

$$S_2(\theta) = 3.3 + 0.19\theta - 0.016\theta^2 + 0.004\theta^3 \quad \text{(E.2)}$$

where θ is the distance from the centre of the image in arcmin.

The HRI was found to have a crude spectral sensitivity. However, the calibration of the HRI spectral response has not been completed, although softness ratios (counts in channels 1-5 divided by the counts in channels 6-11) seem the most sensitive energy indicators.

The total instrument's background given in Table E.1 consists mainly of three components: i) the *internal background* (1.5 counts s^{-1}), which mainly comes from residual radioactivity in the microchannel plates and the surrounding detector structure, ii) the *X-ray background* (1.0 counts s^{-1}), comprised of both galactic and extragalactic components and varies across the sky, and iii) the *externally induced background* (3.0 counts s^{-1}) from charged particles, earth scattered solar radiation, and auroral photons, which varies considerably during an orbit.

E.4 Known problems

E.4.1 Ghost Images

The position of an event in the PSPC is determined from the amplitudes of signals on the two cathode grids. For events with small pulse-height amplitudes, occasionally only one cathode segment grid will have a high enough signal. In this case the position of the event is incorrectly specified. This results in an extension of the images at energies below 0.15 keV.

E.4.2 Errors of the *ROSAT* attitude solution

Systematic discrepancies have been noted between the optical and X-ray positions of *ROSAT* targets. The 1σ scatter of the distribution of the optical versus X-ray positions has been found to be 6.1 arcsec for the PSPC and 6.4 arcsec for the HRI. Additionally the PSPC data showed a systematic offset of 6.9 arcsec, while the HRI showed negligible systematic offset. PSPC data distributed after December 1992 are corrected for the systematic offset. No correction is implemented for the random scatter, and it is thought that it is due to residual startracker errors. This offset can be different for observations of the same object taken at different times, and can result to a blurring of the imaged point sources and the broadening the PSF.

REFERENCES

Abell G. O., 1958, ApJS, 3, 211

Abell G. O., 1965, ARA&A, 3, 1

Abell G. O., 1975, in 'Stars and Stellar Systems IX: Galaxies and the Universe', eds., Sandage A., Sandage M., Kristian J. (University of Chicago, Chicago)

Abell G. O., Corwin H., Olowin R., 1989, ApJS, 70, 1

Arnaud K. A., Mushotzky R. F., Ezawa H., Fukazawa Y., Ohashi T., Bautz M. W., Crewe G. B., Gendreau K. C., Yamashita K., Kamata Y., Akimoto F., 1994, ApJL, 436, L67

Awaki H., Mushotzky R., Tsuru T., Fabian A. C., Fukazawa Y., Loewenstein M., Makishima K., Matsumoto H., Matsushita K., Mihara T., Ohashi T., Ricker G. R., Serlemitsos R. J., Tsusaka Y., Yamazaki T., 1994, PASJ, 46, L65

Baan W. A. McKee M. R., 1985, A&A, 143, 136

Bahcall N. A., 1977, ARA&A, 15, 505

Bahcall N. A., 1996, astro-ph/9611148

Balsara D., Livio M., O'Dea C. P., 1994, ApJ, 437, 83

Baldwin J. E., Scott P. F., 1973, MNRAS, 165, 259

Barnes J. E., Hernquist L. E., 1991, ApJL, 370, L65

Batuski D., Burns J. O., 1985, ApJ, 299, 5

Bautz L. P., Morgan W. W., 1970, ApJL, 162, 149

Bechtold J., Forman W., Giacconi R., Jones C., Schwarz J., Tucker W., Van Speybroeck L., 1983, ApJ, 265, 26

Beers T. C., Gebhardt K., Huchra J. P., Forman W., Jones C., Bothun G. D., 1992, ApJ, 400, 410

Beers T. C., Kriessler J. R., Bird C. M., Huchra J. P., 1995, AJ, 109, 874

Begelman M. C., Blandford R. D., Rees M. J., 1984, Rev. Mod. Physics, 56, 256

Begelman M. C., Rees M. J., Blandford R. D., 1979, Nature, 279, 770

Belcells M., Morganti R., Oosterloo T., Perez-Fournon I., Gonzalez-Serrano J. I., 1995, A&A, 302, 665

Bicknell G. V., 1994, ApJ, 422, 542

Bicknell G. V., 1995, ApJS, 101, 29

Bird C. M., 1993, PASP, 105, 1495

Bird C. M., 1994, AJ, 107, 1637

Biretta J., 1992, 'Astrophysical Jets'. eds. Burgarella D., Livio M., O'Dea, (Cambridge University Press)

Biretta J. A., Zhou F., Owen F. N., 1995, ApJ, 447, 582

Birkinshaw M., 1991, in 'Beams and Jets in Astrophysics', ed. Hughes P. A., (Cambridge University press)

Birkinshaw M., Laing R., Scheuer P., Simon A., 1978, MNRAS, 185, 39

Biviano A., 1997, astro-ph/9711251

Blandford R. D., 1990, in 'Active Galactic Nuclei', Saas-Fee Advanced Course 20, eds Courvoisier T. J.-L., Mayor M. (Springer-Verlag)

Bode P. W., Berrington R. C., Cohn H. N., Lugger P. M., 1994, ApJ, 433, 479

Blandford R. D., Rees M. J., 1974, MNRAS, 169, 395

Böhringer H., 1994, 'Cosmological Aspects of X-ray Clusters of Galaxies, ed. Seitter W. C., (Kluwer Publ.)

Böhringer H., 1995, 'Clusters of Galaxies', 17^{th} Texas Symposium on Relativistic Astrophysics and Cosmology, eds. Böhringer H., Trümper J., Morfill G. E., (The New York Academy of Sciences)

Böhringer H., Neumann D. M., Schindler S., Huchra J. P., 1997, ApJ, 485, 439

Bondi H., Hoyle F., 1944, MNRAS, 104, 273

Bradt H., Mayer W., Naranan S., Rappaport S., Spuda G., 1967, ApJL, 161, L1

Bremer M. N., Fabian A. C., Crawford C. S., 1997, MNRAS, 284, 213

Bridle A. H., Perley R.A., 1984, ARA&A, 22, 319

Briel U. G., Henry J. P., 1993, A&A, 278, 379

Briel U. G., Henry J. P., Böhringer H., 1992, A&A, 259, L31

Briel U. G., Henry J. P., Schwarz R. A., Böhringer H., Ebeling H., Edge A. C., Hartner G. D., Schindler S., Trumper J., Voges W., 1991, A&A, 246, 10

Briel et al. 1996, *ROSAT* User's Handbook

Brinkmann W., Siebert J., 1994, A&A, 285, 812

Brinkmann W., Siebert J., Boller Th., 1994, A&A, 281, 355

Burns J. O., 1981, MNRAS, 195, 523

Burns J. O., Balonek T. J., 1982, ApJ, 263, 546

Burns J. O., Gregory S. A., 1982, AJ, 87, 1245

Burns J. O., Owen F. N., 1979, AJ, 84, 1478

Burns J. O., Gregory S. A., Holman G. D., 1981, ApJ, 250, 450

Burns J. O., Gregory S. A., O'Dea C. P., Balonek T. J., 1986, ApJ, 307, 73

Burns J. O., Eilek J. A., Owen F. N., 1982, IAU Symposium 97: Extragalactic Radio Sources, p. 45

Burns J. O., O'Dea C. P., Gregory S. A., Balonek T. J., 1986, ApJ, 307, 73

Burns J. O., Rhee G., Owen F. N., Pinkney J., 1994, ApJ, 423, 94

Burns J. O., Pinkney J., Perley R. A., Owen F N., Voges W., 1995, ApJ, 446, 583

Butcher H. R., Oemler A. JR., 1985, ApJS, 57, 665
Byram E. T., Chubb T. A., Friedman H., 1966, Science, 152, 66
Canizares C. R., Blizzard P., 1991, ApJ, 382, 79
Canizares C .R., Donahue M. E., Trinchieri G., Stewart G. C., McGlynn T. A., 1986, ApJ, 304, 312
Canizares C. R., Fabbiano G., Trinchieri G., 1987, ApJ, 312, 503
Cavaliere A., Fusco-Femiano R., 1976, A&A, 49, 137
Chandrasekhar, S., 1943, ApJ, 97, 255
Ciotti L., D'Ercole A., Pellegrini S., Renzini A., 1991, ApJ, 376, 380
Cirimele G., Nesci R., Trevese D., 1997, ApJ, 475, 11
Colina L., de Juan L., 1995, ApJ, 448, 548
Cowie L. L., McKee C. F., 1975, A&A, 43, 337
Crawford C. S., Fabian A. C., 1993, MNRAS, 260, 15
Crawford C. S., Fabian A. C., 1995, MNRAS, 273, 827
Curtis H. D., 1918, Lick Obs. Publication, 13, 11
David L. P., Arnaud K. A., Forman W., Jones C., 1990, ApJ, 356, 32
David L. P., Forman W., Jones C., 1991, ApJ, 380, 39
David L. P., Jones C., Forman W., Daines S., 1994, ApJ, 428, 544
David L. P., Jones C., Forman W., 1995, ApJ, 445, 578
Davis D. S., White R. E., 1998, ApJ, 492, 57
Davis D. S., Bird C. M., Mushotzky R. F., Odewahn S. C., 1995, ApJ, 440, 48
De Young D. S., 1978, ApJ, 223, 47
De Young D. S., Condon J. J., Butcher H., 1980, ApJ, 242, 511
den Hartog R., Katgert P., 1996, MNRAS, 279, 349
Doe S. M., Ledlow M. J., Burns J. O., White R. A., 1995, AJ, 110, 46
Dressler A., 1980, ApJ, 236, 351
Dressler A., Shectman S. A., 1988, AJ, 95, 985
Ebeling H., Voges W., Böhringer H., Edge A. C., Huchra J. P., Briel U. G., MNRAS, 281, 799
Edge A. C., Stewart G. C., Fabian A. C., Arnaud K. A., 1990, MNRAS, 245, 559
Edge A. C., Stewart G. C., 1991, MNRAS, 252, 414
Edge A. C., Stewart G. C., Fabian A. C., 1992, MNRAS, 258, 177
Eilek J. A., Burns J. O., O'Dea C. P., Owen F. N., 1984, ApJ, 278, 37
Ellingson E., Green R. F., Yee H. K. C., 1991, ApJ, 378, 476
Evrard A. E., 1990, ApJ, 363, 349
Fabian A. C., 1994, ARA&A, 32, 277

Fabian A. C., Nulsen P. E. J., Canizares C. R., 1984, Nat, 310, 733
Fabbiano G., Trinchieri G., Elvis M., Miller L., Longair M., 1984, ApJ, 277, 115
Fabbiano G., Schweizer F., 1995, ApJ, 447, 572
Fabbiano G., Kim D.-W., Trinchieri G., 1992, ApJS, 80, 531
Fanaroff B. L., Riley J. M., 1974, MNRAS, 167, 31P
Fanti, C., Fanti, R., de Ruiter, H.R., Parma, P., 1987, A&AS, 69, 57
Feigelson E. D., Berg C. J., 1983, ApJ, 269, 400
Feretti L., Böhringer H., Giovannini G., Neumann D., 1997, A&A, 317, 432
Fitchett M. J., 1990, 'Clusters of Galaxies', eds. Oegerle W. R., Fitchett M. J., Danly L. (Cambridge University Press)
Forman W., Jones C., Tucker W., 1985, ApJ, 293, 102
Forman W., Schwarz J., Jones C., Liller W., Fabian A. C., 1979, ApJ, 234, L27
Frenk C. S., Evrard A. E., White S. D. M., Summers F. J., 1996, ApJ, 472, 460
Gallagher J. S., Ostriker J. P., 1972, AJ, 77, 288
Garijo A., Athanassoula E., García-Gómez C., 1997, A&A, 327, 930
Gioia I. M., Henry J. P., Maccacaro T., Stocke J. T., Wolter A., 1990, ApJ, 356, L35
Giovanelli R., Haynes M. P., Chincarini G. L., 1986, ApJ, 300, 77
Giovanelli R., Scodeggio M., Solanes J. M., Haynes M. P., Arce H., Sakai S., 1995, AJ, 109, 1451
Giovannini G., Feretti L., Gregorini L., 1987, A&AS, 69, 171
Giovannini G., Feretti L., Venturi T., Lara L., Marcaide J., Rioja M., Spangler S. R., Wehrle A. E., 1994, ApJ, 435, 116
Gómez P. L., Ledlow M. J., Burns J. O., Pinkney J., Hill J. M., 1997a, ApJ, 474, 580
Gómez P. L., Pinkney J., Burns J. O., Wang Q., Owen F. N., Voges W., 1997b, ApJ, 474, 580
Gopal-Krishna, Wiita P. J., 1987, MNRAS, 226, 531
Gorenstein P., Fabricant D., Topka K., Harnden F. R., Tucker W. H., 1978, ApJ, 224, 718
Gott J. R., Thuan T. X., 1976, ApJ, 204, 649
Grebenev S. A., Forman W., Jones C., Murray S., 1995, ApJ, 607
Gregory S. A., Burns J. O., 1982, ApJ, 255, 373
Gull S. F., Northover K. J. E., 1973, Nat, 244, 80
Gunn J. E., Gott J. R., 1972, ApJ, 176, 1
Gunn J. E., Gott J. R., 1972, ApJ, 176, 1
Henriksen M. J., Markevitch M. L., 1996, ApJ, 466, 79
Henry J. P., Briel U. G., 1995, ApJL, 443, 9

Henry J. P., Gioia I. M., Maccacaro T., Morris S. L., Stocke J. T., & Wolter A., 1992, ApJ, 386, 408

Hooda J. S., Wiita P. J., 1996, ApJ, 470, 211

Hunt R., 1971, MNRAS, 154, 141

Jenner D. C., 1974, ApJ, 191, 55

Jing Y. P., Mo H. J., Borner G., Fang L. Z., 1995, MNRAS, 276, 417

Johnstone R. M., Fabian A. C., Edge A. C., Thomas P. A., 1992, MNRAS, 255, 431

Jones C., Forman W., 1984, ApJ, 276, 38

Jones C., Stern C., Forman W., Breen J., David L., Tucker W., Franx M., 1997, 482, 143

Kaiser N., 1990, 'Clusters of Galaxies', eds. Oegerle W. R., Fitchett M. J., Danly L. (Cambridge University Press)

Kellermann K. I., Owen F. N., 1988, in 'Galactic and Extragalactic Radio Astronomy', eds., Verschuur G. L., Kellermann K. I. (Springer-Verlag)

Kent S. M., Gunn J. E., 1982, AJ, 87, 945

Kent S., Sargent W. L. W., 1983, AJ, 88, 697

King I., 1962, AJ, 67, 471

Kim D.-W., Fabbiano G., Trinchieri G., 1992a, ApJS, 80, 645

Kim D.-W., Fabbiano G., Trinchieri G., 1992b, ApJ, 393, 134

Kormendy J., Richstone D., 1995, ARA&A, 33, 581

Kormendy J., Bender R., Ajhar E. A., Dressler A., Faber S. M., Gebhardt K., Grillmair C., Lauer T. R., Richstone D., Tremaine S., 1996a ApJL, 473, 91

Kormendy J., Bender R., Ajhar E. A., Dressler A., Faber S. M., Gebhardt K., Grillmair C., Lauer T. R., Richstone D., Tremaine S., 1996b ApJL, 459, 57

Krempec-Krygier J. Krygier B., 1995, A&A, 296, 359

Kriss G. A., Cioffi D. F., Canizares C. R., 1983, ApJ, 272, 439

Lang K. R., 1980, in 'Astrophysical Formulae' (Springer-Verlag)

Lea S. M., De Young D. S., 1976, ApJ, 210, 647

Leahy J. P., 1984, MNRAS, 208, 323

Ledlow M. J., Owen F. N., 1995a, AJ, 109, 853

Ledlow M. J., Owen F. N., 1995b, AJ, 110, 1959

Ledlow M. J., Owen F. N., 1996, AJ, 112, 9

Loken C., Roettiger K., Burns J. O., Norman M., 1995, ApJ, 445, 80

Mahdavi A., Geller M. J., Fabricant D. G., Kurtz M. J., 1996, AJ, 111, 64

Markevitch M., Yamashita K., Furuzawa A., Tawara Y., 1994, ApJL, 436, L71

Matteucci F., Gibson B. K., 1996, astro-ph/9610059

Matsushita K., Makishima K., Awaki H., Canizares C. R., Fabian A. C., Fukazawa Y., Loewenstein M., Matsumoto H., Mihara T., Mushotzky R. F., Ohashi T., Ricker G. R., Serlemitsos P. J., Tsuru T., Tsusaka Y., Yamazaki T., 1994, ApJ, 436, L41
Matthews T. A., Morgan W. W., Schmidt M., 1964, ApJ, 140, 35
M^{c} Hardy I. M., 1979, MNRAS, 188, 495
Merrifield M. R., 1998, MNRAS, 294, 347
Merritt D., 1983, ApJ, 264, 24
Merritt D., 1984, ApJ, 276, 26
Mihara K., Takahara F., 1994, PASJ, 46, 447
Mitchell R. J., Culhane J. L., Davison P. J., Ives J. C., 1976, MNRAS, 176, 29P
Mobasher B., James P. A., 1996, MNRAS, 280, 895
Morbey, C., Morris, S., 1983, ApJ, 274, 502
Mulchaey J. S., Davis D. S., Mushotzky R. F., Burstein D., 1993, ApJ, 404, L9
Mushotzky R. F., Done C., Pounds K. A., 1993, ARA&A, 31, 717
Neumann M., Meisenheimer K., Roeser H.-J., Fink H. H., 1997, A&A, 318, 383
Noonan T. W., 1981, ApJS, 45, 613
Norman M. L., Burns J. O., Sulkanen M. E., 1988, Nat, 335, 146
Nulsen P. E. J., Böhringer H., 1995, MNRAS, 274, 1093
O'Dea C. P., 1985, ApJ, 295, 80
O'Dea C. P., Sarazin C. L., Owen F. N., 1987, ApJ, 316, 113
O'Donoghue A. A., Owen F. N., Eilek J. A., 1990, ApJS, 72, 75
O'Donoghue A. A., Eilek J. A., Owen F. N., 1993, ApJ, 408, 428
Oemler A., 1974, ApJ, 194, 1
Oke J. B., Sandage A., 1968, ApJ, 154, 21
Ostriker J. P., Hausman M. A., 1977, ApJL, 217, L125
Ostriker J. P., Tremain S. D., 1975, ApJL, 202, L113
Owen F. N., Laing R. A., MNRAS, 238, 357
Owen F. N., Ledlow M. J., 1997, ApJS, 108, 41
Owen F. N., Rudnick L., 1976, ApJ, 205, 1
Owen F. N., White R. A., 1991, MNRAS, 249, 164
Owen F. N., White R. A., Thronson H. A., 1988, AJ, 95, 1
Owen F. N., White R. A., Burns J. O., 1992, ApJS, 80, 501
Owen F. N., White R. A., Ge J., 1993, ApJS, 87, 135
Owen et al. 1982, AJ, 87, 1083
Owen F. N., Ledlow M. J., Keel W. C., 1995, AJ, 109, 14
Peebles P. J. E., 1990, 'Clusters of Galaxies', eds. Oegerle W. R., Fitchett M. J.,

Sarazin C. L., 1986, Rev. Mod. Phys., 58, 1
Sarazin C. L., McNamara B. R., 1997, ApJ, 480, 203
Sarazin C. L., Burns J. O., Roettiger K., McNamara B. R., 1995, ApJ, 447, 559
Schild R., Oke J. B., 1971, ApJ, 169, 209
Schindler S., 1996, A&A, 305, 756
Schindler S., Böhringer H., 1993, A&A, 269, 83
Schindler S., Müller E., 1993, A&A, 272, 137
Schindler S., Prieto A., 1997, A&A, 327, 37
Schneider P., Ehlers J., Falco E. E., 1992, 'Gravitational Lenses', (Spinger-Verlag)
Scheuer P. A. G., 1974, MNRAS, 166, 513
Scodeggio M., Solanes J. M., Giovanelli R., Haynes M., 1995, ApJ, 444, 41
Scodeggio M., Giovanelli R., Haynes M. P., 1997, AJ, 113, 101
Scott J. S., Robertson J. W., Tarenghi M., 1977, A&A, 59, 23
Serlemitsos P. J., Smith B. W., Boldt E. A., Holt S. S., Swank H., 1977, ApJL, 211. L63
Siebert J. Brinkman W., Morganti R., Tadhunter C. N., Danziger I. J., Fosbury R. A. E., di Serego Alighieri S., 1996, MNRAS, 279, 1331
Smith H., 1936, ApJ, 83, 23
Soltan A., Fabricant D. G., 1990, ApJ, 364, 433
Stark A. A., Gammie C. F., Wilson R. W., Bally J., Linke R. A., Heiles C., Hurwitz M., 1992, ApJS, 79, 77
Struble & Rood 1984, AJ, 89, 1487
Struble & Rood 1987, ApJS, 63, 555
Struble M. F., Rood H. J., 1991, ApJS, 77, 363
Toomre A., 1977, 'The Evolution of Galaxies and Stellar Populations', eds. Tinsley B. M., Larson R. B., (New Haven: Yale University Press)
Trinchieri G., Fabbiano G., 1985, ApJ, 296, 447
Trinchieri G., Fabbiano G., Kim D.-W., 1997, A&A, 318, 361
Vallée J. P., Bridle A. H., Wilson A. S., 1981, ApJ, 250, 66
van der Marel R. P., de Zeeuw P. T., Hans-Walter Rix, Quinlan G. D., 1997, Nat, 385, 610 bibitem Venturi T., Castaldini C., Cotton W. D., Feretti L., Giovannini G., Lara L., Marcaide J. M., Wehrle A. E., 1995, ApJ, 454, 735
Vikhlinin A., Forman W., Jones C., 1994, ApJ, 435, 162
Way M. J., Quintana H., Infante L., 1997, astro-ph/9709036
West M. J., Oemler A., Dekel A., 1988, ApJ, 327, 1
White D. A., Fabian A. C., Forman W., Jones C., Stern C., 1991, ApJ, 375, 35

White R. E., 1991, ApJ, 367, 69
White S. D. M., Briel U. G., Henry J. P., 1993, MNRAS, 261, 8
Wellman G. F., Daly R. A., Wan L., 1997, ApJ, 480, 96
Worrall D. M., Lawrence C. R., Pearson T. J., Readhead A. C. S., 1994, ApJL, 420, L17
Worrall D. M., Birkinshaw M., Cameron R. A., 1995, ApJ, 449, 93
Wrobel J. M., 1991, AJ, 101, 127
Yee H. K. C., Ellingson E., 1993, ApJ, 411, 43
Zabludoff A. I., Zaritsky D., 1995, ApJ, 447, 21
Zensus 1991, in 'Jets in Extragalactic Radio Sources', ads Röser H.-J., Meisenheimer K., (Springer-Verlag)
Zhao J-H., Burns J. O., Owen F. N., 1989, AJ, 98, 64
Zwicky F., 1933, Helv. Phys. acta, 6, 110
Zwicky F., 1957, 'Morphological Astronomy' (Berlin: Springer-Verlag)